National Library of Canada
Bibliothèque nationale du Canada

Canadian Theses Service
Service des thèses canadiennes

Ottawa, Canada
K1A 0N4

NOTICE

The quality of this microform is heavily dependent upon the quality of the original thesis submitted for microfilming. Every effort has been made to ensure the highest quality of reproduction possible.

If pages are missing, contact the university which granted the degree.

Some pages may have indistinct print especially if the original pages were typed with a poor typewriter ribbon or if the university sent us an inferior photocopy.

Previously copyrighted materials (journal articles, published tests, etc.) are not filmed.

Reproduction in full or in part of this microform is governed by the Canadian Copyright Act, R.S.C. 1970, c. C-30.

AVIS

La qualité de cette microforme dépend grandement de la qualité de la thèse soumise au microfilmage. Nous avons tout fait pour assurer une qualité supérieure de reproduction.

S'il manque des pages, veuillez communiquer avec l'université qui a conféré le grade.

La qualité d'impression de certaines pages peut laisser à désirer, surtout si les pages originales ont été dactylographiées à l'aide d'un ruban usé ou si l'université nous a fait parvenir une photocopie de qualité inférieure.

Les documents qui font déjà l'objet d'un droit d'auteur (articles de revue, tests publiés, etc.) ne sont pas microfilmés.

La reproduction, même partielle, de cette microforme est soumise à la Loi canadienne sur le droit d'auteur, SRC 1970, c. C-30.

NL-339 (r. 88/04)

Canada

THE UNIVERSITY OF ALBERTA

IMAGING CRUSTAL DIFFRACTION ZONES AND SEISMIC TOMOGRAPHY

by

SUHAS PHADKE

A THESIS

SUBMITTED TO THE FACULTY OF GRADUATE STUDIES AND RESEARCH

IN PARTIAL FULFILLMENT OF THE REQUIREMENTS FOR THE DEGREE

OF DOCTOR OF PHILOSOPHY

IN

GEOPHYSICS

DEPARTMENT OF PHYSICS

EDMONTON, ALBERTA

Spring 1988

Permission has been granted to the National Library of Canada to microfilm this thesis and to lend or sell copies of the film.

The author (copyright owner) has reserved other publication rights, and neither the thesis nor extensive extracts from it may be printed or otherwise reproduced without his/her written permission.

L'autorisation a été accordée à la Bibliothèque nationale du Canada de microfilmer cette thèse et de prêter ou de vendre des exemplaires du film.

L'auteur (titulaire du droit d'auteur) se réserve les autres droits de publication; ni la thèse ni de longs extraits de celle-ci ne doivent être imprimés ou autrement reproduits sans son autorisation écrite.

ISBN 0-315-42962-3

E. R. Kanasewich,
Department of Physics, University of Alberta,
Edmonton, Canada, T6G 2J1

March 23, 1988

To whoever it may concern

I hereby permit Mr. Suhas Phadke to reproduce Figure 4 of my paper titled 'Precambrian rift: Genesis of strata-bound ore deposits', which appeared in Science 1968, vol. 161, pp. 1002-1005, for his Ph.D. thesis.

Sincerely,

E. R. Kanasewich

THE UNIVERSITY OF ALBERTA

RELEASE FORM

NAME OF AUTHOR Suhas Phadke

TITLE OF THESIS IMAGING CRUSTAL DIFFRACTION ZONES AND SEISMIC TOMOGRAPHY

DEGREE FOR WHICH THESIS WAS PRESENTED Doctor of Philosophy

YEAR THIS DEGREE GRANTED Spring 1988

Permission is hereby granted to THE UNIVERSITY OF ALBERTA LIBRARY to reproduce single copies of this thesis and to lend or sell such copies for private, scholarly or scientific research purposes only. The author reserves other publication rights, and neither the thesis nor extensive extracts from it may be printed or otherwise reproduced without the author's written permission.

(SIGNED) Suhas Phadke

PERMANENT ADDRESS:

Phadke's House
Near Chattri Vegetable Market
LASHKAR, GWALIOR 474001
INDIA

DATED February 19, 1988

THE UNIVERSITY OF ALBERTA

FACULTY OF GRADUATE STUDIES AND RESEARCH

The undersigned certify that they have read, and recommend to the Faculty of Graduate Studies and Research, for acceptance, a thesis entitled IMAGING CRUSTAL DIFFRACTION ZONES AND SEISMIC TOMOGRAPHY submitted by SUHAS PHADKE in partial fulfillment of the requirements for the degree of DOCTOR OF PHILOSOPHY in GEOPHYSICS.

E. R. Kanasewich
Supervisor

Michael Evans

Flavian Abramovici
External Examiner

Date Feb 19, 1988

To the fond memory of my father

Madhukar Phadke

ABSTRACT

A tomographic method has been developed to determine three-dimensional structure and velocity model from seismic reflection data. The interfaces separating layers of different physical parameters in the model are approximated by polynomials and the velocity in each layer is either a constant or a linear function of depth. Direct modeling uses a ray bending method and inversion employs an iterative damped least-squares method. The method is stable and produces good estimates of the model parameters for a three-dimensional synthetic data set.

A two-dimensional Vibroseis seismic survey was carried out on Vancouver Island under the Project LITHOPROBE-I to determine the crustal structure and to understand the tectonics of this convergent margin. The tomographic method was applied to a small portion of Line-1, and a three-dimensional structure with a velocity model was obtained by taking advantage of the crookedness of the line.

A new seismic processing method, called the Common Fault Point (CFP) stacking method, has been developed to image discontinuities in the subsurface acoustic impedance. The method uses the diffraction hyperbolae produced by such discontinuities on prestack traces and concentrates the diffracted energy at the apexes by applying appropriate moveout and amplitude corrections and stacking. Each CFP stacked trace for a particular surface location being obtained by assuming diffractors to reside directly beneath that surface location. The CFP stacked section is produced by repeating the process for each surface location. The discontinuities are identified on these sections by high amplitudes.

The CFP method was tested for synthetic data with and without noise. A velocity model obtained from the seismic data at different source-receiver distances is used for CFP stacking. The method was also applied to reflection data sets from southern Alberta and

Melville Island. The vertical and lateral resolution limits of the method were investigated by using a step fault and a dyke model respectively. The resolution depends upon source pulse, the resolution criterion, the size of the Fresnel zone and the recording parameters.

ACKNOWLEDGEMENTS

I am overwhelmingly grateful to my supervisor, Professor E. R. Kanasewich, without whose continuous guidance and constant encouragement this work would not have been accomplished.

I am also grateful to Professors F. Abramovici, E. Nyland, M. E. Evans, U. M. Maydell, and S. S. Sheinin for their comprehensive and careful review of this work.

I would like to thank Mr. C. McCloughan for sharing his computer software expertise on many occasions. I also would like to thank my colleagues A. Vafidis and C. Tsingas for exchanging various scientific and nonscientific ideas during my Ph. D. studies.

The financial support provided by Alberta Oil Sands Technology and Research Authority, and Natural Sciences and Engineering Research Council of Canada, is greatly appreciated.

I would like to express my deep gratitude to Mr. P. J. Savage, Mr. L. Kelsch, and Mr. S. Campbell of PanCanadian Petroleum Limited for the seismic data in southern Alberta. I also thank them for making helpful suggestions. I would like to thank Mr. T. R. Reesor, Mr. W. E. Davitt, and Mr. C. Hitchon of Chevron Canada Resources Limited for the seismic data from Melville Island.

Last, but not least, I profoundly thank my family for being understanding and never questioning my decisions.

TABLE OF CONTENTS

CHAPTER	PAGE
1. INTRODUCTION	1
1.1 Introduction	1
1.2 Crustal Studies	1
1.3 Diffractions and Common Fault Point (CFP) Stacking Method	4
1.4 Outline of the Thesis	6
2. SEISMIC TOMOGRAPHY	8
2.1 Introduction	8
2.2 Tomographic Method	9
2.2.1 Forward Modeling	9
2.2.2 Inversion Procedure	16
2.2.3 Singular Value Decomposition	21
2.2.4 Treating Ill-Conditioned Matrices	24
2.2.5 Marquardt's Method	25
2.2.6 Resolution and Covariance Matrices	28
2.3 Synthetic Tests	32
2.4 Application to Vancouver Island Data	40
2.4.1 Tectonics of West coast of Canada	40
2.4.2 Application of Tomography	42
2.5 Conclusions	58
3. COMMON FAULT POINT (CFP) STACKING METHOD	60
3.1 Introduction	60
3.2 Amplitude and Phase Characteristics of Diffracted Signals	65

3.3 Method of Diffraction Moveout Correction and Stacking 73
3.4 Amplitude Correction 80
3.5 Synthetic Tests 82
3.6 Application to Real Data 89
3.6.1 Reflection, Gravity, and Magnetic survey in southern Alberta 89
3.6.2 Application to data from south of Princess well in Alberta 107
3.6.3 Application to data from Melville Island 116
3.7 Conclusions 121
4. RESOLUTION WITH REFLECTED AND DIFFRACTED WAVES 124
4.1 Introduction 124
4.2 Description of Source Pulse 124
4.3 Resolution of CFP stacking method 127
4.3.1 Definitions of resolution criterion 127
4.3.2 Discussion on resolution criterion 135
4.3.3 Vertical resolution 139
4.3.4 Lateral resolution 146
4.3.5 Resolution and recording parameters 150
4.4 Conclusions 155
5. CONCLUSIONS 157
REFERENCES 161
APPENDIX I PARTIAL DERIVATIVES 169
APPENDIX II DIFFRACTION RESPONSE FOR NONZERO SOURCE-RECEIVER SEPARATION 173

LIST OF TABLES

Figure		Page
2.1	A comparison of velocity models of Chiu et.al. (1986) and Clowes et.al. (1984).	46
2.2	Parameter sets for reflector C satisfying the least-squares criterion.	47
2.3	Parameter sets for reflector E satisfying the least-squares criterion.	48

LIST OF FIGURES

Figure		Page
2.1	Raypath for the media with velocity varying linearly with depth in the i^{th} layer. v and v' are the velocities at the start and end of the ray segment. θ and θ' are the angles made by the ray with the vertical at the start and end respectively.	13
2.2	A three layer model for testing the inversion procedure. The first interface is a dipping plane while the second and third interfaces are defined by second order polynomial. The velocities at the to of layers 1, 2, and 3 are 2.0, 3.5, and 4.5 km/s respectively and the velocity gradients are 0.6, 0.4, and 0.2 km/s/km respectively	33
2.3	Source receiver configuration for each shot. The receivers are in the form of a 5X5 grid and the grid spacing is 2 km. The shot is located at the center and is marked by X.	34
2.4	Source receiver configuration for generating synthetic traveltime data for the model of Figure 2.2.	35
2.5	Rays from source to receivers for one shot location.	36
2.6	Residual time contour maps (in milliseconds) after each iteration for one shot.	38
2.7	Flow chart for the tomographic algorithm.	39
2.8	Tectonic map of the west coast of Canada. JTWK-J. Tuzo Wilson Knolls, DSM-Dellwood Seamounts, WB-Winona Basin, ESM-Explorer Seamount, CSM-Cobb Seamounts, BBSM-Brown Bear Seamount, TSM-Thompson Seamount, MM-Meager Mountain, MC-Mount Cayley, MG-Mount Garibaldi, MB-Mount Baker, GP-Glacier Peak, MR-Mount Rainier, MA-Mount Adams, MSH-Mount St. Helens, MH-Mount Hood, MJ-Mount Jefferson, TS-Three-Sisters, FZ-Fracture Zone.	41

2.9 An expanded view of a portion of line 1 with the source and receiver locations. Solid squares are sources and open squares are receivers. +'s indicate the source-receiver midpoint locations. The inset shows a map of Vancouver Island along with the location of the four Vibroseis lines. 44

2.10 An example of the excellent original Vibroseis field data. 45

2.11 The three dimensional structure and velocity with gradient of reflector C and E for set II. 49

2.12 The generalized structural section across the subduction zone (Modified from Clowes et.al. 1984). The approximate location of line 1 chosen for inversion is indicated by an arrow. 50

2.13 A comparison of the velocity model obtained from inversion to that of Clowes et.al. 1984. 52

2.14 (a) The resolution matrix for reflector C. The order of the elements from 1 to 5 for the model parameters is a_0, a_{10}, a_{11}, v, and k respectively.
(b) The covariance matrix for reflector C. 53

2.15 (a) The resolution matrix for reflector E. The order of the elements from 1 to 4 for the model parameters is a_0, a_{10}, a_{11}, and v respectively.
(b) The covariance matrix for reflector E. 54

2.16 Structural map of the reflector C obtained by ray migration. The velocity obtained from inversion was used in the migration algorithm. 56

2.17 Structural map of the reflector E obtained by ray migration. 57

3.1 Receiver locations for three shots contributing to a CFP gather. S_1, S_2, and S_3 are the shot locations and $R_{1,max}$, $R_{2,max}$, and $R_{3,max}$ respectively are the receiver locations with maximum diffraction amplitude due to a discontinuity beneath the indicated CFP location. There are 26 ray paths that can contribute to a CFP gather. 63

3.2 A comparison between a CMP gather and a CFP gather. (a) A 3 fold CMP gather. (b) A CFP gather for the same shots. All 26 traces shown in Figure 3.1 contribute to this gather from 13 individual ray paths. 64

3.3 Geometry of a truncated plane reflector. The shot-receiver axis is perpendicular to the edge of the reflector. S and R are the positions of shot and receiver respectively, with shot-receiver midpoint as the origin. X_0 is the horizontal distance of the edge from the origin. Z_0 is the depth of the edge. Locations 1 to 19 are the surface locations with edge located beneath location 10. 67

3.4 (a) The diffraction response and (b) the combined reflection and diffraction response for the model of Figure 3.3. Shot point is at location 8 and the diffracting edge is below location 10. 70

3.5 A graph of the ratio (R) of diffraction amplitude to reflection amplitude versus the position of shot-receiver midpoint (X_0), for various depths of the diffracting edge (Z_0). 1. Z_0=500 m, 2. Z_0=750 m, 3. Z_0=1000 m 4. Z_0=2000 m, 5. Z_0=3000 m. 72

3.6 Geometry for the diffracted raypath when the diffracting edge is located below 'n-1' horizontal layers. 'i_1, i_2, ..., i_n' are the angles made by the downgoing ray with the vertical and 'j_1, j_2, ..., j_n' are the angles made by the upgoing ray with the vertical. 74

3.7 The time distance curve of a diffracted ray for a fixed shot position, two-way time T_0=1.0 sec., and V_{rms}=2000 m/s. The horizontal distance between the shotpoint and the diffractor is 200 m. The moveout correction for each value of D_r is equal to the time difference between the solid line and the dotted line for that value of D_r. 79

3.8 Plots of R as a function of (a) depth (Z_0) and (b) two-way vertical travel time (T_0), for various values of X_0. 1. X_0=0.0, 2. X_0=50.0, 3. X_0=100.0, 4. X_0=150.0, 5. X_0=200.0, 6. X_0=250.0. 81

3.9 The amplitude correction function (1/R) plotted as a function of two-way time for various values of X_0. 1. X_0=250.0, 2. X_0=200.0, 3. X_0=150.0, 4. X_0=100.0, 5. X_0=50.0, 6. X_0=0.0. 83

3.10 (a) and (b) are synthetic records with added noise for the model of Figure 3.3. SP is the location of the shotpoint. The vertical scale is the two-way travel time in seconds. (c) and (d) are the CMP stacks of synthetic records without and with added noise respectively. 86

3.11 (a) and (b) are the CFP stacks of synthetic records without and with added noise respectively. Amplitude correction is not applied after correcting for moveout. (c) and (d) are the CFP stacks of synthetic records without and with added noise respectively. Amplitude correction is applied here after correcting for moveout. 88

3.12 Location map of the Vibroseis line in Vulcan area of Southern Alberta. 90

3.13 Seismic Reflection cross-section across southern Alberta (Reproduced from Kanasewich, 1968). 92

3.14 (a) The Bouger gravity anomaly and (b) the aeromagnetic anomaly along the Vulcan seismic line. 93

3.15 A common depth point stacked section of the Vulcan seismic line. 95

3.16 f-k migrated section of line 83-421 along with its interpretation. 98

3.17 The model used for the calculation of gravity anomaly. The number above each shaded block represents the density contrast in gm/cc. 100

3.18 The schematic diagram for gravitational attraction due to shaded block at location P. 101

3.19 A comparison of observed and calculated gravity anomalies. 103

3.20 A CMP stacked section of a small portion (stations 440 to 500) of Vulcan Line. 105

3.21 A CFP stacked section of the portion of Vulcan Line shown in Figure 3.20. 106

3.22 Map of Southern Alberta showing the location of the seismic line. 108

3.23 A CMP stacked section of a portion of the seismic line from Princess area. The data is courtesy of PanCanadian Petroleum Ltd. 2WS - Second white specks, bFS - base Fish scale, M - top of Mississippian, Wab - Wabamun, A - Arctomys, P - Pika, S - Stephen PC - Precambrian. 110

3.24 A CFP stacked section of the line from Princess area. The solid shaded peaks indicate a positive polarity on the diffraction stack. The shaded gray peaks indicate negative polarity. 113

3.25 A line drawing of the Princess section along with the diffraction and fault interpretation made on the basis of the CFP stacked section. a. Boundary of the igneous intrusive, b. possible reactivation, c. possible erosional feature or carbonate buildup, d. faulting. 115

3.26 A map of Melville Island along with the location of the NS line 67-X. 117

3.27 A CDP stack of the seismic data from line 67-X. D - Devonian, S - Silurian UO - Upper Ordovician, MO - Middle Ordovician, C - Cambrian, PC - Precambrian. 120

3.28 A CFP stack of the seismic data from line 67-X. Peaks (blue) and troughs (red) having amplitudes above a preset threshold are plotted. Light blue - boundary between Silurian and Upper Ordovician, Pink - salt unit. 123

4.1 (a) Time domain representation of the seismic pulse used for generating synthetic seismograms for the step fault and dyke models. (b) Amplitude spectrum of the source pulse. 126

4.2 Rayleigh's criterion for resolution (a) diffraction pattern produced by a single slit (b) Resolved diffraction pattern from two slits (c) Rayleigh's limit of resolution for two slits (d) unresolved diffraction pattern from two slits. 129

4.3 A comparison of Rayleigh's and Ricker's criterion of resolution for an antisymmetric wavelet. 1. Rayleigh's limit of resolution 2. Ricker's limit of resolution. 130

4.4 Ricker's criterion for resolution. (a) a symmetric Ricker's wavelet (the second derivative of a Gaussian function) (b) two resolved wavelets (c) Ricker's limit of resolution (d) two unresolved wavelets. 132

4.5 Widess criterion applied to an antisymmetric wavelet. 134

4.6	Composite of two wavelets of same polarity plotted as a function of separation.	136
4.7	(a) The maximum absolute amplitude of the composite of two wavelets of same polarity plotted as a function of separation. (b) The maximum absolute amplitude of the composite of two wavelets of opposite polarity plotted as a function of separation.	137
4.8	Composite of two wavelets of opposite polarity plotted as a function of separation.	138
4.9	Geometry of the step fault model.	141
4.10	CDP and CFP stacked sections of the step fault model for (a) $\Delta z=\lambda$ (b) $\Delta z=\lambda/2$ (c) $\Delta z=\lambda/4$ (d) $\Delta z=\lambda/16$.	142
4.11	Variation of peak amplitude on the CFP section plotted as a function of $\Delta z/\lambda$.	144
4.12	Amplitude on CFP section for step fault model plotted as a function of horizontal distance.	145
4.13	Relationship between the extent of the Fresnel zone and frequency.	147
4.14	Fresnel zone explanation for changes in waveshape produced by the edge of a feature.	148
4.15	The model of a dyke.	151
4.16	CDP and CFP stacked sections of the dyke model for widths of (a) 2λ (b) λ (c) $\lambda/2$ (d) $\lambda/4$.	152
4.17	Amplitude on CFP section for dyke model plotted as a function of horizontal distance.	154
II.1	Geometry for the Kirchhoff formulation of diffraction response.	175

II.2 Prolate spheroidal coordinate system. 's' and 'g' are the shot and receiver locations. 'r_s' and 'r_g' are the distances of the shot and receiver respectively from the subsurface point. 'r_s+r_g' is constant on the ellipsoid of revolution about the x-axis. 177

II.3 Geometry for the calculation of diffraction response due to a diffracting edge perpendicular to the shot-receiver axis. 181

CHAPTER 1

INTRODUCTION

1.1 Introduction

Recordings of mechanical vibrations of the earth, usually called seismograms, are the basic data used in seismology to determine the structure and elastic parameters. Natural vibrations of the earth caused by earthquakes provide data for studying the deeper parts of the earth. Artificially caused vibrations (explosions, airgun, vibrators) find applications in crustal studies, mineral prospecting and exploration for oil and natural gas. The field seismograms have to go through several steps of processing before one may make inferences regarding the structural features of the subsurface. Basically there are two ways of interpreting seismic records. In the first method the recorded data are compared with the artificially generated data by assuming an earth model. In the second method the recorded seismograms are transformed and displayed in such a way as to resemble a two-dimensional image (called a seismic section) of the earth. Usually an admixture of both is used to arrive at a decision.

In this thesis, new methods for generating seismic sections are described to study the earth's lithosphere and to locate discontinuities in the seismic acoustic impedances in the crust.

1.2 Crustal Studies

The crust is the outermost shell of the earth. Its thickness varies from 5 km under the oceans to 70 km under some mountains and is a very heterogeneous mixture of

sedimentary, igneous and metamorphic rocks with large acoustic impedance contrasts separating various layers or zones. The upper part of the earth, approximately 100 km thick, is a more or less rigid shell called the lithosphere. The Mohorovicic discontinuity (or Moho) is a boundary separating the lithosphere into a heterogeneous lower velocity crust and a more homogeneous upper mantle which is defined by a compressional wave velocity between 7.7 and 8.5 km/s (Isacks, Oliver and Sykes, 1968). There appears to be a relatively sudden change in seismic velocity from less than 7.3 km/s to about 8.0 km/s at the Moho. The lithosphere of the earth is divided up into 7 or 8 major plates and an undetermined number of microplates by transform faults, subduction zones and spreading centers. Transform faults, first recognized by J. T. Wilson (1965), are strike slip faults that accommodate movement generated at spreading centers, which are often marked by mid-oceanic ridges where new hot and molten material is introduced for the creation of lithosphere. The lithosphere material is destroyed at subduction or Benioff zones (Benioff, 1954) which are underthrust fault zones where the heavier of two convergent plates descends under the lighter one.

The oceanic crust is continuously created and consumed at plate boundaries and the determination of its structure and physical properties is of great importance in studying the tectonics of an area. There is growing evidence that not all the material of oceanic crust is destroyed at the convergent boundaries. The remains are plastered against the continental crust. This phenomenon has been observed in most parts of the western north America (Cox, Dalrymple and Doell 1967, Coney 1981, Coney et al. 1981). These masses of additional material are called *accreted terranes* and are characterized by large deformations. *Suspect terranes* are regional rock assemblages that may be exotic to the home continent in which they now reside. In thin-skinned tectonics of southern Appalachians, the crystalline rocks appear to have been thrust to the west and overlie sedimentary rocks (Cook et al. 1979). This happens when the rocks from one plate are forced to come aboard some other

plate at a convergent boundary. The formation of ore deposits may also be related to activity at plate boundaries or an active rift (Kanasewich 1968).

Cross-sectional imaging of objects from either transmitted or reflected waves is called tomography. The term is derived from the Greek *tomos* meaning section or slice. In this method the target object is illuminated from many different directions either sequentially or simultaneously and the transmitted or reflected data are used to reconstruct an image of the object. Medical tomography has been successfully used to reconstruct an image of organs within the body by X-rays or by ultrasonic rays. This is basically transmission tomography and makes use of the physical property of these waves to be attenuated in matter. Some of the medical studies of tomography are discussed by Kak (1979), Kak (1981), Norton and Linzer (1979), and Stark and Paul (1981). Recently tomographic methods have been used to construct images of underground structures for seismic exploration, cross-sectional imaging for nondestructive testing and other uses. Some applications of these methods for shallow and deep studies are discussed by Aki and Lee (1976), Hawley et al. (1981), Gjoystdal and Ursin (1981), McMechan (1983), Kanasewich and Chiu (1985), Bishop et al. (1985), Chiu et al. (1986) and Chiu and Stewart (1987). Two major applications of tomography in seismic exploration are cross-borehole imaging of earth resources by transmitted waves, and determination of earth's structure by reflected waves observed on the surface. The method has also been used for studying global structure by transmitted waves from earthquakes.

In this thesis a new seismic reflection tomographic method is described. Seismic reflection tomography uses the traveltime information of the reflected elastic waves to determine the three-dimensional structure and physical properties of the earth. An estimate of the model is modified iteratively by using a least-squares inversion technique.

A seismic reflection survey was carried out on Vancouver Island under the Project LITHOPROBE-I (Clowes et al. 1984, Yorath et al. 1985, Green et al. 1986, Chiu et al.

1986) to study the crustal structure and tectonics of this convergent margin. Four seismic profiles were shot which provided the structural and velocity information after usual common depth point stacking. The lines, following mountain forestry roads, were not straight but crooked creating difficulties for the standard seismic data processing. However, due precisely to the crookedness of the lines the reflection points were located in three-dimensional space and this made possible to obtain three-dimensional structure of the subsurface.

In this thesis an iterative damped least-squares technique was used to obtain three-dimensional structure and velocity with gradients since the travel time is a nonlinear function of model parameters. Ray tracing was performed for each shot-receiver pair by solving a system of nonlinear equations. In constant velocity media the raypath is a straight line, whereas in media with velocity varying linearly with depth it follows the arc of a circle. The interfaces are defined by polynomial surfaces where the raypaths satisfy Snell's law. The method was tested for a synthetic model which shows that it is stable and effective. Then the method was applied to a small portion of Line 1 of Vancouver Island to obtain velocity gradients and three-dimensional structures of the decollement and subduction zones.

1.3 Diffractions and Common Fault Point (CFP) Stacking Method

Diffractions are produced by waves incident upon edges, corners or vertices of boundary surfaces. The presence of diffractions on seismic sections usually indicates discontinuities in the subsurface acoustic impedance. Diffractions are associated with various geological discontinuities, e.g. a fault, a pinchout, a wedgeout, unconformities across changes in acoustic impedance, a reef edge or any sudden change of facies (Haagedorn 1954, Stone 1974). Sometimes they manifest themselves as seismic bright

spots or flat spots, but in general they are good indicators of structural and stratigraphic anomalies and can be of great importance in hydrocarbon prospecting. Thus, processing techniques should be designed to enhance the detection of point diffractors, not to remove them by destructive interference.

In routine seismic processing normal moveout (NMO) corrections are performed to enhance reflected signals on seismic sections. On common depth point (CDP) or common midpoint (CMP) stacked sections, interference of the reflections from the two faulted blocks and the diffractions from their edges hinders fault location determination. Destruction of diffraction patterns by post-stack migration further inhibits proper imaging of diffracting centers.

This thesis presents a new technique which helps in the interpretation of diffracting edges by concentrating the signal amplitudes from discontinuous diffracting points on seismic sections. It involves application to the data of moveout and amplitude corrections appropriate to an assumed diffractor location. The maximum diffraction amplitude occurs at a receiver location for which the diffracting discontinuity is situated beneath the source-receiver midpoint. As the amplitudes of these diffracted signals drop very rapidly on either side of this receiver location, where one expects maximum amplitude, an appropriate amplitude correction must be applied to the data. As the diffractions are present on all the traces, one can use a very large number of signals to obtain a stacked trace for one possible diffractor location. Stacks of 100 to 400 traces are quite feasible with ordinary 12 or 24 fold field acquisition. Repetition of this procedure for diffractors assumed to be located beneath each surface point results in the Common Fault Point (CFP) stacked section, which shows diffractor locations by high amplitudes.

A CMP section displays reflection data reduced to vertical incidence travel paths, whereas a CFP section displays diffraction arrivals at vertical incidence. A CFP section shows not only diffractions from fault edges, but also those from other geological features with impedance discontinuities or large gradients in the impedance. For example, reefs, salt

domes, intrusions, unconformities and discontinuity in fluid content will all produce diffraction patterns in varying degrees.

The method, tested on synthetic data with and without noise, proves to be quite effective, but it is sensitive to the velocity model used for moveout corrections. Therefore the velocity model obtained from NMO stacking is generally used for enhancing diffractor locations by stacking. The vertical and lateral resolution limits of the CFP method are also investigated.

Finally the potential of the method is demonstrated by applying it to the reflection data sets from an area south of the Princess well in Alberta and from Melville Island in the Northwest Territories.

Reflection surveys carried out in southern Alberta (Kanasewich and Cumming 1965, Clowes et al. 1967) indicate several continuous deep reflecting horizons. A careful study of deep reflections detected a Precambrian rift valley (i.e. an ancient spreading center similar to the one under the Red Sea at the present time) below flat-lying sediments (Kanasewich 1968). An interpretation of seismic reflection data obtained in this region by PanCanadian Petroleum Limited was carried out and is presented in this thesis. CFP stacking method was also applied to a small portion of the Vulcan seismic line.

1.4 Outline of the thesis

The thesis consists of five chapters.

Chapter 1 contains an introduction and outline of the thesis.

In Chapter 2 a tomographic method is described to obtain a three-dimensional structure and velocity with gradients. The method is applied to a seismic line from Vancouver Island.

In Chapter 3 a new method to detect seismic discontinuities in the subsurface is

presented. The method is called the Common Fault Point (CFP) stacking method and makes use of the diffracted waves produced by the discontinuities. The technique is tested by applying it to synthetic and real data. The first set of real data includes the application of the CFP stacking method to a small portion of the Vulcan line from southern Alberta. A combined interpretation of seismic and gravity data for this line is also presented. The second example is from an area south of the Princess well in Alberta. The third example is from Melville Island in the Northwest Territories.

In Chapter 4 resolution with reflected and diffracted waves is discussed. Vertical and lateral resolution limits of the CFP method are also determined.

Chapter 5 contains the conclusions, discusses the original contribution in the thesis and makes suggestions on future work.

CHAPTER 2

SEISMIC TOMOGRAPHY

2.1 Introduction

In the recent past seismic tomography has been extensively used for seismic modeling. It is used to obtain the three-dimensional structure and the physical parameters of the earth by using the traveltime information of the elastic waves. By minimizing the squared differences between the observed traveltimes and traveltimes calculated from an initial estimate of the model parameters, the model is modified iteratively by inverting a linearized version of least-squares formulation. Thus the goal of reflection tomography is to find a model for which the model traveltimes closely match the real traveltimes. The model obtained can be displayed as two-dimensional slices or three-dimensional structure.

Tomographic methods have been applied to several geophysical problems. Formulation and methodology of seismic tomography were discussed by Cutler et al.(1984). It is basically similar to the determination of physical parameters by least-squares inversion techniques. Some applications of these methods are discussed by Kanasewich and Chiu (1985), Bishop et al. (1985), and Chiu et al. (1986).

In this chapter a technique is presented which determines a three-dimensional structure and velocity with gradients from seismic reflection data. The input to the algorithm consists in the traveltimes of selected events from unstacked seismic reflection records and an initial estimate of the model parameters. This is basically an iterative processing method based on a least-squares inversion technique. For forward modeling a fast and computationally efficient algorithm for tracing seismic rays was developed as part of the tomographic method. For inversion an iterative damped linear least-squares method

is based on the Levenberg-Marquardt method (Levenberg 1944, Marquardt 1963). The damping factor improves the stability of the method at the expense of the resolution of the parameters. The lease-squares method reduces the L2 norm and therefore assumes that the data error obeys the Gaussian distributation.

Finally the tomographic method was applied to a reflection seismic data set from Vancouver Island. At first the velocities in each layer were assumed constant. But then it was found that the model obtained was not consistent with refraction modeling. The model obtained by introducing velocity gradients was found to be consistent with previous models.

2.2 Tomographic Method

The method of tomographic inversion basically involves three steps: (1) forward modeling is used to obtain travel times and their derivatives with respect to the model parameters; (2) inversion using the field data and the information for the direct modelling to produce an updated model; (3) iteration to produce a model within specified error limits. The input to the algorithm is the traveltime information picked from the unstacked traces and an initial estimate of the model parameters. The output consists of the model parameters which fit the observed traveltimes in a least-squares sense.

2.2.1 Forward Modeling

In forward modelling one solves the direct problem of finding the travel times when the earth model is known. The problem is solved by tracing the rays from sources to receivers. The simplest problem is to find the travel times when the structure and velocity of the subsurface is given. The procedure is based on Fermat's principle which is satisfied if the integral of the slowness along the ray is a minimum,

$$t = \text{Min} \int_{ray} s(x,y,z)\, dl \qquad (2.1)$$

In this equation t is the traveltime, s(x,y,z) is the slowness (inverse of velocity) at the point (x,y,z) and 'dl' is the differential length along the ray. To implement equation (2.1) in order to find the traveltime the raypath between the source and receiver must be known and the slowness along this path must also be known. The method of ray tracing is used to determine the raypath.

There are two methods of tracing seismic rays between given end points through three dimensional structure. In the first method one shoots a ray from the source in a particular direction and determines its point of emergence. Then the starting direction is modified repeatedly until the ray emerges at the desired point. In the second method an initial guess of the raypath between the source and receiver is made and then this raypath is modified till it satisfies the principle of least time. The first method is called the shooting method and the second method is called the bending method. Julian and Gubbins (1977) have shown that the bending method is computationally faster than the shooting method by a factor of 10 or more. Therefore we made use of the bending method for the following study.

For ray tracing a description of the earth model is made. The description includes (a) the number of model interfaces (b) the layer velocities and (c) the geometrical relationship in three-dimensional-space between the interfaces and layer velocities.

The functions representing the interfaces must be continuous together with their first and second derivatives. This is because in the forward modelling with the ray bending method one solves a set of nonlinear equations. The solution of a nonlinear equation numerically involves the calculation of a Jacobian, the elements of which are partial derivatives. Several mathematical functions satisfy these properties but one should consider

only those functions which resemble the geological interfaces to some extent. Keeping this in mind an interface may be represented by spline function (Gjoystdal et al. 1984, Gjoystdal & Ursin 1981) or in the form of a Fourier Series (Chiu and Stewart 1987) or by a polynomial (Chiu et al. 1986). For this study we have used the representation of the interfaces by polynomials of the form

$$z_i = a_0 + f_i(x,y) \qquad i = 1, ..., L \tag{2.2}$$

where a_0 is the depth of the interface at the origin and $f_i(x,y)$ is a function of x and y given by

$$f_i(x,y) = \sum_{j=1}^{N} \sum_{k=0}^{j} a_{jk} x^k y^{j-k} \tag{2.3}$$

In the above expression N is the degree of the interface a_{jk} are the coefficients and i is the index for the interface. L is the number of interfaces in the model. Other expressions for interfaces can be very easily incorporated in the algorithm.

The next task is to express the velocities in each layer. Velocity can be expressed as a function of x, y, and z. For the present study we assume that the velocity in each layer is either a constant or a linear function of depth. Taking more complicated functions for the velocity only complicates the algebra but is otherwise straightforward.

The raypath between two given end points in a layer depends upon the velocity of the medium. If the velocity is constant then the raypath is a straight line. However if the velocity is a linear function of depth then the raypath is an arc of a circle (Dobrin, 1976).

Let the source and receiver locations be (x_0,y_0,z_0) and (x_n,y_n,z_n) respectively and assume that there are n ray segments. Each ray segment is contained within a particular layer, therefore it is either a straight line or the arc of a circle. Then the travel time along the ray is equal to the sum of traveltimes along the individual ray segments, i.e.

$$t = \sum_{i=1}^{n} t_i \tag{2.4}$$

If the velocity is constant for the i^{th} ray segment i.e. between points $(x_{i-1},y_{i-1},z_{i-1})$ and (x_i,y_i,z_i), then the traveltime is

$$t_i = \frac{[(x_i - x_{i-1})^2 + (y_i - y_{i-1})^2 + (z_i - z_{i-1})^2]^{1/2}}{v_i} \tag{2.5}$$

If the velocity is a linear function of the depth z i.e.

$$v_i = v_i + k_i (z_i - z_{i-1}) \tag{2.6}$$

where v_i and v_i' are the velocities at the start and end of the i^{th} ray segment and k_i is the velocity gradient, then the travel time t_i is given by (Figure 2.1)

$$t_i = \frac{1}{k_i} \ln\left[\frac{v_i'(1 + \cos \theta_i)}{v_i (1 + \cos \theta_i')} \right] \tag{2.7}$$

where

$$\tan \theta_i = \frac{2 v_i k_i R_i}{(v_i)^2 + k_i^2 R_i^2 - v_i^2}$$

$$R_i = [(x_i - x_{i-1})^2 + (y_i - y_{i-1})^2]^{1/2}$$

$$\text{and} \quad \frac{\sin \theta_i}{v_i} = \frac{\sin \theta_i'}{v_i'}$$

To determine the raypath using the bending method an initial estimate of the raypath is perturbed while keeping the ends fixed. Chander (1977) developed an algorithm of this nature for tracing rays through three-dimensional media having plane interfaces. We have modified this algorithm to accommodate polynomial interfaces and velocities varying linearly with depth. This is essentially a variational approach where Fermat's principle of

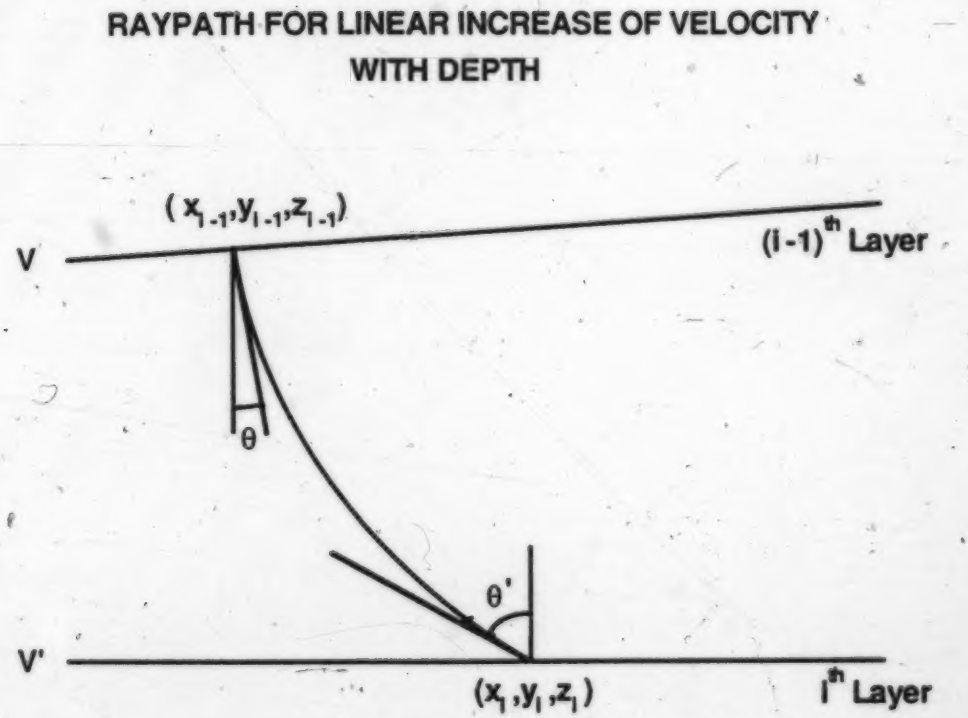

Figure 2.1 Raypath for the media with velocity varying linearly with depth in the i^{th} layer. v and v' are the velocities at the start and end of the ray segment. θ and θ' are the angles made by the ray with the vertical at the start and end respectively.

stationarity of travel time with respect to small path variations is used. The travel time is made stationary by setting the partial derivatives of t with respect to x_i and y_i ($i = 1,..n-1$) equal to zero and solving the resulting system of (2n-2) equations, i.e.

$$\frac{\partial t}{\partial x_i} = \frac{\partial t_i}{\partial x_i} + \frac{\partial t_{i+1}}{\partial x_i} = 0 \qquad i = 1, ...n-1$$

$$\text{and} \quad \frac{\partial t}{\partial y_i} = \frac{\partial t_i}{\partial y_i} + \frac{\partial t_{i+1}}{\partial y_i} = 0 \qquad i = 1, ...n-1 \tag{2.8}$$

The solution of these (2n-2) nonlinear equations gives the coordinates of the starting and end points of each ray segment.

For v_i = constant

$$\frac{\partial t_i}{\partial x_i} = \frac{[\, x_i - x_{i-1} + \frac{\partial z_i}{\partial x_i}(z_i - z_{i-1})\,]}{v_i\,[\,(x_i - x_{i-1})^2 + (y_i - y_{i-1})^2 + (z_i - z_{i-1})^2\,]^{1/2}} \tag{2.9}$$

$$\frac{\partial t_i}{\partial y_i} = \frac{[\, y_i - y_{i-1} + \frac{\partial z_i}{\partial y_i}(z_i - z_{i-1})\,]}{v_i\,[\,(x_i - x_{i-1})^2 + (y_i - y_{i-1})^2 + (z_i - z_{i-1})^2\,]^{1/2}} \tag{2.10}$$

For v_{i+1} = constant

$$\frac{\partial t_{i+1}}{\partial x_i} = \frac{[\, x_i - x_{i+1} + \frac{\partial z_i}{\partial x_i}(z_i - z_{i+1})\,]}{v_{i+1}\,[\,(x_i - x_{i+1})^2 + (y_i - y_{i+1})^2 + (z_i - z_{i+1})^2\,]^{1/2}} \tag{2.11}$$

$$\frac{\partial t_{i+1}}{\partial y_i} = \frac{[\, y_i - y_{i+1} + \frac{\partial z_i}{\partial y_i}(z_i - z_{i+1})\,]}{v_{i+1}\,[\,(x_i - x_{i+1})^2 + (y_i - y_{i+1})^2 + (z_i - z_{i+1})^2\,]^{1/2}} \tag{2.12}$$

For the velocity varying linearly with depth in the i^{th} segment

$$\frac{\partial t_i}{\partial x_i} = \frac{1}{k_i}\left[\frac{1}{v_i'}\frac{\partial v_i'}{\partial x_i} - \frac{\sin\theta_i}{(1+\cos\theta_i)}\frac{\partial \theta_i}{\partial x_i} + \frac{\sin\theta_i'}{(1+\cos\theta_i')}\frac{\partial \theta_i'}{\partial x_i}\right] \tag{2.13}$$

$$\frac{\partial t_i}{\partial y_i} = \frac{1}{k_i}\left[\frac{1}{v_i'}\frac{\partial v_i'}{\partial y_i} - \frac{\sin\theta_i}{(1+\cos\theta_i)}\frac{\partial \theta_i}{\partial y_i} + \frac{\sin\theta_i'}{(1+\cos\theta_i')}\frac{\partial \theta_i'}{\partial y_i}\right] \tag{2.14}$$

For the velocity varying linearly with depth in the $(i+1)^{th}$ segment

$$\frac{\partial t_{i+1}}{\partial x_i} = \frac{1}{k_{i+1}}\left[\frac{1}{v_{i+1}'}\frac{\partial v_{i+1}'}{\partial x_i} - \frac{\sin\theta_{i+1}}{(1+\cos\theta_{i+1})}\frac{\partial \theta_{i+1}}{\partial x_i} + \frac{\sin\theta_{i+1}'}{(1+\cos\theta_{i+1}')}\frac{\partial \theta_{i+1}'}{\partial x_i}\right] \tag{2.15}$$

$$\frac{\partial t_{i+1}}{\partial y_i} = \frac{1}{k_{i+1}}\left[\frac{1}{v_{i+1}'}\frac{\partial v_{i+1}'}{\partial y_i} - \frac{\sin\theta_{i+1}}{(1+\cos\theta_{i+1})}\frac{\partial \theta_{i+1}}{\partial y_i} + \frac{\sin\theta_{i+1}'}{(1+\cos\theta_{i+1}')}\frac{\partial \theta_{i+1}'}{\partial y_i}\right] \tag{2.16}$$

The partial derivatives appearing in the above equations are given in the Appendix I. The nonlinear algebraic equations can be expressed in a compact form as

$$f_i(X,Y) = 0 \qquad i = 1, \ldots 2n-2 \tag{2.17}$$

where

$$X = (x_1, x_2, \ldots x_{n-1})$$
$$Y = (y_1, y_2, \ldots y_{n-1})$$

or by combining vectors X and Y we can write them as

$$f_i(X) = (x_1, x_2, \ldots x_{2n-2}) \qquad i = 1, \ldots 2n-2 \tag{2.18}$$

This system of equations can be solved by the Newton-Raphson iteration method. In this method an estimate $X^{(k)}$ of the solution is corrected to

$$X^{(k+1)} = X^{(k)} + \delta^{(k)} \tag{2.19}$$

where $\delta^{(k)}$ is the solution of the linear system

$$f_i(X^{(k)}) = - \sum_{j=1}^{2n-2} J_{ij}^{(k)} \delta_j^{(k)} \qquad i = 1, \ldots 2n-2 \tag{2.20}$$

$J_{ij}^{(k)}$ being the Jacobian of f_i with respect to x_j at $X = X^{(k)}$, i.e.

$$J_{ij}^{(k)} = \left[\frac{\partial f_i}{\partial x_j} \right]_{X = X^{(k)}} \tag{2.21}$$

The Newton-Raphson method for the solution of nonlinear systems is generally expected to give quadratic convergence since equation (2.20) takes account of the first order terms in the Taylor series expansion of $f_i(X)$ about $X=X^{(k)}$. This method often fails if the initial estimate is not a good approximation to the solution of the system.

Several algorithms have been developed for the Newton-Raphson method which make the method converge even when a close initial estimate of the solution is not available. Powell (1970) proposed a hybrid method for the solution of a nonlinear system. In this method the correction δ is calculated from equation (2.20) and the X is replaced by $X+\lambda\delta$. The value of the parameter λ is calculated by a search process which tries to make the estimate $(X+\lambda\delta)$ better than the estimate X by using the criterion

$$F(X+\lambda\delta) < F(X) \tag{2.22}$$

where F(X) is the sum of the squares of the residuals

$$F(X) = \sum_{k=1}^{2n-2} \left[f_k(X) \right]^2 \tag{2.23}$$

This algorithm is very similar to the Levenberg-Marquardt method. The essential feature in this algorithm is to guarantee a decrease in the sum of squares of the residuals via the steepest descent direction when X is far from the minimum and to switch to the rapid convergence of Newton's method as the minimum is approached.

2.2.2 Inversion Procedure

If the number of observations is different than the number of unknown model parameters, then an exact solution to the inverse problem does not always exist. The least-squares solution arose from consideration of inverse problems that had no exact solution. The next best thing in this case is to estimate the solution by those values of the model parameters which best satisfy the observations.

Suppose there are 'm' parameters, $\mathbf{M} = (M_1, M_2, \ldots M_m)$, of the earth to be determined from n observations made on the surface of the earth. In seismic tomography the unknown parameters are the coefficients of the layer interfaces, together with the velocities and the velocity gradients in each layer. The observed data consist of the traveltimes of the elastic waves reflected from the various geological interfaces. Suppose there are n observed traveltimes forming the vector $T = (T_1, T_2, \ldots T_n)$. Each traveltime can be expressed as a function of the model parameters

$$T_i = t_i(M_1, M_2, \ldots M_m) \qquad i = 1, \ldots n \tag{2.24}$$

Usually the function relating the traveltimes with the model parameters is nonlinear. But if we assume that it varies smoothly enough and if some approximate values of the parameters are known, then the problem can be linearized and the solution is found iteratively. Let the approximate values of the model parameters be represented by

$$\mathbf{M}^a = (M_1^a, M_2^a, \ldots M_m^a) \tag{2.25}$$

Expanding T_i in terms of $\mathbf{M}^a$ by a first order Taylor expansion, we obtain a set of linear equations for the observed data

$$T_i = t_i(\mathbf{M}^a) + \sum_{j=1}^{m} \left.\frac{\partial t_i}{\partial M_j}\right|_{\mathbf{M}=\mathbf{M}^a} (M_j - M_j^a) \tag{2.26}$$

or

$$(T_i - t_i^a) = \sum_{j=1}^{m} \left.\frac{\partial t_i}{\partial M_j}\right|_{M=M^a} (M_j - M_j^a) \qquad (2.27)$$

where T_i (i = 1, ...n) are the observed traveltimes, M^a is the initial estimate of model parameters and t_i^a (i = 1, ...n) are the calculated traveltimes from the initial estimate of model parameters. It is extremely important to note that the linear inverse method often fails if the function $t_i(M)$ is not continuous. Writing equation (2.27) in matrix form

$$\Delta t = A\,\delta \qquad (2.28)$$

where Δt is a (n x 1) column vector of the differences between observed and calculated traveltimes, $\delta = M_j - M_j^a$ is the (m x 1) correction vector and A is the (n x m) matrix containing the partial derivatives

$$A = \begin{bmatrix} \frac{\partial t_1}{\partial M_1} & \frac{\partial t_1}{\partial M_2} & \cdots & \frac{\partial t_1}{\partial M_m} \\ \frac{\partial t_2}{\partial M_1} & \cdots & \cdots & \cdots \\ \cdots & \cdots & \cdots & \cdots \\ \frac{\partial t_n}{\partial M_1} & \cdots & \cdots & \frac{\partial t_n}{\partial M_m} \end{bmatrix} \qquad (2.29)$$

The inverse problem is made overdetermined by choosing less parameters to solve for than the number of observations i.e. n > m. Then the solution is determined by minimizing the square of the error between the observed data and the calculated data. Let the error for each data set be ε

$$\varepsilon = A\,\delta - \Delta t \qquad (2.30)$$

then

$$\mu = |\varepsilon|^2 = \sum_{i=1}^{n} \left(\sum_{j=1}^{m} a_{ij}\,\delta_j - \Delta t_i \right)^2 \tag{2.31}$$

To minimize μ (error square) we equate to zero the partial derivatives with respect to δ

$$\frac{\partial \mu}{\partial \delta_k} = \sum_{i=1}^{n} 2 \left(\sum_{j=1}^{m} a_{ij}\,\delta_j - \Delta t_i \right) a_{ik} = 0$$

or

$$\sum_{i=1}^{n} a_{ik} \sum_{j=1}^{m} a_{ij}\,\delta_j = \sum_{i=1}^{n} a_{ik}\,\Delta t_i$$

or in matrix form

$$A^T A\,\delta = A^T \Delta t \tag{2.32}$$

This is the least square formulation of equation (2.28) and the solution is

$$\delta = (A^T A)^{-1} A^T \Delta t \tag{2.33}$$

Since the problem is linearized by dropping the higher order terms in the Taylor series expansion of equation (2.24), a new estimate of the model parameters is obtained by

$$M_j = M_j^a + \delta_j \tag{2.34}$$

This estimate is closer to the solution than the initial guess. Next this estimate is used as the initial estimate and again the parameter vector is modified i.e. for the n^{th} iteration

$$M_j^{(n+1)} = M_j^{(n)} + \delta_j^{(n)} \tag{2.35}$$

The iterative process is continued until the error ε falls below a preset threshold, or the new parameter vector does not show any improvement over the old parameter vector. Equation (2.32) represents a set of normal equations and involves the inverse of the matrix ($A^T A$).

Therefore it is necessary for an inverse to exist that the determinant be nonsingular i.e.

$$\det (A^T A) \neq 0 \tag{2.36}$$

Also the matrix $(A^T A)$ is always symmetric and its eigenvalues are not only real but nonnegative.

There are several methods available for the solution of a system of linear equations. Gaussian elimination method and Cholesky's method are a few of the simple , fast, and economical methods of solving a system of equations. Unfortunately these methods are known to be unstable for the linear least-squares problem.The major difficulty with the above mentioned methods arises when the coefficient matrix $A^T A$ is singular or nearly singular. When the matrix is singular then either there are infinite solutions or there is no solution. But for a nearly singular matrix the situation is even worse. In this case the algorithm will converge to a solution but the solution obtained will consist of numbers totally unrelated to the problem. Of course this does not always happen; it may happen often enough to make this approach unreliable.

It is hard to determine the singular nature of a matrix, if the dimensions of the matrix are large. Then the standard procedure is to determine the rank of the matrix. If the matrix is deficient in rank then it is singular. The practical method to determine the rank is to triangularize by Gaussian elimination. If no zeroes show up on the diagonal of the final triangularized matrix of $A^T A$ then the rank is equal to m, the matrix is of full rank and a unique solution exists. If there are zeroes on the diagonal, the matrix is rank deficient and there is no unique solution or no solution at all. In practice, due to the round-off errors in the elimination process, the triangularized matrix does not have a proper number of zeroes on the diagonal. Besides, the matrix A usually involves some inherent errors like errors in the data or in the numerical computation. Therefore even if the matrix is singular the triangularized form of it may not show this. To handle such situations and to get more information on the various aspects of the solution like its resolution matrix, covariance

matrix etc. the singular value decomposition (SVD) method is used.

2.2.3 Singular Value Decomposition

Lanczos (1961) proposed a method of singular value decomposition (SVD) of a matrix. This type of approach is important in analyzing the rank deficient matrices. Golub and Reinsch (1970) described the computational aspects of this approach. The method is best understood with the concepts of model space and data space.

The fundamental equation to be inverted is expressed by

$$\Delta t = A\,\delta \tag{2.37}$$

where δ is a (mx1) vector in the model space, Δt is a (nx1) vector in the data space and A is a (nxm) matrix. The matrix A can be written as a product of three matrices

$$A = U\,\Lambda\,V^T \tag{2.38}$$

The matrix U is a (nxn) matrix of vectors that span the data space

$$U = [\,u_1, u_2, \ldots u_n\,]$$

where u_i's are the individual vectors. The vectors are orthogonal to one another and can be chosen to be of unit length, so that $UU^T = U^TU = I$. Similarly, V is a (mxm) matrix of vectors that span the model parameter space as

$$V = [\,v_1, v_2, \ldots v_m]$$

Here the v_i's are the individual orthonormal vectors, so that $VV^T = V^TV = I$. The matrix Λ is a (nxm) matrix with m eigenvalues equal to the positive square roots of m eigenvalues of A^TA. Let the eigenvalues be denoted by λ_i's. The eigenvectors u_i and v_i and eigenvalues λ_i are related to A by

$$
\begin{aligned}
A\, v_i &= \lambda_i\, u_i && i = 1, \ldots, m \\
A^T u_j &= \lambda_j\, v_j && j = 1, \ldots, m \\
A^T u_j &= 0 && j = m+1, \ldots, n
\end{aligned}
\tag{2.39}
$$

The least-squares solution, equation (2.33), involves the formation of A^TA and $A^T\Delta t$ by matrix multiplication. In terms of the SVD of A, the matrix A^TA is given by

$$
\begin{aligned}
A^TA &= (U\Lambda V^T)^T (U\Lambda V^T) \\
&= V \Lambda^T \Lambda V^T
\end{aligned}
\tag{2.40}
$$

where $\Lambda^T\Lambda$ is a (mxm) diagonal matrix containing at most m positive squares of the eigenvalues, λ_i^2 of A^TA. since λ_i is a nonnegative squareroot of the eigenvalues of A^TA, they are unique and equal to the singular values. Also it can be noted that V diagonalizes A^TA. Similarly

$$
A A^T = U \Lambda \Lambda^T U^T \tag{2.41}
$$

and therefore U diagonalizes AA^T.

Also, since U and V are nonsingular matrices, it follows that A and Λ have the same rank. This is because of the fact that multiplying a matrix on either side by a nonsingular matrix does not alter its rank. This also implies that the rank of a matrix is equal to the number of nonzero eigenvalues.

The least-squares solution in terms of U, V, and Λ is given by

$$
\begin{aligned}
\delta &= (A^TA)^{-1} A^T \Delta t \\
&= (V \Lambda^T \Lambda V^T)^{-1} (U \Lambda V^T)^T \Delta t \\
&= V (\Lambda^T \Lambda)^{-1} V^T V \Lambda^T U^T \Delta t \\
&= V (\Lambda^T \Lambda)^{-1} \Lambda^T U^T \Delta t
\end{aligned}
\tag{2.42}
$$

This solution δ can be expanded as the weighted vector product sum

$$\delta = \frac{1}{\lambda_1} v_1 u_1^T \Delta t + \frac{1}{\lambda_2} v_2 u_2^T \Delta t + \ldots\ldots\ldots + \frac{1}{\lambda_m} v_m u_m^T \Delta t \tag{2.43}$$

Let $y_i = u_i^T \Delta t$ (i = 1, ...m) be the magnitude of the projection of the discrepancy vector Δt onto the i^{th} observation eigenvector u_i; then

$$\delta = \frac{y_1}{\lambda_1} v_1 + \frac{y_2}{\lambda_2} v_2 + \ldots\ldots\ldots + \frac{y_m}{\lambda_m} v_m \tag{2.44}$$

From this expression it is clear that the solution vector δ is the weighted sum of eigenvectors v_i with weights y_i/λ_i. Small values of y_i/λ_i have relatively little influence on δ, but if λ_i is very small, then y_i/λ_i will be very large (unless y_i is very small simultaneously) and the term $(y_i/\lambda_i)v_i$ will have a dominant influence on the solution vector δ. There are two ways to avoid the dominant influence of the small values of λ_i: (i) removing it altogether; (ii) reducing its influence by making use of the Marquardt's damping factor.

The linearization procedure has several drawbacks:

1. It may converge very slowly; that is, a very large number of iterations may be required before the solution stabilizes even though the sum of squares of the residuals may decrease consistently. This sort of behavior is not common but may occur.

2. It may oscillate widely; continually reversing direction, and often increasing, as well as decreasing the sum of squares. Nevertheless the solution may stabilize eventually.

3. It may not converge at all and even diverge, so that the sum of squares increases iteration after iteration without bound.

Thie linearization method is, in general, a useful one and allows to solve successfully many nonlinear problems. In cases when it does not seem to work, one should consider either a reparameterization of the model or the use of Marquardt's method.

2.2.4 Treating ill-conditioned Matrices

If the matrix A^TA is ill-conditioned, i.e. if some of the eigenvalues are small, then we can partition Λ into a submatrix Λ_p of p nonzero singular values and several zero matrices as (Aki and Richards, 1980)

$$\Lambda = \begin{bmatrix} \Lambda_p & 0 \\ 0 & 0 \end{bmatrix} \tag{2.45}$$

where Λ_p is a (pxp) diagonal matrix. Similarly U and V can be partitioned into

$$\begin{aligned} U &= [\, U_p \quad U_0 \,] \\ V &= [\, V_p \quad V_0 \,] \end{aligned} \tag{2.46}$$

where U_p and V_p consist of first p columns of U and V respectively, corresponding to the nonzero eigenvalues, and U_0 and V_0 are the eigenvectors corresponding to zero eigenvalues. The decomposition of A then becomes

$$\begin{aligned} A &= U \Lambda V^T \\ &= [\, U_p \quad U_0 \,] \begin{bmatrix} \Lambda_p & 0 \\ 0 & 0 \end{bmatrix} \begin{bmatrix} V_p^T \\ V_0^T \end{bmatrix} \\ &= U_p \Lambda_p V_p^T \end{aligned} \tag{2.47}$$

and the least-squares solution is given by

$$\delta = V_p \Lambda_p^{-1} U_p^T \Delta t \tag{2.48}$$

One should note here that $U_p{}^T U_p = V_p{}^T V_p = I$ (orthogonality), but since Up and Vp are no longer complete, $U_p\, U_p{}^T \neq I$, and $V_p\, V_p{}^T \neq I$. The above results show that A can be constructed from U_p and V_p space alone.

If there is no U_0 space, one can always find a solution that satisfies $\Delta t = A\, \delta$, because then the U_p space is complete. However if the U_0 space exists and if the data have

components in the U_0 space, the predicted data ($A\delta$) cannot match the observed data for any choice of m, because $A\delta$ has no component in U_0. Therefore U_0 space is the source of discrepancy between the observed data and the predicted data. Similarly the V_0 space gives rise to the nonuniqueness in determining the model from the observed data, since any vector can be added in V_0 space without contradicting the observations.

2.2.5 Marquardt's Method

When the matrix A^TA is nearly singular, an alternate form of the least-squares problem is solved. In this case the sum of the squares of the parameter change vector δ is bounded by a finite quantity. This approach was first introduced by Levenberg (1944) and later Marquardt (1963) gave a detailed account of the method. Lawson and Hanson (1974) and Jupp and Vozoff (1975) have also discussed this method of avoiding singularities. This technique of suppressing the undesirable effect of small eigenvalues is called damped least-squares method or "ridge regression". In this technique a constant k is added to the diagonal elements of the matrix A^TA. The constant prevents unbounded oscillations in the solution. The modified least-squares equation is given by

$$(A^TA + kI)\,\delta = A^T\,\Delta t \tag{2.49}$$

and the solution is

$$\delta = (A^TA + kI)^{-1}\,A^T\,\Delta t \tag{2.50}$$

writing $(A^TA + kI)$ in terms of U, Λ,and V

$$\begin{aligned}(A^TA + kI) &= V\Lambda^T\Lambda V^T + kI \\ &= V(\Lambda^T\Lambda + kI)V^T\end{aligned} \tag{2.51}$$

Hence

$$(A^TA+kI)^{-1} = V(\Lambda^T\Lambda+kI)^{-1}V^T$$

$$= V\,\mathrm{diag}\left(\frac{1}{\lambda_1^2+k}, \ldots, \frac{1}{\lambda_m^2+k}\right)V^T \tag{2.52}$$

where $(\Lambda^2+kI)^{-1}$ is a diagonal matrix of the form

$$(\Lambda^T\Lambda+kI)^{-1} = \begin{bmatrix} \frac{1}{\lambda_1^2+k} & 0 & \ldots. & 0 \\ 0 & \frac{1}{\lambda_2^2+k} & \ldots. & 0 \\ .. & \ldots & \ldots. & . \\ 0 & 0 & \ldots. & \frac{1}{\lambda_m^2+k} \end{bmatrix} \tag{2.53}$$

Then the least-squares solution becomes

$$\delta = V\,\mathrm{diag}\left(\frac{1}{\lambda_1^2+k}, \ldots, \frac{1}{\lambda_m^2+k}\right)V^T\,(U\Lambda V^T)^T\,\Delta t$$

$$= V\,\mathrm{diag}\left(\frac{1}{\lambda_1^2+k}, \ldots, \frac{1}{\lambda_m^2+k}\right)\Lambda^T U^T\,\Delta t \tag{2.54}$$

By comparing equation (2.42) with (2.54), one can see that the Marquardt's damped least-squares technique is obtained by replacing $(1/\lambda_i)$ in the $((\Lambda^T\Lambda)^{-1}\Lambda^T)$ matrix by

$$\frac{\lambda_i}{\lambda_i^2+k} \tag{2.55}$$

where k is the Marquardt's damping factor. In this case even if λ_i approaches zero , the division by zero does not occur. Thus k obviates the problem of matrix singularities.

Addition of constant k to the diagonal elements of A^TA does not allow the eigenvalues

to become zero. The constant k is called a damping factor because it damps out the negligibly small eigenvalues and prevents the matrix A^TA from becoming singular. Thus a large k increases the stability of the solution but decreases the resolution of the model parameters. Hence to achieve best results, k should be chosen as small as possible, but large enough to stabilize the solution.

It is very important to find an appropriate value for the constant k, since it controls the stability and resolution. Lines and Treitel (1984) have suggested that the iterative process should start with a value of k less than 1. Then, after each iteration the value of k should be reduced by multiplying it with a reduction factor, also less than 1. A typical initial choice of k would be 0.3 with a reduction factor of 0.5. This method is always found to produce good results.

Hoerl et al. (1975) proposed an algorithm for the automatic selection of k. They use the expression

$$k = \frac{p\,\sigma_d^2}{M^TM} \tag{2.56}$$

where σ_d^2 is the least-square estimator of the variance in the data, M is the least-squares solution and p is the number of nonzero eigenvalues. σ_d^2 is obtained by

$$\sigma_d^2 = \frac{\phi(0)}{N - p} \tag{2.57}$$

where N is the number of observations and $\phi(0)$ is the residual sum of squares for the least-squares estimate and is given by

$$\phi(0) = (\Delta t - A\,\delta)^T (\Delta t - A\,\delta) \tag{2.58}$$

This estimate of k was also shown to produce very good results, although it does not always guarantee stability and convergence. It will be shown later that sometimes this method works better and sometimes the other method works better.

To speed the convergence when solving the normal equations and also to avoid ill conditioning caused by different scales in which the model parameters are expressed, scaling can be employed. Each column of the matrix A is scaled by a root mean sum of squared values d_j, defined as follows

$$d_j = \left[\sum_{i=1}^{N} A_{ij}^2 \right]^{1/2} \tag{2.59}$$

The scaling is applied to each element of A by

$$A_{ij}^{(scaled)} = A_{ij} / d_j \tag{2.60}$$

The effect of scaling is to reduce numerical inaccuracies such that all the model parameters will be scaled in the same way. The estimates of parameters from the scaled matrix are then transformed back to original parameters by

$$\delta_j = \delta_j^{(scaled)} / d_j, \qquad j = 1, ..., m. \tag{2.61}$$

2.2.6 Resolution and Covariance Matrices

The performance of a method cannot be judged without the knowledge of the uniqueness and reliability of the solution. Backus and Gilbert (1967, 1968, 1970) introduced the concepts of the resolution of a particular solution and the trade off between the resolution and error due to the noise in the data. Jackson (1972), Aki and Richards (1980) and Kanasewich (1981) have discussed these concepts for a discrete data set. For the discrete case considered here the concepts of data resolution matrix, model resolution matrix and covariance matrix are as follows.

According to equation (2.28), the basic problem is obtaining the solution of $\Delta t = A\,\delta$. An estimate of δ, the correction vector, is obtained by operating on Δt with a matrix H, i.e.

$$\delta^{est} = H\,\Delta t \tag{2.62}$$

Since the matrix H solves the inverse problem $\Delta t = A\,\delta$, it is called the generalized inverse. The generalized inverse of the overdetermined (n>m) least-square problem is (equation 2.33)

$$\begin{aligned} H &= (A^T A)^{-1} A^T \\ &= V \Lambda^{-1} U^T \end{aligned} \tag{2.63}$$

and the inverse operator H for damped least-squares problem is given by

$$\begin{aligned} H &= (A^T A + k I)^{-1} A^T \Delta t \\ &= V\, \mathrm{diag}\left(\frac{1}{\lambda_1^2 + k}, \ \ldots, \frac{1}{\lambda_m^2 + k} \right) \Lambda^T U^T \end{aligned} \tag{2.64}$$

Suppose we have found an estimate for δ. Then, we want to know how well this estimate fits the data. By substituting δ^{est} in $\Delta t = A\,\delta$, we obtain

$$[\Delta t]^{calc} = A\,\delta^{est} = A\,H\,\Delta t = N\,[\Delta t]^{obs} \tag{2.65}$$

Here the superscripts 'calc' and 'obs' mean calculated and observed respectively. The n x n matrix N (= A H) is called the data resolution matrix and it describes how well the calculated data match the observed data. If $N = I_{nxn}$ then $[\Delta t]^{calc} = [\Delta t]^{obs}$ and there is no error in inversion. The matrix N in terms of U, V and Λ is given by

$$\begin{aligned} N &= A\,H \\ &= U \Lambda V^T\, V \Lambda^{-1} U^T \\ &= U\,U^T \end{aligned} \tag{2.66}$$

Wiggins (1972) calles N the information density matrix because it shows if some of the data is redundant. If several eigenvalues of the matrix A are zero, then

$$N = U_p U_p^T \tag{2.67}$$

where p is the number of nonzero eigenvalues. In this case the predicted data cannot match

the observed data.

The data resolution matrix characterizes whether the data can be independently predicted or resolved. The same question can be asked about the estimate of δ. Suppose there is a true but unknown set of δ^{true} that solves

$$A\,\delta^{true} = [\,\Delta t\,]^{obs} \tag{2.68}$$

then substituting this in equation (2.62)

$$\begin{aligned}\delta^{est} &= H\,[\,\Delta t\,]^{obs} \\ &= H\,A\,\delta^{true} \\ &= R\,\delta^{true}\end{aligned} \tag{2.69}$$

Here R (= H A) is the m x m model resolution matrix. If R = I, then each δ^{est} is uniquely determined and so are the model parameters. If R is not an identity matrix, then the estimates of the parameters are really weighted averages of the true parameters. In terms of U, V and Λ

$$\begin{aligned}R &= H\,A \\ &= V\,\Lambda^{-1}\,U^T\,U\,\Lambda\,V^T \\ &= V\,V^T\end{aligned} \tag{2.70}$$

For p nonzero eigenvalues

$$R = V_p\,V_p^T \tag{2.71}$$

The model resolution matrix R for a damped least-squares formulation is given by

$$R = V_p\,\frac{\Lambda_p^2}{\Lambda_p^2 + k\,I}\,V_p^T \tag{2.72}$$

This shows that the introduction of damping factor k degrades resolution, but the solution is stabilized.

Finally the reliability of the solution is judged by its covariance matrix. The error δ in

the solution due to error Δt in traveltime data can be written as

$$\delta = H \Delta t \tag{2.73}$$

Therefore their covariance matrices are related by

$$< \delta \delta^T > = H < \Delta t \Delta t^T > H^T \tag{2.74}$$

Assuming that all components of the data vector are statistically independent and share the same variance σ_d^2, then

$$\begin{aligned} < \delta \delta^T > &= \sigma_d^2 H H^T \\ &= \sigma_d^2 V \Lambda^{-1} U^T (V \Lambda^{-1} U^T)^T \\ &= \sigma_d^2 V \Lambda^{-2} V^T \end{aligned} \tag{2.75}$$

for p nonzero eigenvalues

$$< \delta \delta^T > = \sigma_d^2 V_p \Lambda_p^{-2} V_p^T \tag{2.76}$$

Obviously the covariance of the solution becomes large when the eigenvalues are small. For the damped least-squares solution the covariance matrix is given by

$$< \delta \delta^T > = \sigma_d^2 V_p \frac{\Lambda_p^2}{(\Lambda_p^2 + k I)^2} V_p^T \tag{2.77}$$

The introduction of the damping factor k decreases the covariance by damping out the small eigenvalues. Thus the damping factor k introduces a tradeoff between the resolution and covariance. As k increases the resolution decreases but the covariance matrix is improved.

2.3 Synthetic Tests

To check the algorithm a test was made using a three layer model as shown in Figure 2.2. The first interface is a dipping plane while the second and third interfaces are defined by second order polynomial. The velocities at the top of each layer are 2.0, 3.5 and, 4.5 km/sec respectively. The velocity gradients in each layer are 0.6, 0.4 and, 0.2 km/sec/km respectively. To generate the traveltime data for three dimensional inversion we took the receivers in the form of a 5 by 5 grid (Figure 2.3). The source is located at the center and the grid spacing is 2 km. With this source receiver configuration the data was generated for 9 shot locations (Figure 2.4). Figure 2.5 shows the rays for one shot location.

The traveltimes to different layers were generated for the model with the specified source receiver configuration. The inversion was carried out by taking as initial guess a perturbed version of the original model. The parameters of the upper layers are first determined and held constant while solving for the structure and velocity with gradient for the lower layers. This approach is called the layer-stripping method and it provides speed and stability to the inversion algorithm since there are fewer parameters involved. For the purpose of detailed testing of the algorithm the third interface was chosen as the target horizon i.e. the interface parameters and velocity with gradient in this layer were to be determined. The parameters of the first two interfaces were assumed to be known and hence they were kept constant during the inversion.

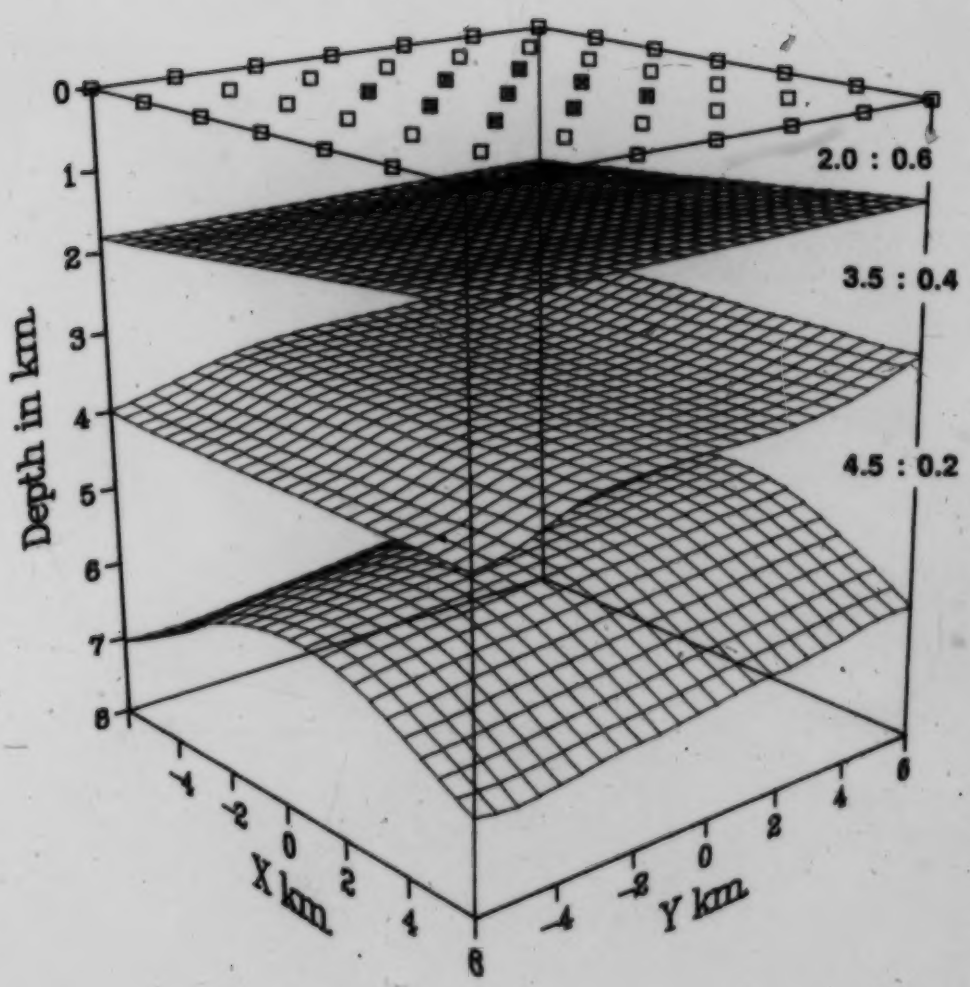

Figure 2.2 A three layer model for testing the inversion procedure. The first interface is a dipping plane while the second and third interfaces are defined by second order polynomial. The velocities at the top of layers 1, 2, and 3 are 2.0, 3.5, and 4.5 km/s respectively and the velocity gradients are 0.6, 0.4, and 0.2 km/s/km respectively.

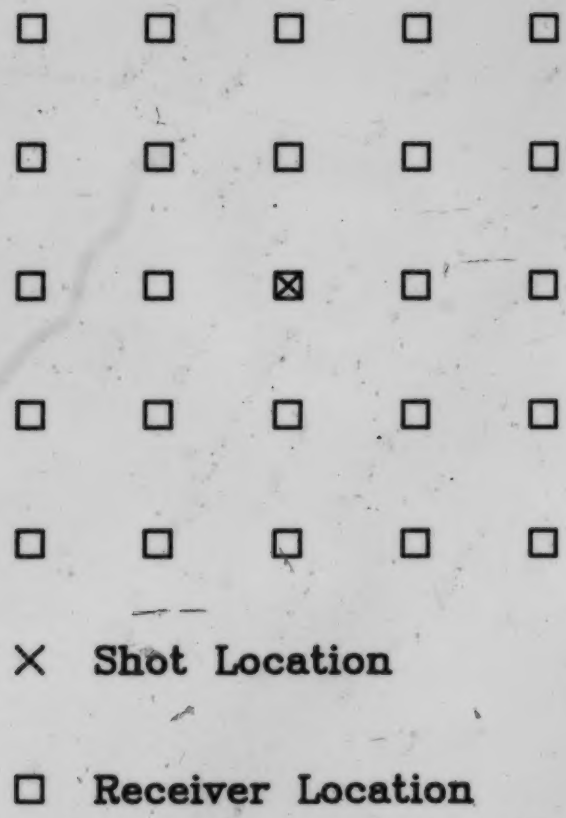

Figure 2.3 Source receiver configuration for each shot. The receivers are in the form of a 5 X 5 grid and the grid spacing is 2 km. The shot is located at the center and is marked by X.

Figure 2.4 Source receiver configuration for generating synthetic traveltime data for the model of Figure 2.2.

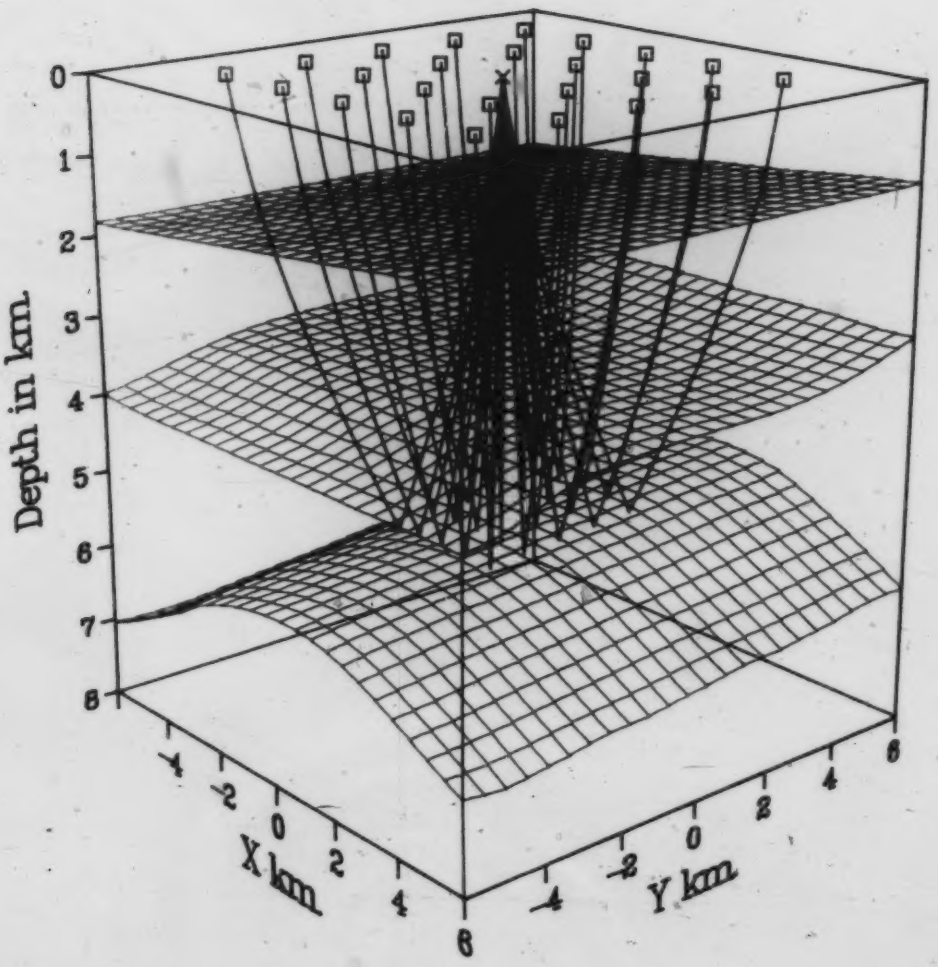

Figure 2.5 Rays from source to receivers for one shot location.

The traveltime data for the third interface was generated and input to the inversion algorithm. An initial guess for the parameters of the third layer was also input to the algorithm. The objective was to reconstruct iteratively the velocity, its gradient and the parameters of the third interface. The calculated model should approach the real model as the number of iterations increase. Figures 2.6a to 2.6d show how the residual times (in milliseconds) between the calculated and known model change after each iteration. The residual times have almost dropped to zero after four iterations and the calculated model converged to the actual model.

Next the effect of random noise on the inversion algorithm was tested. Random numbers having standard deviation of 20 msec (with uniform, Gaussian distribution) were added to the traveltime data. We found that the convergence rate in case of noisy data was slow and after 8 iterations the residual times dropped below 20 msec. There is no point in iterating further since the standard deviation of the noise is just 20 msec. We found also cases when the inversion was unstable due to the presence of noise. In such cases a higher value of the damping factor had to be used.

The synthetic model results shown above lead to the following conclusions. In the case of noise-free data it is possible to obtain the velocity, its gradient and the shape of the interfaces simultaneously. But for the data contaminated by random noise it is usually not possible to obtain all the parameters simultaneously from the reflection data unless the initial guess is very close to the actual parameters. Besides, the noise affects the stability and the resolution of the algorithm, but the estimated parameters satisfy the observations in a least squares sense. The flow chart of the tomographic algorithm is shown in Figure 2.7.

The inversion algorithm is stable in the sense that small changes in the initial data produce correspondingly small changes in final results. Efficiency of the ray tracing algorithm can be judged from the fact that it takes about 4.5 seconds of CPU time on Amdahl 5870 to trace rays for 225 source-receiver pairs. Each iteration requires 9.0 secs.

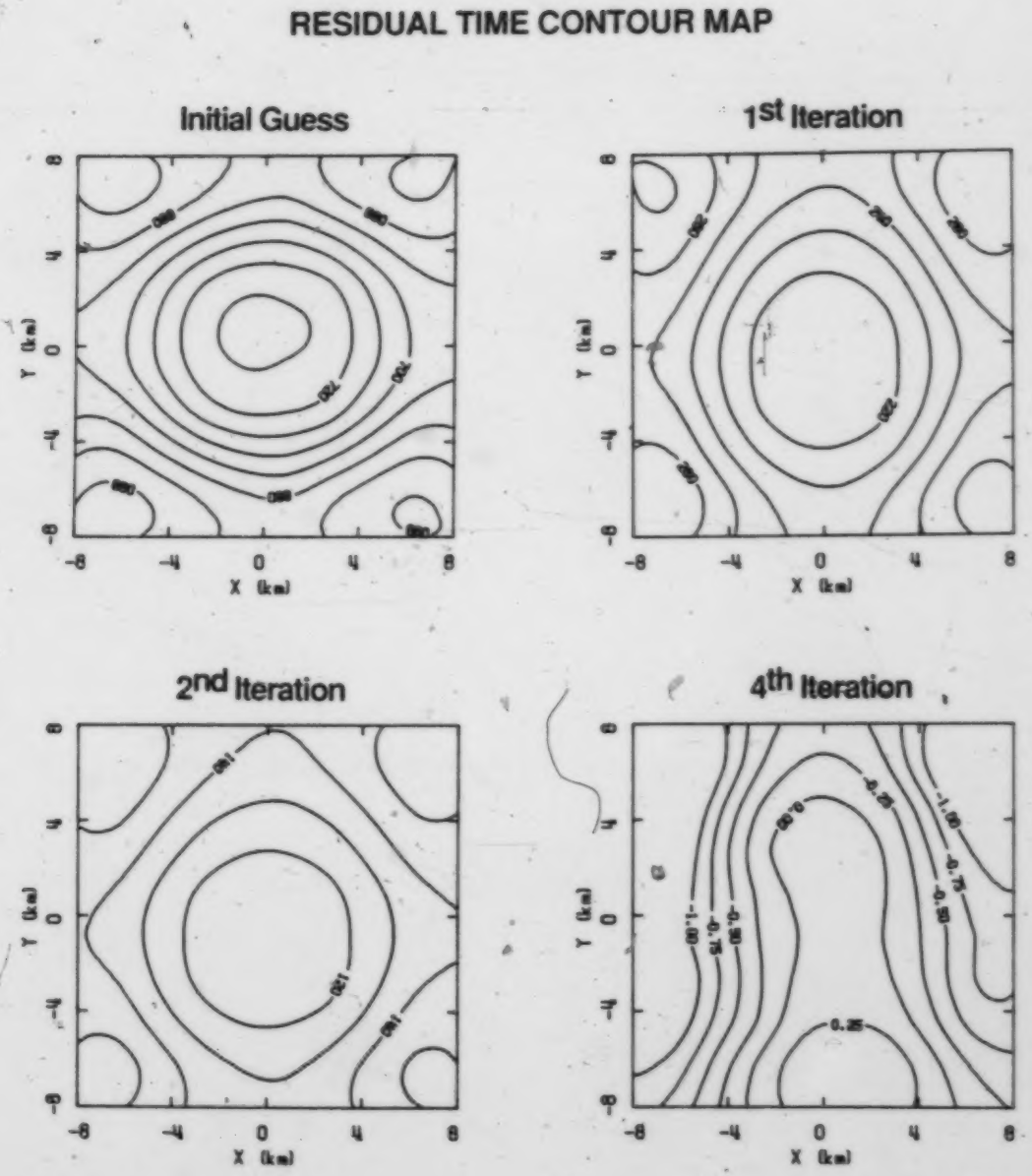

Figure 2.6 Residual time contour maps (in milliseconds) after each iteration for one shot.

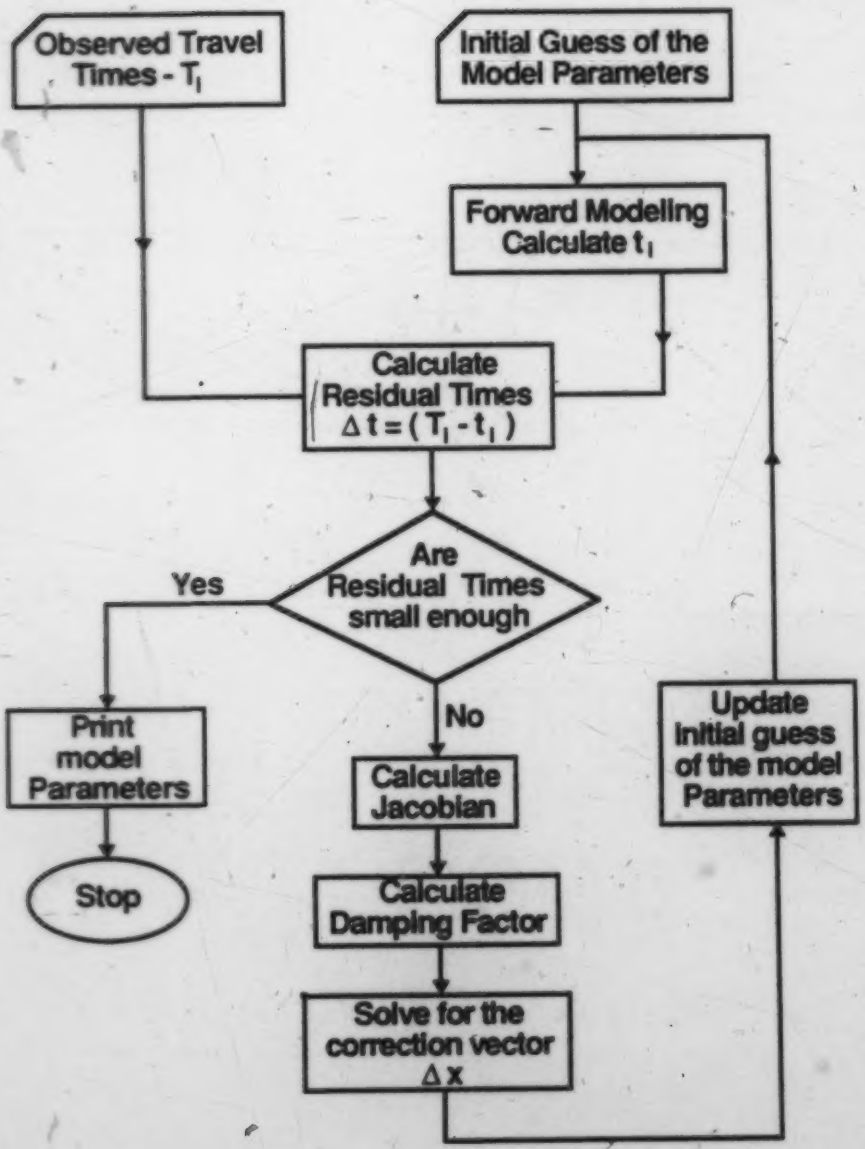
Observed Travel Times - T_i
Initial Guess of the Model Parameters
Forward Modeling Calculate t_i
Calculate Residual Times $\Delta t = (T_i - t_i)$
Are Residual Times small enough
Yes
No
Print model Parameters
Stop
Calculate Jacobian
Calculate Damping Factor
Solve for the correction vector Δx
Update initial guess of the model Parameters

Figure 2.7 Flow chart for the tomographic algorithm.

2.4 Application to Vancouver Island data

2.4.1 Tectonics of west coast of Canada

The plate tectonic regime of west coast of Canada is extremely complex and has been the focus of many geological and geophysical studies. The essential features of the plate tectonic environment are dominated by the relative motion of two large lithospheric plates and two micro plates. The large segments are the Pacific and North America plates. The smaller Juan de Fuca plate and a northern part, which has been named the Explorer plate, have been shown to be moving independently. They were once part of a larger oceanic plate of lithosphere. A comprehensive review is given by Keen and Hyndman (1979). Figure 2.8 shows a tectonic map of this area.

In the vicinity of Vancouver Island, the oceanic Juan de Fuca and Explorer plates are being obliquely subducted beneath the continental North America plate at convergence rates of 2 to 4 cm/yr. The motion between the Juan de Fuca and Explorer plates occurs across the Nootka transform fault zone, which extends northeasterly from the north end of the Fuca ridge to the continental shelf off north central Vancouver Island. The active portion of the fault zone, about 20 km wide, has produced extensive disturbance in the 0.5 to 1.0 km of overlying sediments. Hyndman, Riddihough and Herzer (1979) showed that the magnetic anomaly pattern required the fault to have a strike-slip motion of about 3 cm/yr, with subduction at the margin being more rapid to the south than to the north of the fault zone.

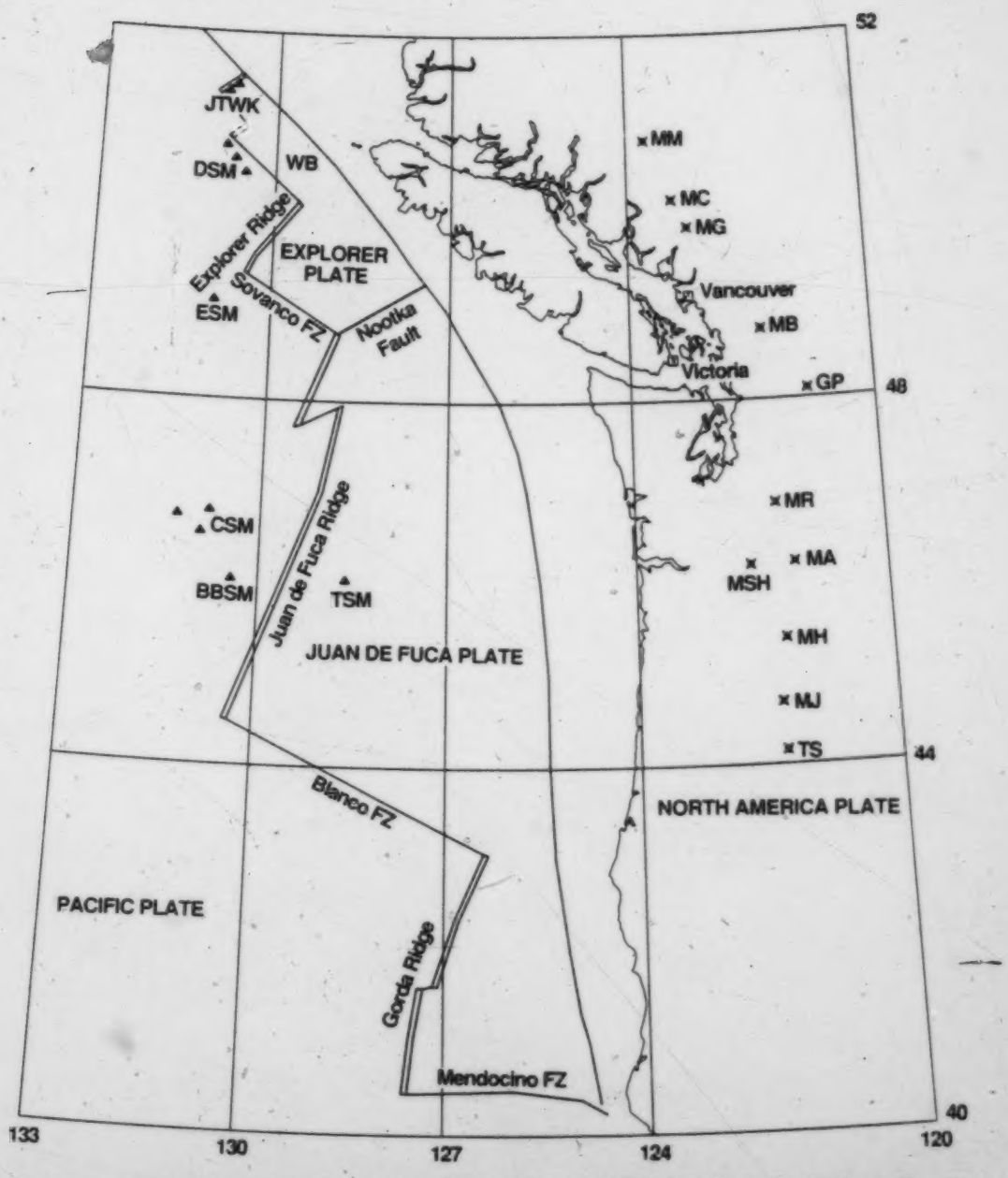

Figure 2.8 Tectonic map of the west coast of Canada. JTWK-J. Tuzo Wilson Knolls, DSM-Dellwood Seamounts, WB-Winona Basin, ESM-Explorer Seamount, CSM-Cobb Seamounts, BBSM-Brown Bear Seamount, TSM-Thompson Seamount, MM-Meager Mountain, MC-Mount Cayley, MG-Mount Garibaldi, MB-Mount Baker, GP-Glacier Peak, MR-Mount Rainier, MA-Mount Adams, MSH-Mount St. Helens, MH-Mount Hood, MJ-Mount Jefferson, TS-Three-Sisters, FZ-Fracture Zone.

Most subduction zones in other regions are characterized by a deep trench, but there is no such deep trench in this region. With the evidence of a lack of a deep margin trench and deep earthquakes in this zone, Riddihough (1978) suggested that the subduction might be a very recent geological feature, and the absence of a deep trench was probably due to high sedimentation rates and the damming effect of the Juan de Fuca ridge lying only a few 100 km offshore.

2.4.2 Application of Tomography

A reflection survey was carried out on Vancouver island as a part of Project LITHOPROBE-1. LITHOPROBE is a geoscientific research program where the objective is to study the three dimensional properties of the lithosphere. For this purpose four Vibroseis lines were shot in 1984. The tomographic method was applied to the traveltime data from one of a set of four Vibroseis lines to determine the structure and velocities of different layers underneath the island, which might be of great significance to understand the tectonics. The seismic instrumentation consisted of a 120-channel DFS-V digital recording system which employed 4 synchronized vibrator sources and a geophone array with a 90 m group spacing. The source array was about 180 m long and was generated by moving four vibroseis units 16 times to produce a single field record stack. An upsweep of 8 to 40 Hz over a 16 seconds duration was used for the vibrators. A 32 seconds listen time was used to produce records to 16 seconds.

The inset of Figure 2.9 shows a map of Vancouver Island along with the location of the four Vibroseis lines. Figure 2.9 shows an expanded view of a portion of line 1 with the source and receiver locations. Solid squares are sources and open squares are receivers. +'s indicate the source receiver midpoint locations. Although this is a two-dimensional reflection survey, it is possible to obtain a three-dimensional structure because the sources and receivers are on a crooked line. The reflection midpoints (indicated by +'s) cover a

three-dimensional surface. Therefore, if the traveltimes to various reflecting horizons are picked from the prestack data then a three-dimensional picture of the subsurface can be obtained by inverting this data.

Figure 2.10 shows an example of the excellent original vibroseis field data. There are two prominent bands of reflectors located approximately at 5 and 8 seconds. These two major reflectors are quite uniform and consistent throughout all four lines from Vancouver island. The reflector at 5 sec is labelled 'C' and is the first reflector to be used for this tomographic study. It is called the "decollement zone". The second reflector labelled "E" is thought to be the underthrusting oceanic crust which is currently subducting under the west coast.

Previous studies (McMechan and Spence 1983, Clowes et al. 1984, Spence et al. 1985) indicate that the surface layer of Mesozoic volcanics and sediments in this region is nearly horizontal and its thickness is about 1.5 km. The velocity at the surface is about 5.4 km/s and the velocity gradient in this layer is 0.6 km/s/km. Therefore, the first layer is assumed to be horizontal and its parameters remain constant in solving for the lower layers. Moreover from the field shot records it was not possible to pick reflection times to this horizon and hence the parameters could not be determined from inversion.

Chiu et al. (1986) carried out inversion to determine the structure and velocity of reflectors 'C' and 'E' by assuming that the velocity in each layer is constant. For the surface layer of Mesozoic volcanics and sediments, a constant velocity of 6.0 km/s was assigned. The parameters of this surface layer were constant while solving for the lower layers. At first inversion for the reflector 'C' was carried out. It was found that a plane interface was adequate to represent the reflector. The reflector 'C' in this area was found to be dipping at approximately 1.6 degrees to the northeast, with a minimum depth of about 14 km and with an interval velocity of 6.54 km/s.

Figure 3.10 (a) and (b) are the synthetic records with added noise for the model of Figure 3.3. SP is the location of the shotpoint. The vertical scale is the two-way travel time in seconds. (c) and (d) are the CMP stacks of synthetic records without and with added noise respectively.

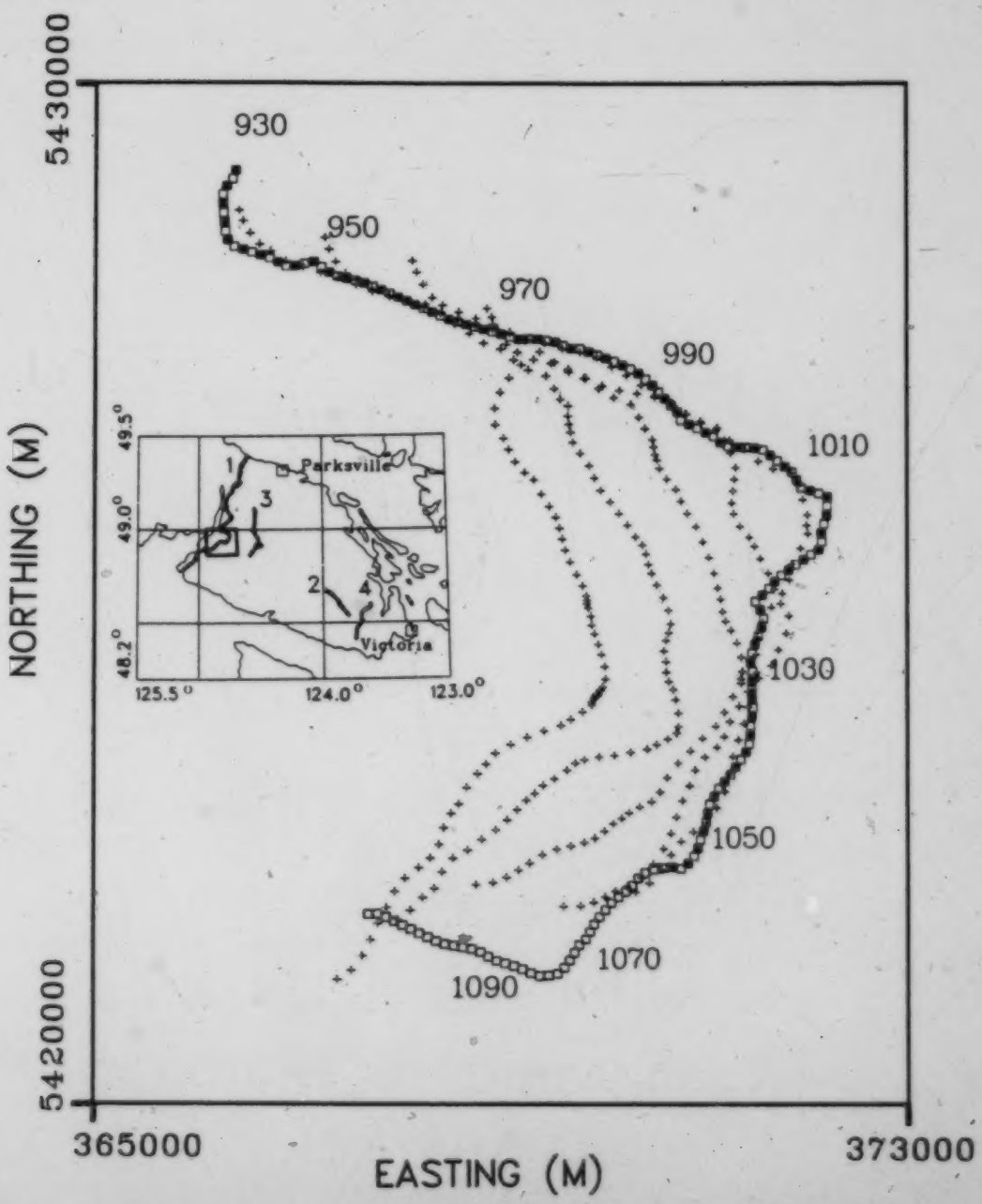

Figure 2.9 An expanded view of a portion of line 1 with the source and receiver locations. Solid squares are sources and open squares are receivers. +'s indicate the source-receiver midpoint locations. The inset shows a map of Vancouver Island along with the location of the four Vibroseis lines.

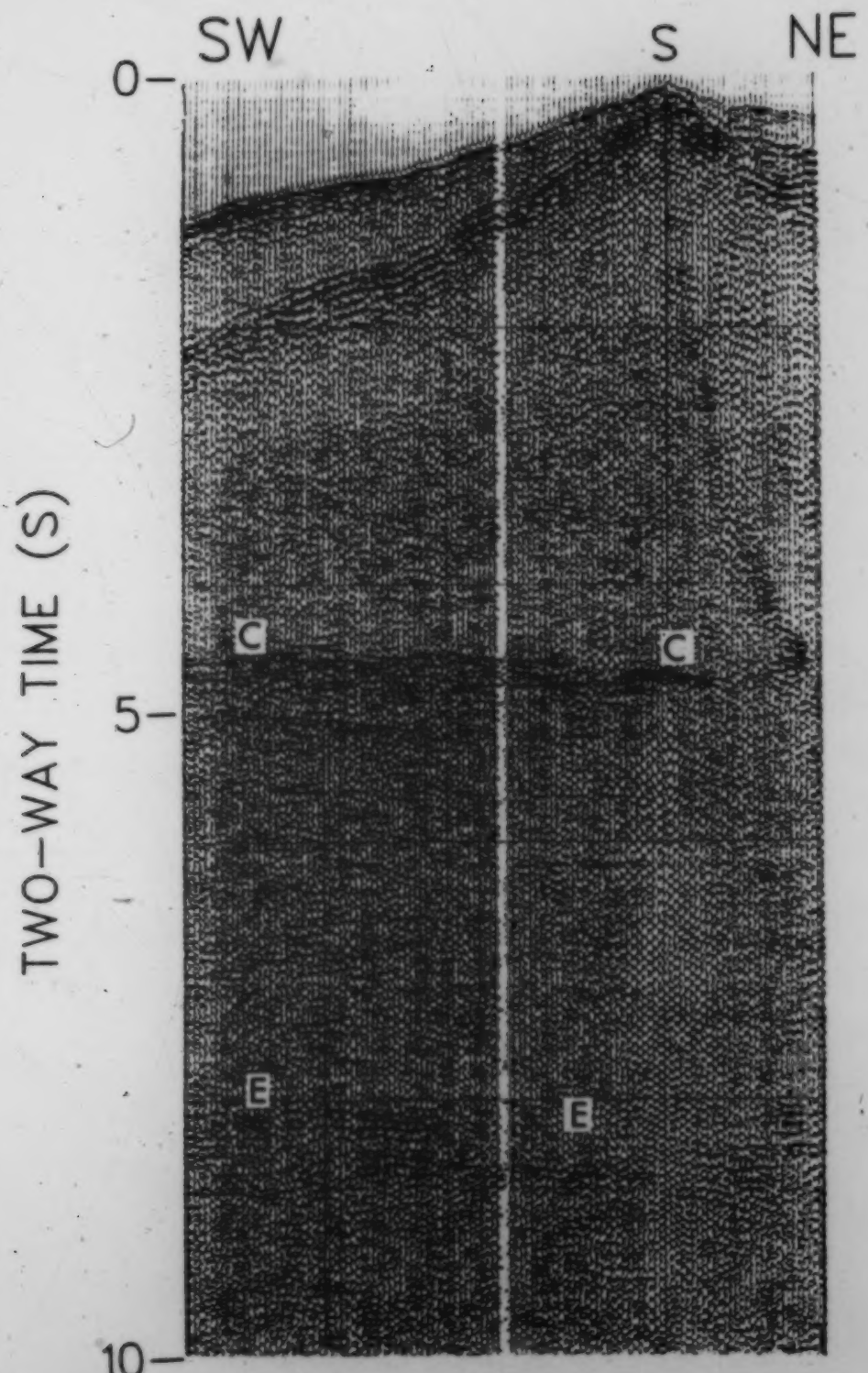

Figure 2.10 An example of the excellent original Vibroseis field data.

Inversion of the reflector 'E' was achieved by freezing the model parameters for the first two layers. For this reflector also a plane reflector was adequate to fit the observations. This reflector was found to dip approximately 8.4 degrees to the northeast with a minimum depth of 25 km and with an interval velocity of 6.75 km/s.

Table 2.1 shows a comparison of the velocity models obtained under the assumption

TABLE 2.1

A comparison of velocity models of Chiu et al. (1986) and Clowes et al. (1984)

Layer No.	Minimum Depth(km)		Velocity(km/s)		Dip (NE)	
	Chiu et al.	Clowes et al.	Chiu et al.	Clowes et al.	Chiu et al.	Clowes et al.
1	1.5	1.5	6.0	5.4 - 6.4	0°	0°
2	14.0	15.6	6.54	6.4 - 6.75	1.6°	2° - 4°
3	25.0	25.6	6.75	7.7	8.4°	7° - 10°

of constant velocity layers with the model of Clowes et al. (1984). The discrepancy in the two models led us to believe that the assumptions regarding interval velocities were inaccurate. The present work introduces velocity gradients in each layer.

The inversion of the traveltime data was carried out to determine the structure and velocity with gradients of the above reflectors C and E. Approximately 110 traveltimes were picked in the area indicated by Figure 2.9 for both C and E reflectors from the original field recordings. The error in picking traveltimes is of the order of 20 milliseconds. The error distribution can be assumed Gaussian since the picked time corresponds to the peak on the reflected pulse. To determine the structure and velocity with gradients on the decollement zone we assumed the interface to be a second order polynomial surface and also made an initial estimate of the velocity and gradient based on the previous studies. It

turned out that several of the eigenvalues corresponding to the coefficients of the second order polynomial were very small, hence we concluded that a plane was adequate to represent the interface. While inverting for the remaining parameters we found that the eigenvalues corresponding to the velocity and gradient parameters were also relatively small. Hence these parameters were constrained. The standard error dropped below 25 msecs after 8 iterations. This accuracy is good enough for the crustal seismology since the error in picking arrival times is of the order of 20 msecs. We found two parameter sets for this layer which fit the observed data in a least square sense and they are given in table 2.2. The two sets result from the two different starting models and thus show the nonuniqueness in the inversion process.

Previous models show that this horizon is almost flat. The results obtained from inversion are consistent with this because the dip of the second reflector is less than 3 degrees. However the reflection midpoints shown in Figure 2.9 cover a very small area on the interface, hence the data is not adequate to determine the true dip and strike of the interface. The noisy data as well as uncertainty in picking arrival times also affects solution.

TABLE 2.2

Parameter sets for reflector C satisfying the least-squares criterion

	Depth (km)	Velocity (km/s)	Gradient (km/s/km)	Dip	Strike
Set I	13.57	6.33	0.05	2.6°	N30°E
Set II	14.58	6.85	0.034	3.0°	N18°E

To invert for the model parameters of the reflector E the parameters of the first two layers were kept constant. Here also it was found that a plane was good enough to fit the observations. The eigenvalue corresponding to the gradient parameter was very small,

hence the third layer was assumed to be of constant velocity. The parameter sets obtained from inversion corresponding to the parameters of layer 2 (Table 2.2) are shown in Table 2.3. These results are consistent with that of Clowes et al. (1984). Figure 2.11 illustrates the structure of reflectors C and E for set II. In both cases it took about 9 iterations before the residual times dropped below 30 msecs.

TABLE 2.3

Parameter sets for reflector E satisfying the least-squares criterion

	Depth (km)	Velocity (km/s)	Dip	Strike
Set I	25.70	7.75	7.0°	N73°W
Set II	25.71	7.77	8.87°	N65.4°W

Clowes et al. (1984) have also reported the existence of the high velocity anomalous zone above the downgoing crust in the depth range of 18 to 25 kms. Figure 2.12 illustrates the preliminary generalized structural section across the subduction zone. The location of the small portion of line 1 chosen for inversion is indicated by an arrow. Spence et al. (1985) have attributed this anomalous high velocity zone to the remanents of a subducted slab, perhaps detached when the subduction zone jumped westward to its present position.

In tomography a solution is determined by comparing the observed data with the data generated from a model. If these two are the same then the solution is exact but not necessarily unique. Solutions which are unrealistic should be dropped. The model parameters of set I do not agree well with the previous refraction models. There is a discrepancy in the depth of the second reflector. The model parameters for the reflection data of set II are more similar to an independent interpretation of the refraction data than that of set I.

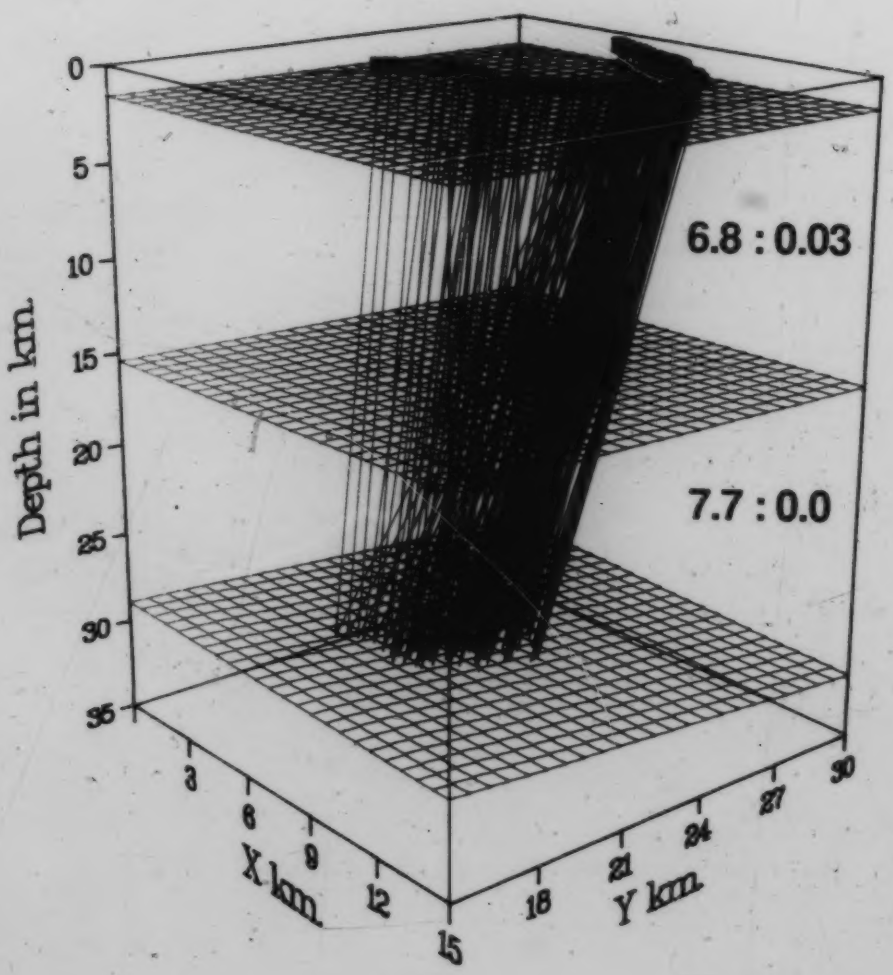

Figure 2.11 The three dimensional structure and velocity with gradient of reflector C and E for set II.

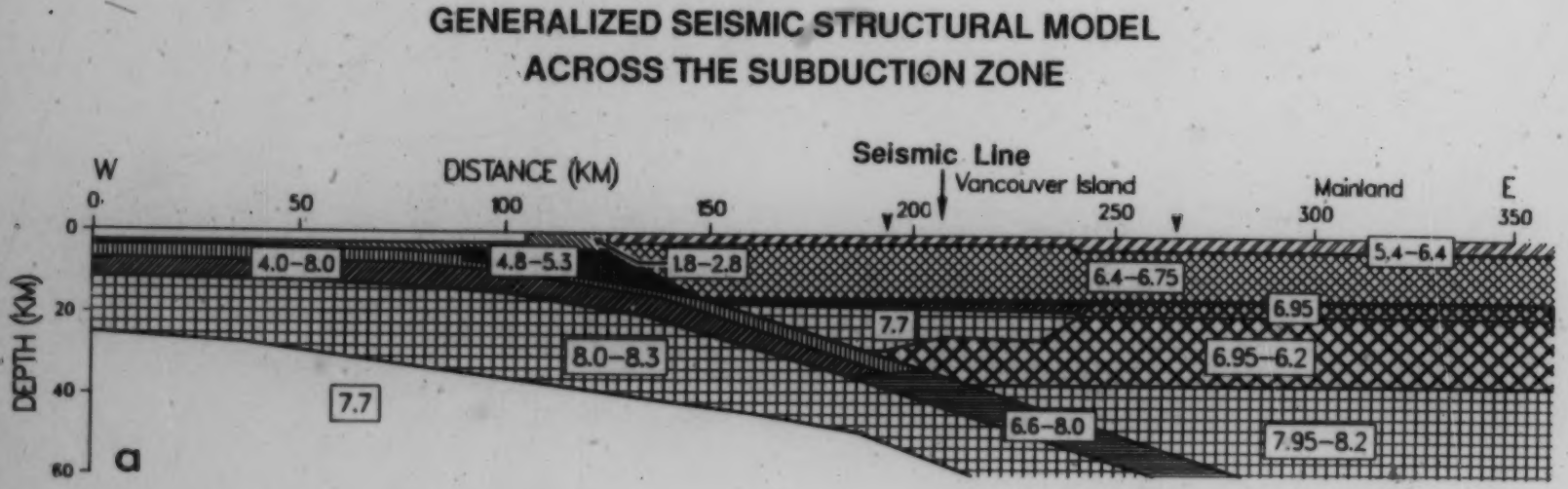

Figure 2.12 The generalized structural section across the subduction zone (Modified from Clowes et.al. 1984). The approximate location of line 1 chosen for inversion is indicated by an arrow.

Figure 2.13 shows the comparison of the velocity model obtained from inversion (set II) to that of Clowes et al. (1984). The shaded portion indicates the upper and lower bounds for the model parameters of set II. The bounds were calculated from the covariance matrices and are discussed below. There is a discrepancy in the depth and velocity parameters for reflector C. This discrepancy can not be explained at the present time since Clowes and others are redoing the interpretation with larger data set.

As described in section 2.2.6, the reliability of the damped least-squares solution is measured by its resolution and covariance matrices. The diagonal elements of the resolution matrix are useful measures of resolution. If the diagonal elements are unity then all the model parameters are uniquely determined. Otherwise the estimates of the model parameters are expressed as a weighted average of the true values. Figures 2.14a and 2.15a illustrate the resolution matrices for reflectors C and E respectively. For reflector C the parameters a_0 and v are not well determined since the corresponding elements of the resolution matrix have values of 0.513 and 0.579. Other parameters are better resolved since the corresponding elements have values close to 1. For reflector E none of the model parameters are well resolved since none of the diagonal elements of resolution matrix is close to 1. Their estimates are the weighted average of the true values. The model parameters for this layer fluctuate significantly with each iteration. Because of this instability, the ridge regression tends to produce a relatively large common damping factor to stabilize the solution. Figures 2.14b and 2.15b illustrate the covariance matrices for reflector C and E. The variances of the solution are relatively small hence the computed model parameters are fairly reliable. The square roots of the diagonal elements of the covariance matrix give the errors associated with the parameters. In Figure 2.13 the error bounds (the shaded area) for the parameters were determined by this criterion.

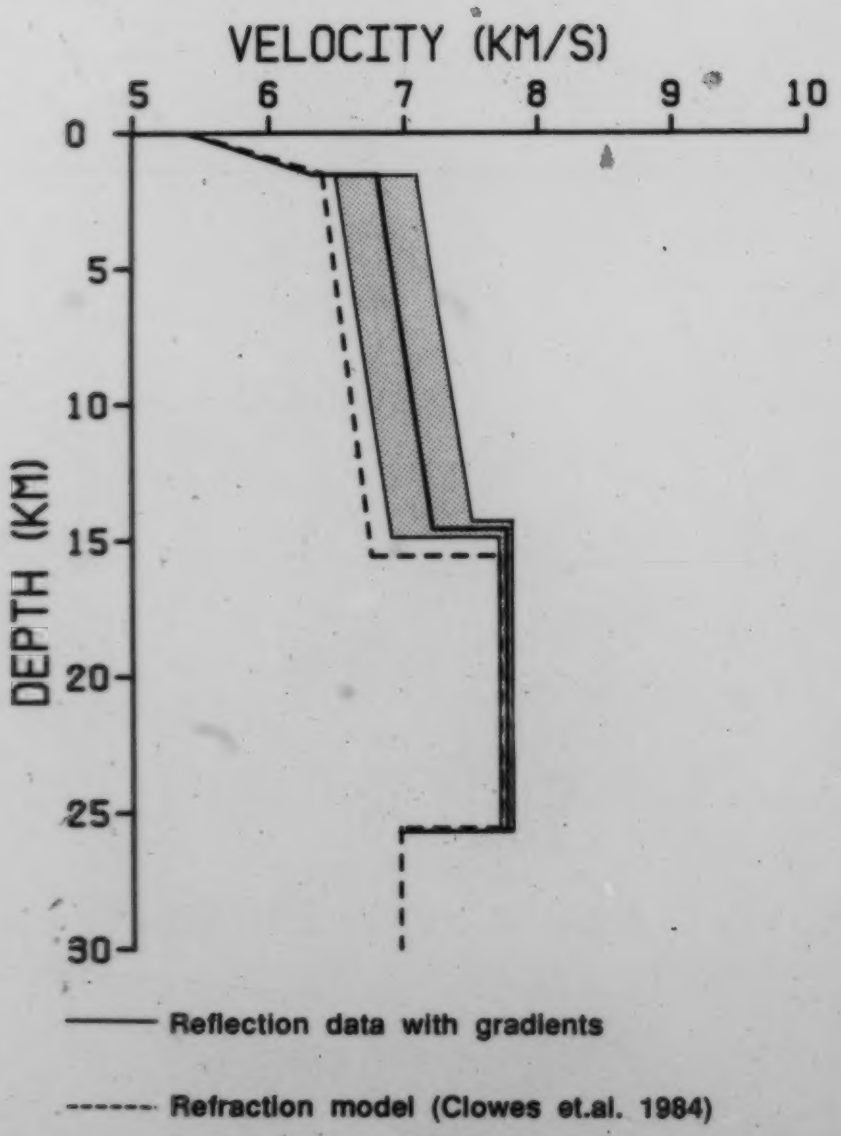

Figure 2.13 A comparison of the velocity model obtained from inversion to that of Clowes et.al. 1984.

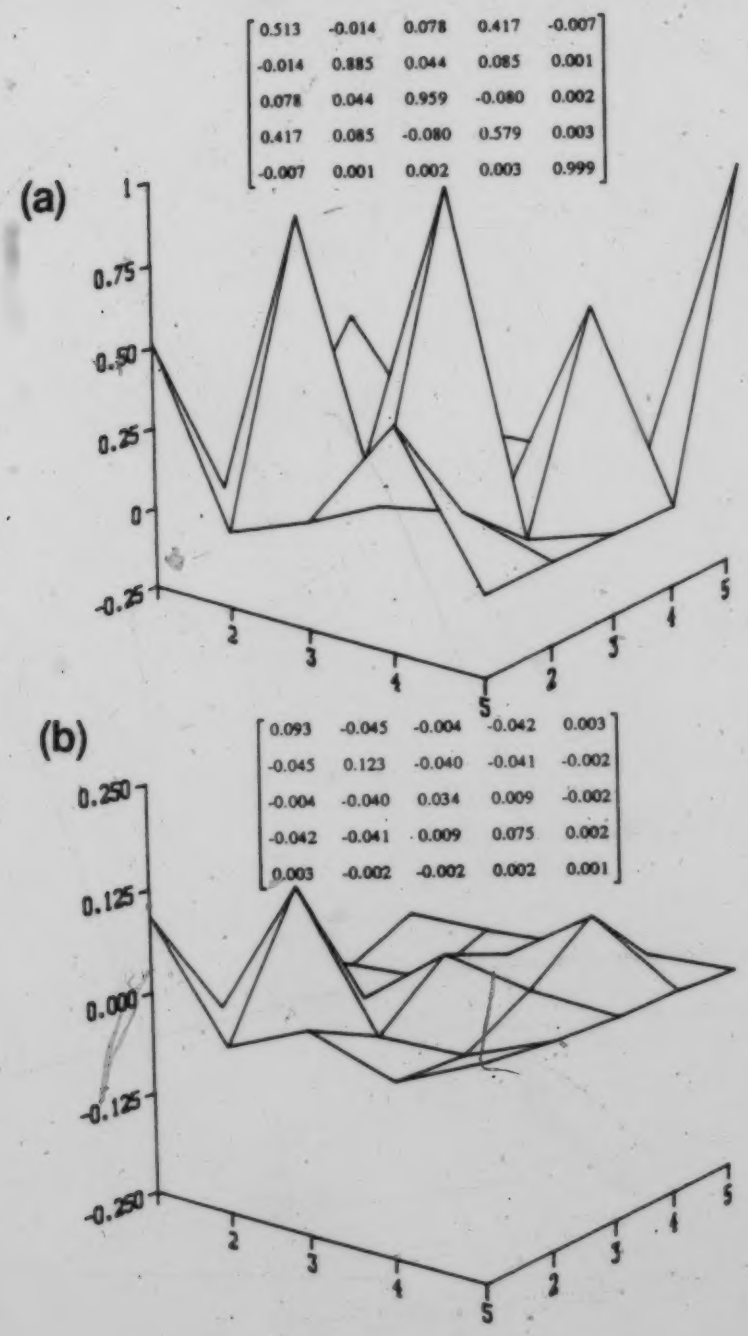

Figure 2.14 (a) The resolution matrix for reflector C. The order of the elements from 1 to 5 for the model parameters is a_0, a_{10}, a_{11}, v, and k respectively. (b) The covariance matrix for reflector C.

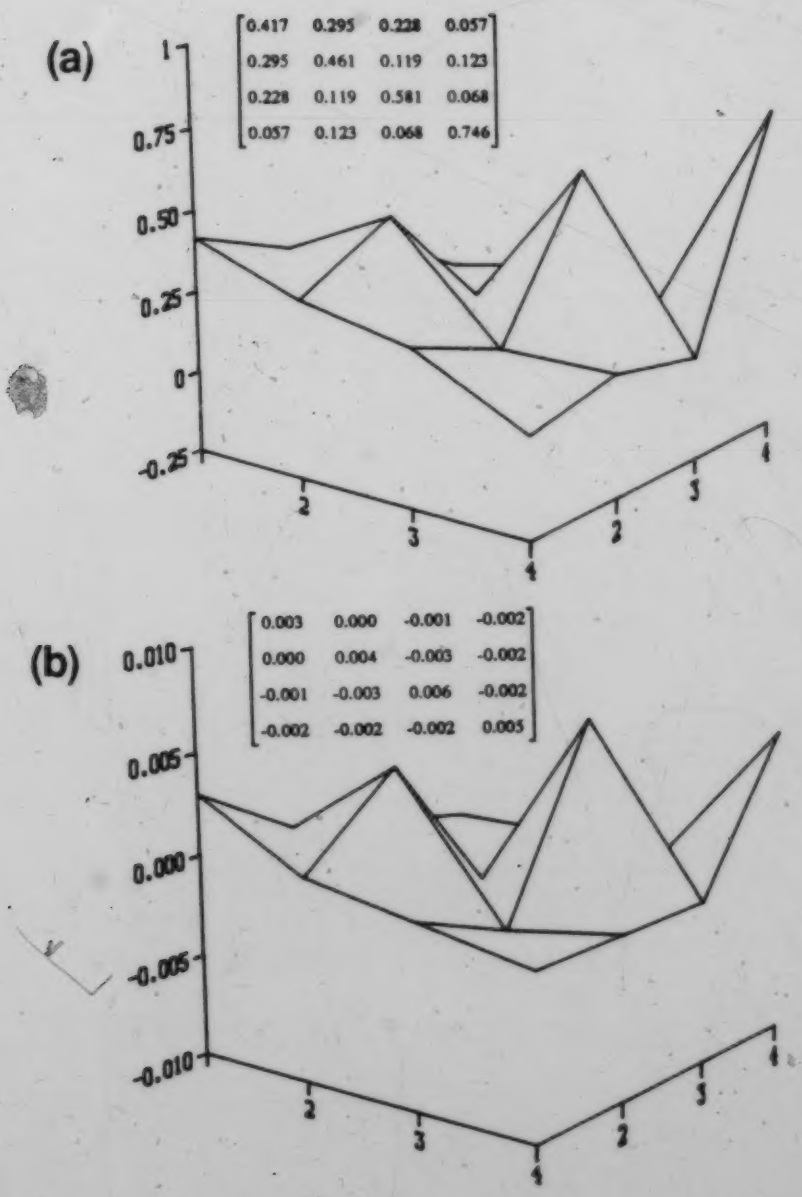

Figure 2.15 (a) The resolution matrix for reflector E. The order of the elements from 1 to 4 for the model parameters is a_0, a_{10}, a_{11}, and v respectively. (b) The covariance matrix for reflector E.

The CDP stack of seismic data is obtained by assuming that the reflectors are flat in the subsurface. If the reflectors are dipping then the CDP stack does not show the true position of the reflectors. In this case the true position is obtained by a process called migration. In order to determine the true location, the ray migration procedure makes use of the apparent dip of the reflector on CDP section (i.e. the change in reflection time between adjacent traces), the travel time and the derivative of the travel time with respect to the horizontal distance. The reflection times to reflectors C and E on all four lines were migrated by this simple ray migration technique. The contour plots for the depths of reflectors C and E, after ray migration, are illustrated in Figures 2.16 and 2.17 respectively. These figures show only the approximate estimates of the structures of these reflectors since they are generated by using data from four sparse lines and a linear interpolation in between. Generally speaking both the reflectors dip towards the northeast. The seismic velocities obtained from inversion were used in the ray migration algorithm.

Figure 2.17 also shows the boundary between Juan de Fuca plate and the America plate. At the boundary the depth to the subducting slab is approximately 6 km (Clowes et al. 1984). The 20 km depth contour is located at the edge of the Island. The depth contours between 6 km and 20 km are plotted by simple linear interpolation. Therefore the diagram in general shows that the subducting plate dips gently till the edge of the Island and then the dip becomes abruptly steeper. There is also a significant change in the strike under the southern portion of Vancouver Island. Riddihough (1977) estimated the rate and direction of convergence across the subduction zone from an analysis of offshore magnetic anomalies. The strike directions of the subducting plate shown in Figure 2.17 do not match well with his results. This can be explained from the fact that our results are based upon a sparse data set.

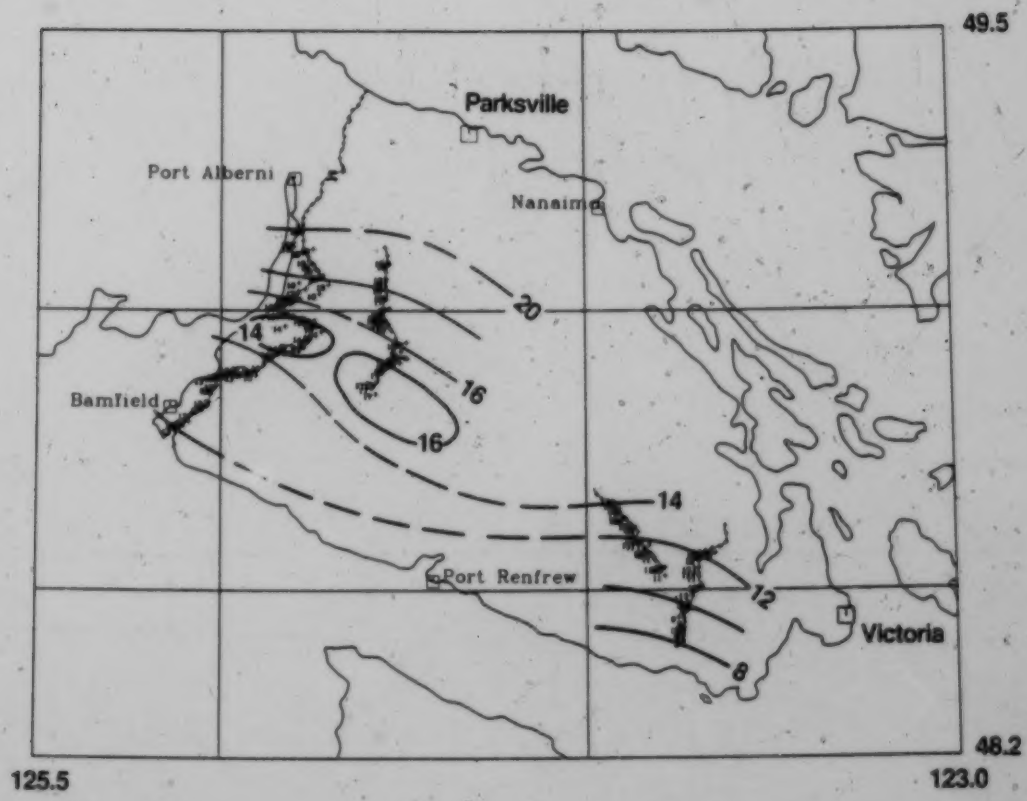

Figure 2.16 Structural map of the reflector C obtained by ray migration. The velocity obtained from inversion was used in the migration algorithm.

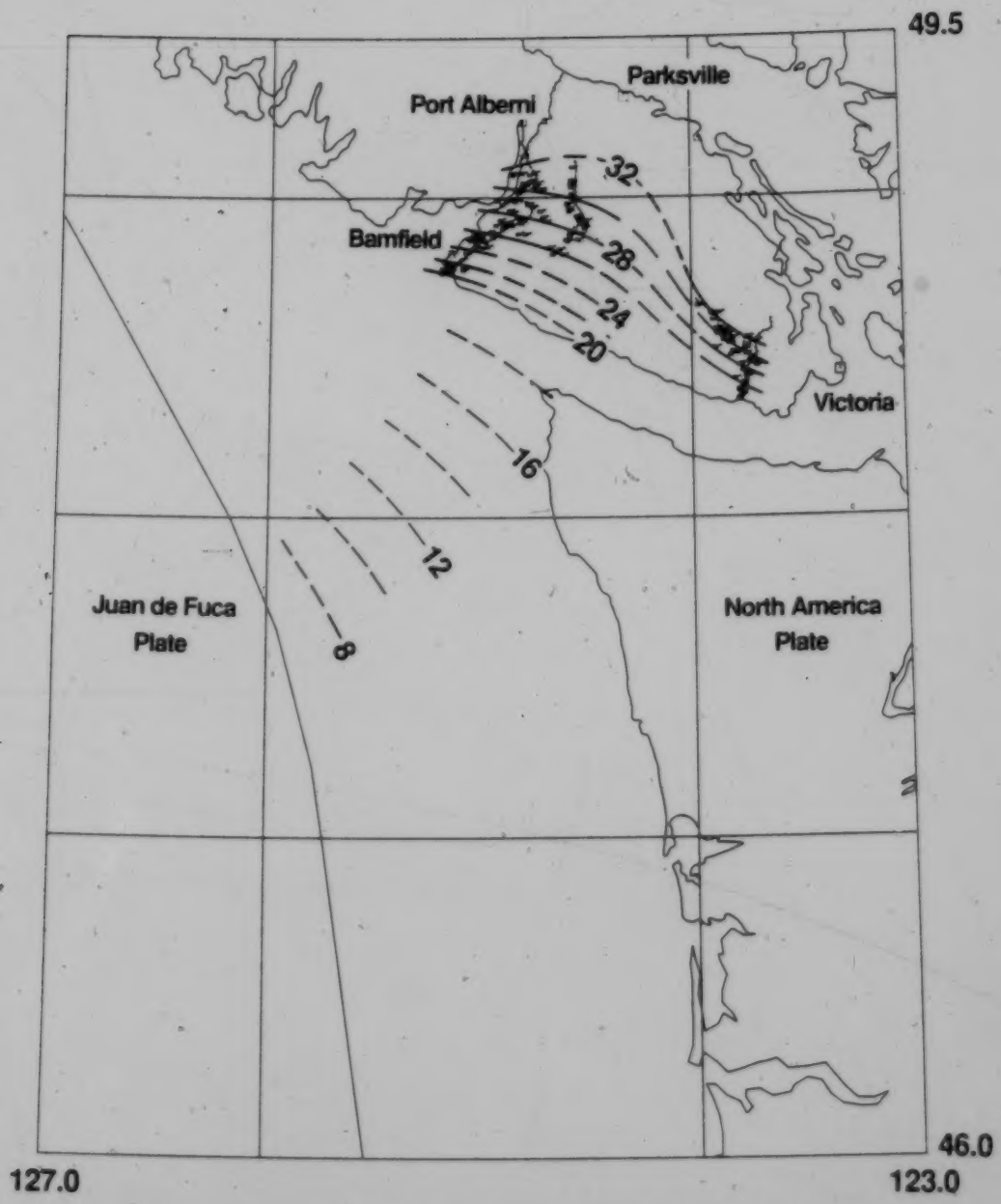

Figure 2.17 Structural map of the reflector E obtained by ray migration.

3.5 Conclusions

The method of tomographic inversion is shown to be fast and effective in obtaining a three-dimensional structure and the velocity gradients when travel time data is available from a wide range of source-receiver distances. For noise free synthetic data it was observed that the solution converges to the true model in a small number of iterations. However for data contaminated with noise, the rate of convergence is slower and the solution obtained only fits the data in a least squares sense. Noise also affects the stability of the solution and higher values for the damping factor are required. The method depends upon having field data with clearly distinguishable reflections, a condition that is met by only a limited number of reflecting horizons.

Good quality reflection data was acquired on Vancouver island allowing to image the subducting lithosphere and to understand the tectonics of this convergent margin. The reflection survey was carried out along a crooked road. We showed that a velocity model and a three dimensional structure of the subsurface can be obtained by taking advantage of the crookedness on the survey line. The velocity model obtained from inversion is consistent with refraction models. Also a fast and efficient algorithm was developed for forward modelling. As an example it takes about 4.5 sec of CPU time on Amdhal 5870 to trace 225 reflected rays from the third interface. With this algorithm rays can be generated for specified source receiver locations in three-dimensional media.

The advantage of this method is that one obtains an unbiased measure of the resolution and the precision for the parameters of the solution. Its disadvantage is that one must have some method of interpreting and timing the required travel times. The method has great potential if seismic surveys are planned to obtain three dimensional (tomographic) images and the source-receiver distances are made as large as possible. A distance range of 0 to 20 kms is suggested as practical for crustal studies. Even with distances of 0 to 10 km,

as in this study, the velocity determinations are comparable in accuracy to those obtained from refraction studies. The advantage of the reflection determined constants is that they are locally determined and not subjected to large distance averaging when using refraction - wide angle reflection seismic results.

CHAPTER 3

COMMON FAULT POINT (CFP) STACKING METHOD

3.1 Introduction

The presence of diffractions on seismic sections indicates discontinuities in the subsurface acoustic impedance. On a field common shot gather a subsurface diffractor gives rise to a hyperbolic pattern with a curvature dependent upon the velocity of the medium and an apex location close to the surface receiver directly above the discontinuity. In order to find the true location of the diffractor in space and time the trace containing the apex has to be shifted to its two-way vertical travel time equivalent, an amount dependent upon the positions of the shotpoint and receiver relative to the diffractor. The method was first discussed at the 1986 Annual meeting of the Canadian Society of Exploration Geophysicists (Kanasewich and Phadke, 1986).

In the case of both thrust and normal faulting, seismic records taken across faults generally show an overlapping of reflected energy from the two displaced fault blocks (Krey 1952; Kunz 1960). Diffraction of seismic waves causes this overlapping and this phenomenon can be used successfully in the interpretation of faults. Diffractions can also be produced by various other geological discontinuities (Haagedorn 1954), e.g. a pinchout, a wedgeout, a reef edge or any sudden change of facies. As a practical example they are also associated with seismic bright spots and flat spots (Stone 1974) which are caused by density and velocity changes due to the accumulation of gas in porous media. Therefore they are good indicators of structural and stratigraphic anomalies and can be of great importance in hydrocarbon prospecting. Thus processing techniques should be designed to enhance the detection of point diffractors, not to remove them by destructive interference.

A least-squares technique has been used by Schilt et al.(1981) to model diffracted signals observed on common midpoint sections. They assumed simple point or line models for the diffractors and determined their locations in space and time and the approximate root mean square velocity to these diffractors. Hubral (1975) obtained a direct solution to the problem of locating a point diffractor below plane layers of constant interval velocity and varying dip. The input data were the diffraction arrival times observed on stacked sections.

Recently Landa et al. (1987) have suggested a method for the detection of diffracted waves on common-offset sections. Their algorithm makes use of traveltime, amplitude and phase characteristics of the diffracted waves and identifies them by a correlation procedure. The values of a function, determined by averaging the seismic field along the diffracted traveltime curve and above a specified threshold, form the data for the D-section. The high amplitudes on this section are related to the location of diffractors. The method utilizes only common-offset traces, therefore the complete information regarding the diffracted field is not used. The method described here uses the complete information and is also analogous to a Common Mid Point (CMP) stacking method with diffracting rays migrated to their approximate subsurface origin.

This chapter describes a technique which takes into account the traveltime and amplitude characteristics of the diffracted signals and enhances the amplitude of the seismic signal at the location of the diffractors on a Common Fault Point (CFP) section analogous to the Common Depth Point (CDP) section used to enhance reflection data. A CDP section displays reflection data reduced to vertical incidence travel paths, whereas a CFP section displays diffraction arrivals at vertical incidence.

A CFP section shows not only diffractions from fault edges, but also those from other geological features with impedance discontinuities or large gradients in the impedance. For example, reefs, salt domes, intrusions, unconformities and discontinuity in fluid content will all produce diffraction patterns if there are lateral discontinuities in the

acoustic impedance.

The CFP stacking method assumes an acoustic model of the subsurface and the diffraction response of a discontinuous reflector is obtained by making use of Kirchoff's integral solution of the wave equation. A CFP trace is obtained by assuming the diffractor to be located beneath that surface location, applying the appropriate moveout and amplitude corrections to the selected field traces and then summing all of them (Figures 3.1 and 3.2). Figure 3.1 shows the traces from three shots for one CFP location. The receiver location for each shot, and the site where one expects the maximum diffraction amplitude due to a discontinuity beneath the indicated CFP location, are also shown. Since the diffraction amplitude drops very rapidly on either side of R_{max}, only a few traces on both sides of R_{max} are considered. The number of traces used depends upon the nature of the amplitude drop and is explained in the next section. Figure 3.2 illustrates a comparison between a CMP gather and a CFP gather. Figure 3.2a shows a 3 fold CMP gather. Figure 3.2b shows a CFP gather for the same shots, where all the traces shown in Figure 3.1 contribute to the gather and the summation of all these traces produces a CFP stacked trace with a 26 fold gather from 13 individual raypaths.

The following sections give a description of the amplitude and phase characteristics of diffracted waves for nonzero separation of source and receiver and then an explanation of the method of diffraction moveout correction, amplitude correction and stacking. The potential of the method is first demonstrated for synthetic data without noise. Then it is shown that the method gives good results even for the synthetic data with low signal to noise ratio. Finally the technique is applied to three real reflection data sets from southern Alberta and Melville Island (Northwest Territories). The results are quite promising.

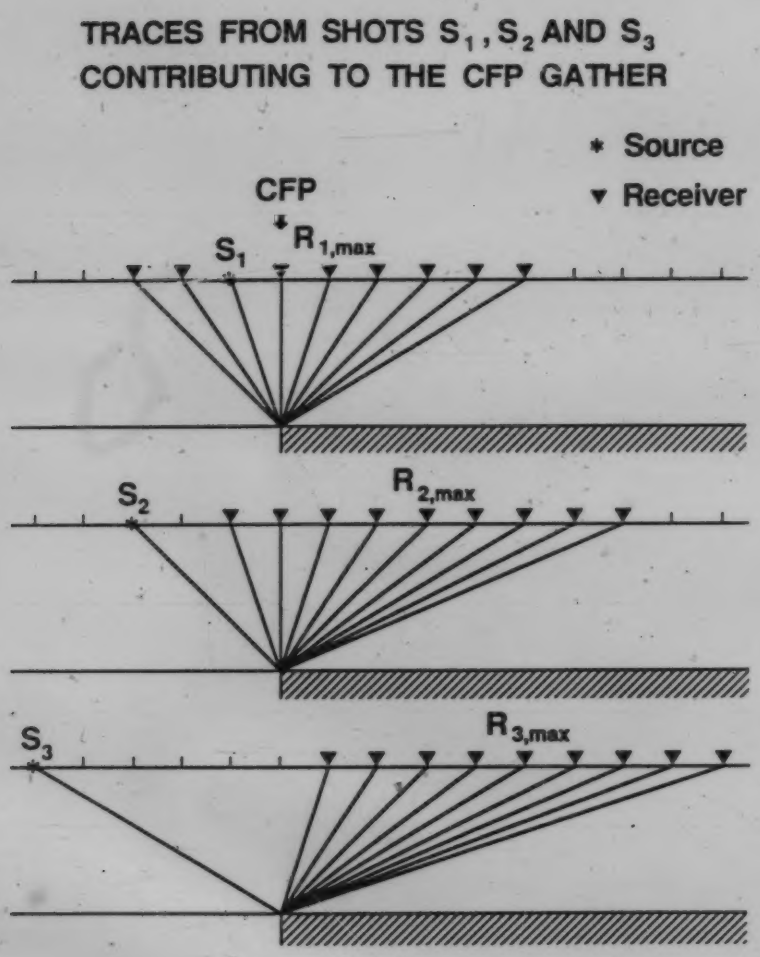

Figure 3.1 Receiver locations for three shots contributing to a CFP gather. S_1, S_2, and S_3 are the shot locations and $R_{1,max}$, $R_{2,max}$, and $R_{3,max}$ respectively are the receiver locations with maximum diffraction amplitude due to a discontinuity beneath the indicated CFP location. There are 26 ray paths that can contribute to a CFP gather.

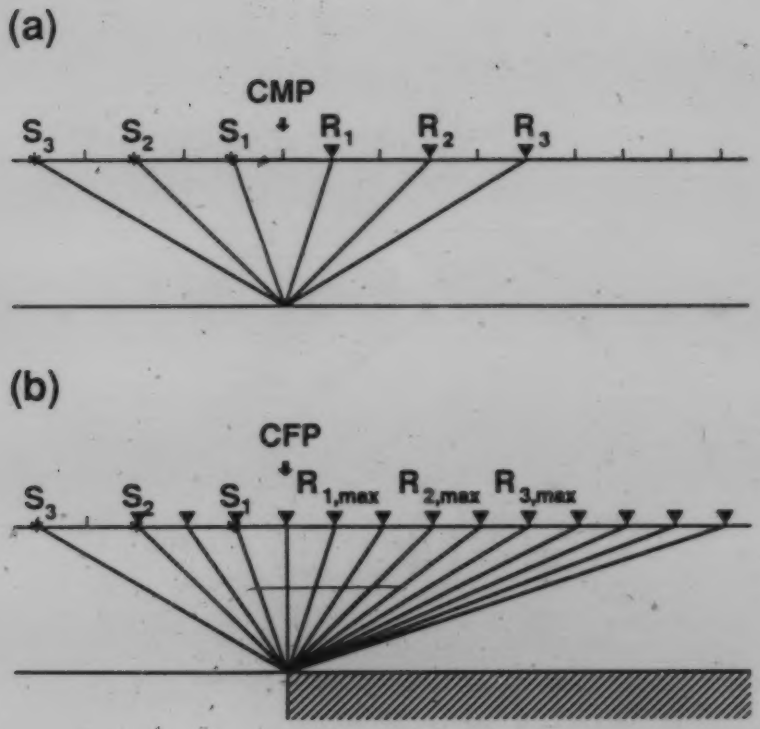

Figure 3.2 A comparison between a CMP gather and a CFP gather. (a) A 3 fold CMP gather. (b) A CFP gather for the same shots. All 26 traces shown in Figure 3.1 contribute to this gather from 13 individual raypaths.

3.2 Amplitude and phase characteristics of diffracted signals

Diffractions are produced by rays incident upon edges, corners or vertices of boundary surfaces or which graze such surfaces. Away from the diffracting surfaces, the seismic energy propagates like ordinary rays and the diffracted wavefronts obey the usual eikonal equation.

To determine the analytical response of a discontinuous reflector, one makes use of Huygen's principle, which states that every point on the reflector acts as a source of secondary disturbance. The response at a receiver is obtained by summing all the responses due to these secondary disturbances. This always poses an ambiguity as to what should be called reflected energy and what should be called diffracted energy. Dix(1952) defines the term 'reflection' to denote an event which gives information regarding curvature or dip of the interface, and the term 'diffraction' to include all other events, some of which may tell us about a discontinuity in the interface. Applying this definition to a truncated plane interface, we find that the reflected energy arriving at the receiver follows the least time path and all the energy received after this first arrival is the diffracted energy. For certain receiver locations both reflected and diffracted waves may arrive at the same time. To be consistent with the definitions proper amplitudes and phases are assigned to each on the basis of theoretical elastic wave model studies.

Several theoretical studies regarding diffraction response for coincident source-receiver location have been carried out in the past (Trorey 1970, Hilterman 1970, Hilterman 1975, Berryhill 1977), since an interpreter usually uses zero-offset sections. But the zero-offset section obtained by correcting common midpoint traces for normal moveout and stacking does not necessarily simulate true response for coincident source-receiver locations. Diffractions are usually suppressed by such stacking. Also since the diffractions from a subsurface diffractor are present on all shot receiver pairs, in principle one can

make use of all the traces to enhance amplitudes at diffracting points on seismic sections. For this purpose one needs to know the amplitude and phase characteristics of diffractions for nonzero separation of source and receiver.

Trorey(1977) and Berryhill(1977) derived closed form solutions for diffraction response for nonzero separation of source and receiver. In the following discussion Berryhill's formulation for diffraction response for the acoustic case due to a vertical fault is used.

Consider a plane truncated reflector as shown in Figure 3.3. The shot-receiver axis is perpendicular to the edge of the reflector. The origin is taken at the shot-receiver midpoint, with X-axis along the shot-receiver axis and Z-axis positive downwards. X_0 is the horizontal distance of the edge from the origin, Z_0 is the vertical distance of the edge from the origin, v is the velocity in the upper medium, 'a' is half of the shot-receiver separation, and t_a is the time of first arrival of the diffracted signal. For the purpose of testing the stacking algorithm, the assumption of an acoustic constant velocity medium is adequate. The diffraction response in this case for an arbitrary source receiver separation is given by (Berryhill 1977) (Appendix II)

$$D_a(t) = \frac{1}{\pi} \cos\theta_0 \left[\frac{R_0^2 v}{a^3} [\, C(t) + B(t)\, A(t)\, \Theta(t)\,] + \frac{R_0^2}{a^2} \frac{d}{dt} [\, A(t)\, \Theta(t)\,] \right] \tag{3.1}$$

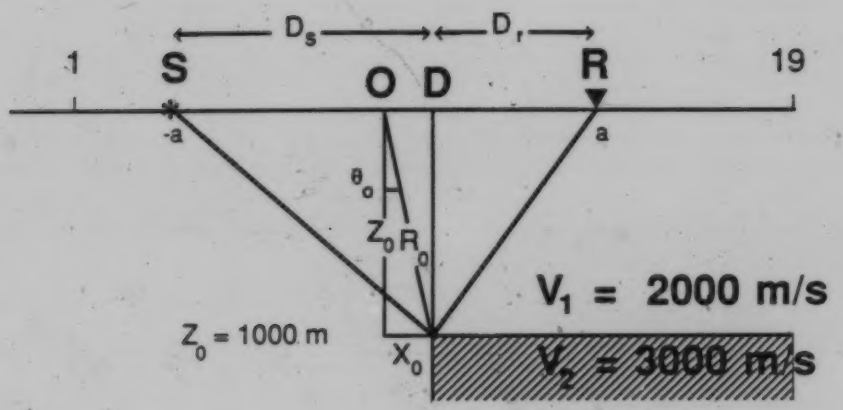

Figure 3.3 Geometry of a truncated plane reflector. The shot-receiver axis is perpendicular to the edge of the reflector. S and R are the positions of shot and receiver respectively, with shot-receiver midpoint as the origin. X_0 is the horizontal distance of the edge from the origin. Z_0 is the depth of the edge. Locations 1 to 19 are the surface locations with edge located beneath location 10.

where

$$A(t) = \frac{1}{\sinh u}\left[\cosh^2 u - \frac{x_0^2}{a^2 \cosh^2 u}\right]^{-1/2}$$

$$B(t) = \frac{\cosh u}{\cosh^2 u - K^2}$$

$$C(t) = \frac{[K^2 \cosh^2 u - x_0^2/a^2]^{1/2}}{\sinh u\ (\cosh^2 u - K^2)(\cosh^2 u - x_0/a)}$$

$$\Theta(t) = \arcsin\left[\frac{\cosh u}{K}\,\frac{(a K^2 - x_0)}{(a \cosh^2 u - x_0)}\right]$$

$$\cosh u = \frac{v t}{2 a}$$

$$K = \left[1 - \frac{Z_0^2}{a^2 \sinh^2 u}\right]^{1/2}$$

$$\cos \theta_0 = \frac{Z_0}{R_0}$$

and $\Theta(t_a) = -\pi/2$

The response at the receiver ($p_r(t)$) is obtained by convolving $D_a(t)$ with the source wavelet ($f(t)$), i.e.

$$p_r(t) = f(t) * D_a(t)\ U(t - t_a) \qquad (3.2)$$

where $U(t - t_a)$ is the unit step function used because the diffracted wave does not arrive

before $t=t_a$.

The diffraction response $D_a(t)$ for the model of Figure 3.3 is evaluated by the computer at discrete time points beginning at t_a, with the derivative term approximated by a difference. This response with the shotpoint at location 8 and receivers at locations 2 to 14, is shown in Figure 3.4a. The diffracting edge is at a depth of 1000 m and the velocity of the medium is 2000 m/s. The source pulse is approximated by an expression of the form $U(t-t_a)\, e^{-a(t-t_0)} \sin[\omega_0(t-t_0)]$ where t_0 is the ray arrival time. The distance between two adjacent receivers is 100 m. Geometrical spreading is not included. Figure 3.4b illustrates the diffraction response along with the reflection response. The important conclusions derived from these illustrations are listed in item form below.

(i) The diffraction time-distance curve is hyperbolic with maximum amplitude at a receiver location for which the diffracting edge is vertically below the source-receiver midpoint.

(ii) The algebraic sign of the diffraction amplitude depends upon the location of the shot-receiver midpoint. If the midpoint lies above the reflector, then the sign is opposite to that of the reflection amplitude from the edge, and if the midpoint is not above the reflector or the edge, then the sign is the same as that of the reflection amplitude from the edge.

(iii) The highest amplitude on the diffraction hyperbola is half of the reflection amplitude from the edge, and does not always occur at the apex of the travel-time hyperbola. The apex is seen at the receiver vertically above the edge, whereas the highest amplitude is seen when the shot-receiver midpoint is vertically above the diffracting edge. The amplitude decreases very rapidly as the shot-receiver midpoint moves away from the point vertically above the edge.

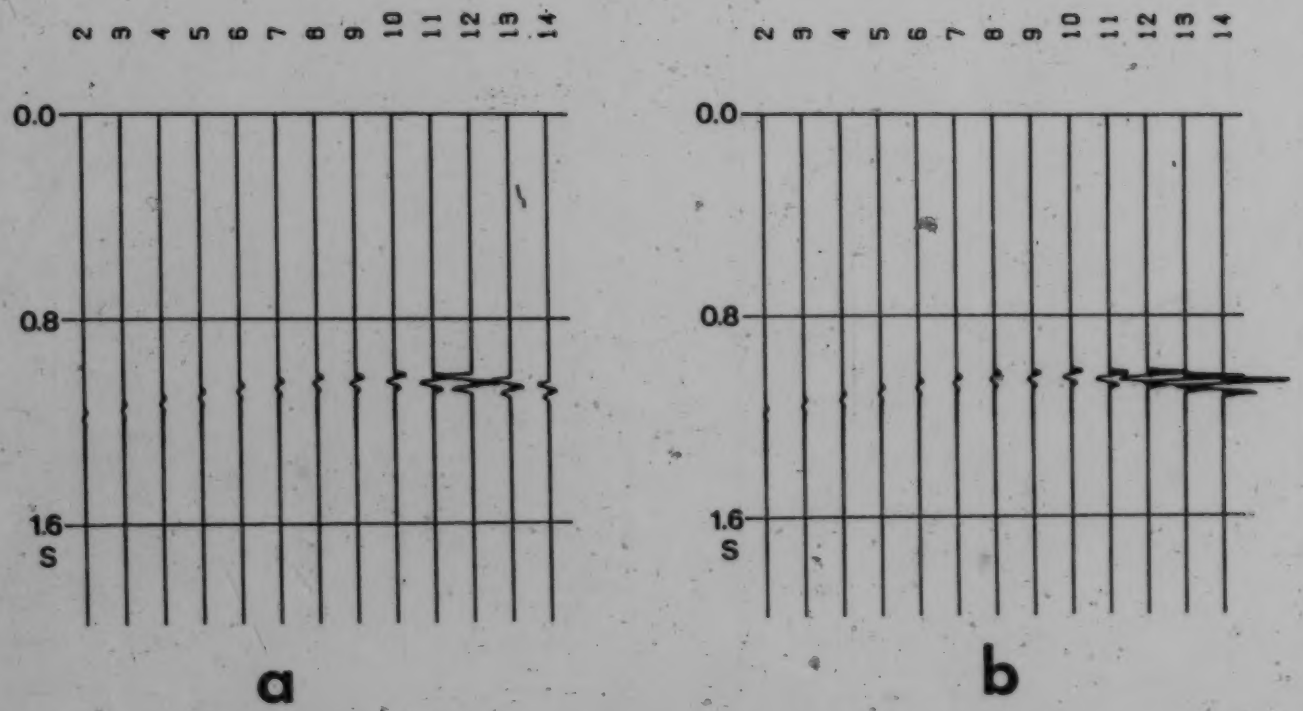

Figure 3.4 (a) The diffraction response and (b) the combined reflection and diffraction response for the model of Figure 3.3. Shot point is at location 8 and the diffracting edge is below location 10.

The graph of the ratio (R) of diffraction amplitude to reflection amplitude from the edge versus the position of the shot-receiver midpoint (X_0) is shown in Figure 3.5 for various depths of the diffracting edge. The amplitude drop is much more rapid for shallow diffractors as compared to that for the deep diffractors. Therefore when making amplitude correction to moveout corrected seismic data, the amplitude characteristics required for diffractors at different depths will need to be considered. This will be explained in detail in the next section.

If the diffracting edge is parallel to the seismic line, then it is not possible to see a hyperbolic diffraction pattern on seismic section. Moreover on a CDP section the fault edge will show up as a reflector of small amplitude. The two-way time of this reflector depends upon the horizontal separation and depth of the edge with respect to the line. The diffraction response for a diffracting edge parallel to the shot receiver axis was also derived by Berryhill (1977). However, for the present investigation we have assumed that the diffracting edge is perpendicular to the shot receiver axis, since the seismic lines are usually planned to be perpendicular to the geological strikes of faults in the area under investigation. For a fault edge crossing a seismic line at an oblique angle the characteristic velocity of the diffraction pattern appears higher.

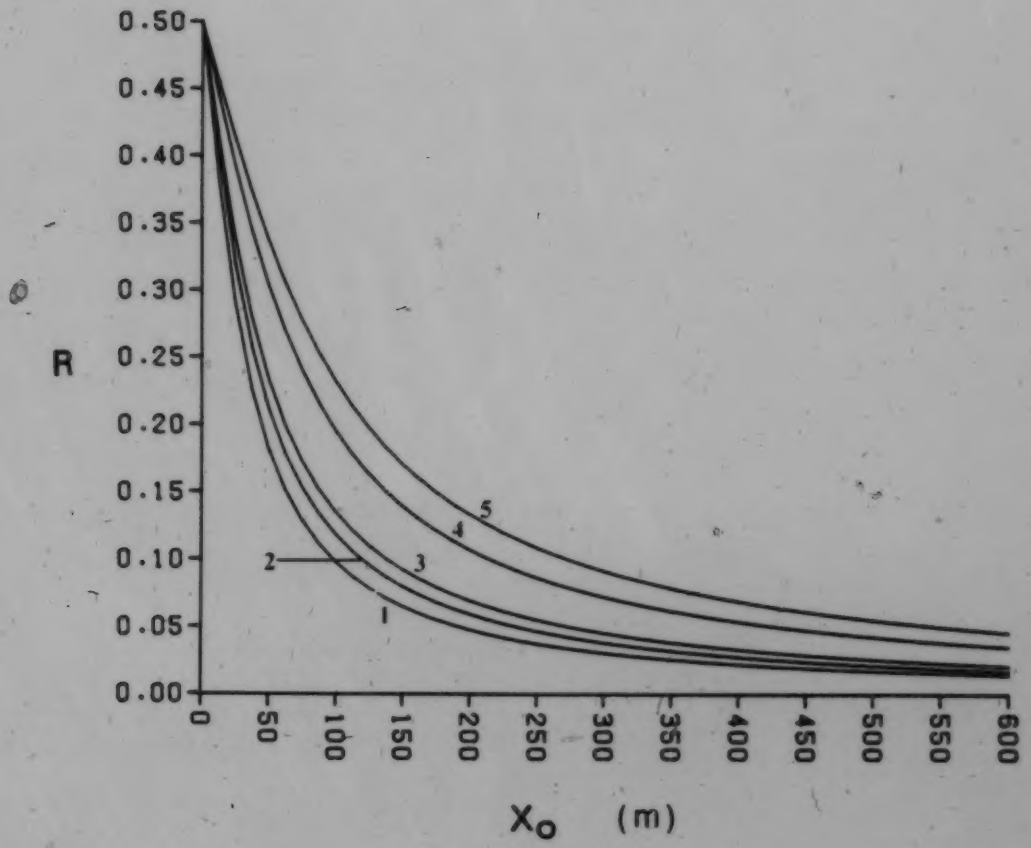

Figure 3.5 The graph of the ratio (R) of diffraction amplitude to reflection amplitude versus the position of the shot-receiver midpoint (X_0), for various depths of the diffracting edge (Z_0). 1. Z_0=500 m, 2. Z_0=750 m, 3. Z_0=1000 m 4. Z_0=2000 m, 5. Z_0=3000 m.

3.3 Method of diffraction moveout correction and stacking

Consider the geometry of Figure 3.3. S is the position of shot, R is the position of receiver, z_0 is the depth of the diffractor and v is the velocity in the upper medium. D_s and D_r are the projected horizontal distances of shot and receiver from the diffractor respectively. T_0 is the vertical travel time for a diffracted wave, if the shot and receiver were located vertically above the diffracting edge i.e. at 'D'. Then the travel time for a diffracted ray from shot to receiver is given by

$$T = \frac{[D_s^2 + z_0^2]^{1/2}}{v} + \frac{[D_r^2 + z_0^2]^{1/2}}{v} \qquad (3.3)$$

but

$$T_0 = \frac{2 z_0}{v}$$

Therefore

$$T = \left[\frac{D_s^2}{v^2} + \frac{T_0^2}{4}\right]^{1/2} + \left[\frac{D_r^2}{v^2} + \frac{T_0^2}{4}\right]^{1/2} \qquad (3.4)$$

If the fault edge is located below 'n-1' horizontal layers (Figure 3.6), then the traveltime for a diffracted ray from shot to receiver is given by

$$T = \sum_{k=1}^{2} T_k \qquad (3.5)$$

$$T_1 = \sum_{h=1}^{n} \frac{Z_h}{v_h (1 - v_h^2 p_1^2)^{1/2}} \qquad (3.6)$$

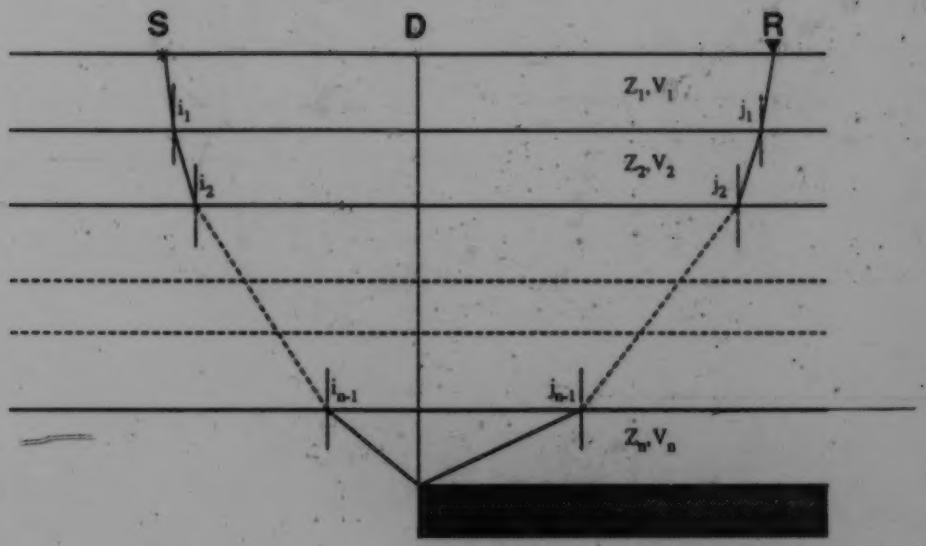

Figure 3.6. Geometry for the diffracted raypath when the diffracting edge is located below 'n-1' horizontal layers. 'i_1, i_2, ..., i_n' are the angles made by the downgoing ray with the vertical and 'j_1, j_2, ..., j_n' are the angles made by the upgoing ray with the vertical.

$$T_2 = \sum_{h=1}^{n} \frac{Z_h}{v_h (1 - v_h^2 p_2^2)^{1/2}} \tag{3.7}$$

where T_1 and T_2 are the travel times of the downgoing and upgoing rays respectively, and V_h and Z_h are the velocity and thickness of the h^{th} layer. The ray parameters p_k (k=1 or 2) of the downgoing and upgoing rays respectively are

$$\frac{\sin i_h}{v_h} = p_1 \quad ; \quad \frac{\sin j_h}{v_h} = p_2 \tag{3.8}$$

where i_h and j_h are the angles made by the downgoing and upgoing rays with the vertical in the h^{th} layer.

The horizontal distances D_s and D_r are given by

$$D_s = p_1 \sum_{h=1}^{n} \frac{Z_h V_h}{(1 - v_h^2 p_1^2)^{1/2}} \tag{3.9}$$

$$D_r = p_2 \sum_{h=1}^{n} \frac{Z_h V_h}{(1 - v_h^2 p_2^2)^{1/2}} \tag{3.10}$$

If one could eliminate p_1 and p_2 from equations (3.5), (3.6), (3.7), (3.9) and (3.10), then T could be expressed in terms of D_s and D_r only. From the nature of these equations it is not possible to do so analytically. But we can express T_1 in terms of D_s by expanding $T_1(D_s)$ by Taylor series expansion about D_s=0, and dropping the higher order terms

$$T_1(D_s) = T_1(0) + \left.\frac{dT_1}{dD_s}\right|_{D_s=0} D_s + \frac{1}{2!} \left.\frac{d^2T_1}{dD_s^2}\right|_{D_s=0} D_s^2 \tag{3.11}$$

The derivatives of T_1 with respect to D_s are obtained from (3.6) and (3.9) using the chain rule

$$\left.\frac{dT_1}{dD_s}\right|_{D_s=0} = \left.\frac{dT_1/dp_1}{dD_s/dp_1}\right|_{p_1=0} \tag{3.12}$$

$$\left.\frac{d^2T_1}{dD_s^2}\right|_{D_s=0} = \left.\frac{\frac{d}{dp_1}\left[\frac{dT_1}{dD_s}\right]}{(dD_s/dp_1)}\right|_{p_1=0} \tag{3.13}$$

The first derivative obtained using (3.12) is zero, whereas the second derivative is given by

$$\left.\frac{d^2T_1}{dD_s^2}\right|_{D_s=0} = \frac{1}{\sum_{h=1}^{n} Z_h v_h} \tag{3.14}$$

Substituting (3.14) in (3.11) gives

$$T_1(D_s) = T_1(0) + \frac{1}{2}\frac{D_s^2}{\sum_{h=1}^{n} Z_h v_h} \tag{3.15}$$

Squaring and truncating the terms beyond the quadratic term in D_s gives

$$T_1^2(D_s) = T_1^2(0) + \frac{D_s^2}{(\sum_{h=1}^{n} Z_h v_h)/T_1(0)} \tag{3.16}$$

Writing $T_1(0)$ in terms of the two-way vertical travel time i.e. when the shot and receiver are at D, we get

$$T_1(0) = \frac{T_0}{2} = \sum_{h=1}^{n} \frac{Z_h}{v_h} = \sum_{h=1}^{n} t_h \tag{3.17}$$

Substituting (3.17) in (3.16) gives

$$T_1^2(D_s) = \frac{T_0^2}{4} + \frac{D_s^2}{v_{rms}^2} \qquad (3.18)$$

where v_{rms} is the root-mean-square velocity.

$$v_{rms} = \sqrt{\frac{\sum_{h=1}^{n} v_h^2 t_h}{\sum_{h=1}^{n} t_h}} \qquad (3.19)$$

Similarly using (3.7) and (3.10) T_2 can be expressed in terms of D_r as

$$T_2^2(D_r) = \frac{T_0^2}{4} + \frac{D_r^2}{v_{rms}^2} \qquad (3.20)$$

Substituting T_1 and T_2 from (3.18) and (3.20) in (3.5), we obtain finally

$$T = \left[\frac{T_0^2}{4} + \frac{D_s^2}{v_{rms}^2}\right]^{1/2} + \left[\frac{T_0^2}{4} + \frac{D_r^2}{v_{rms}^2}\right]^{1/2} \qquad (3.21)$$

The above expression is similar to (3.4) except for the difference in velocity. Thus the effective velocity for a buried diffractor is equal to the root mean square velocity. This is analogous to the equation for normal moveout correction.

Mathematically the moveout correction amounts to shifting the trace by an amount equal to the traveltime difference between $D_S=0$, $D_r=0$ and the actual D_S and D_r. Since the velocity is a function of depth, the moveout correction is not a simple time shift applied to each trace but rather a function of time as follows:

$$\Delta t = T(j) - T_0(j)$$

$$= \left[\frac{D_s^2}{v_{rms}^2(j)} + \frac{T_0^2(j)}{4} \right]^{1/2} + \left[\frac{D_r^2}{v_{rms}^2(j)} + \frac{T_0^2(j)}{4} \right]^{1/2} - T_0(j) \qquad (3.22)$$

If $T_0(j)$ and $v_{rms}(j)$ are known for each reflector then the time shift Δt can be calculated for each value of 'j' and applied in a continuously time-varying fashion by some sort of interpolation scheme. In general Δt decreases with increasing T_0.

The moveout curve for a fixed shot position, vertical two-way time T_0=1.0 sec and v_{rms}=2000 m/s, is shown in Figure 3.7. The X-axis represents the horizontal distance of the receiver from the diffracting edge (D_r). The horizontal distance between the shotpoint and the diffractor is 200 m. The moveout correction to be applied for each value of D_r is equal to the time difference between the solid line and the dotted line for that value of D_r. If the corrections are applied to each trace, the diffractor will appear at its proper two-way travel time on all the traces. If appropriate amplitude corrections are also applied and all the traces are summed (stacked), the amplitude at the diffractor location will be enhanced because all the signals will be in phase.

If the alignment after the diffraction moveout correction is perfect, the signal amplitude level after the stack will be N times the level before stack, N being the number of traces summed. But each trace contributing to the sum has a noise component present in it. If we assume that the noise components of the traces are statistically independent and the noise variance is approximately the same for each trace, then the variance of the sum will be approximately N times the variance of the input noise level. Therefore the gain in signal amplitude to noise level by stacking is approximately equal to the square root of N, and this is the maximum which one can achieve. Normally the gain in signal to noise ratio is less than this.

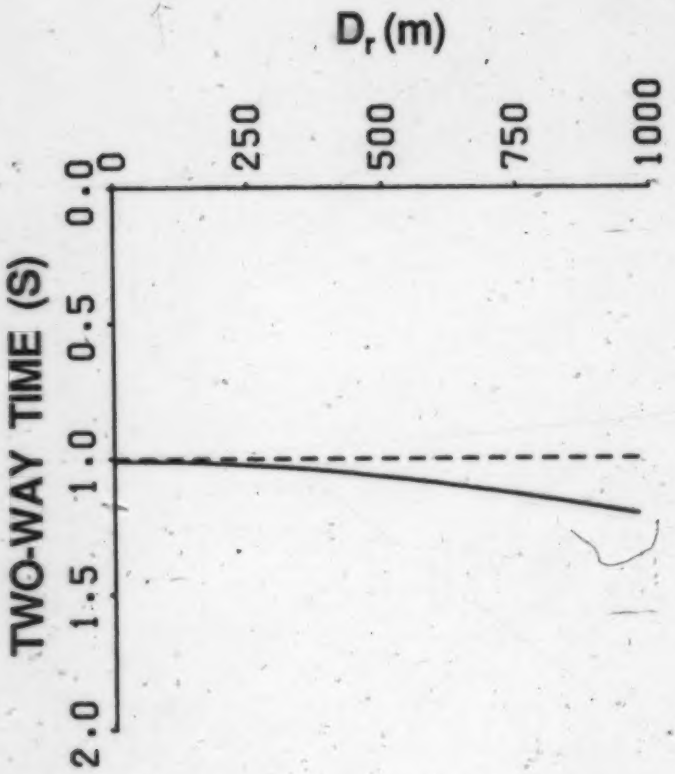

Figure 3.7 The time distance curve of a diffracted ray for a fixed shot position, two-way time T_0=1.0 sec., and V_{rms}=2000 m/s. The horizontal distance between the shotpoint and the diffractor is 200 m. The moveout correction for each value of D_r is equal to the time difference between the solid line and the dotted line for that value of D_r.

In the above discussion the surface location right above the diffractor was known. In general one does not know this surface location. In this case we have to try all possible locations on an arbitrary discrete grid in the x-z space. Assuming that the diffractors are located beneath the various surface locations, the time and amplitude corrections are applied to the selected pre-stack traces and the sum of these traces is represented at the surface location beneath which the diffractor was assumed to be located. This procedure is carried out for every surface location and the seismic section so obtained is called the CFP stack (Figures 3.1 and 3.2). The signals will be in phase only for the surface locations and two-way travel times where diffractors exist. Everywhere else they will be out of phase. Hence on such a stacked section one can find diffracting points and also discontinuities in the reflecting horizon.

3.4 Amplitude correction

Consider Figure 3.5 which shows the graph of the ratio (R) of diffraction amplitude to reflection amplitude versus the horizontal distance of shot-receiver midpoint from the edge (X_0) for different depths (Z_0) of the edge. From this data we can plot the graph of R versus Z_0 for different X_0's (Figure 3.8a). The graph of R versus two-way vertical travel time for different X_0's is also shown in Figure 3.8b. Two-way vertical travel times were calculated from depth and velocity information. This illustration clearly shows that for any X_0, R increases as the two-way vertical travel time increases.

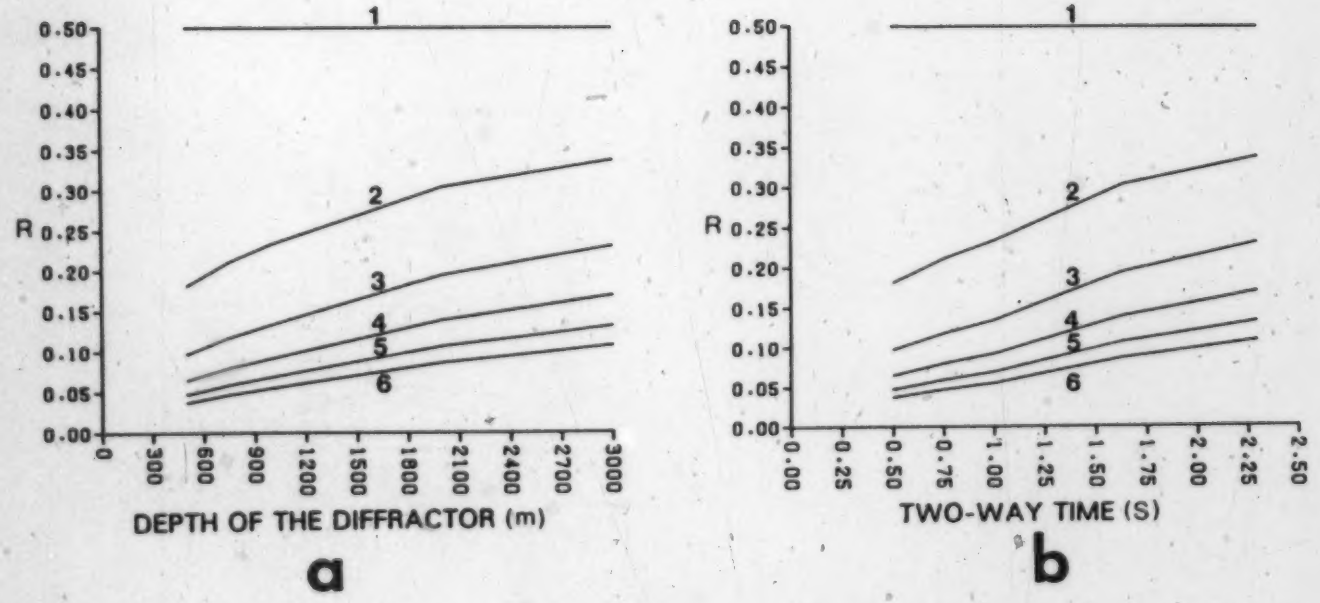

Figure 3.8. Plots of R as a function of (a) depth (Z_0) and (b) two-way vertical travel time (T_0), for various values of X_0. 1. X_0=0.0, 2. X_0=50.0, 3. X_0=100.0, 4. X_0=150.0, 5. X_0=200.0, 6. X_0=250.0.

To make all the diffraction amplitudes equal to the reflected amplitude from the edge (or maximum diffraction amplitude), we need to multiply them with the inverse of R. Figure 3.9 illustrates the inverse of R plotted as a function of two-way time. Also since there is a phase reversal, as the shot-receiver midpoint moves from one side of the fault to the other, a phase correction must be incorporated in the data after making moveout correction. This is important, since otherwise the signals will not be in phase at the time of stacking. Therefore to obtain a trace corresponding to a surface location on CFP section, we first assume that the diffractors are located beneath that surface location. Then we apply the diffraction moveout correction to all the traces and multiply each trace by the amplitude correction time function corresponding to the value of X_0. Finally all the traces are stacked to form a single trace. This is done for each surface location to obtain the CFP section.

3.5 Synthetic tests

One synthetic model example is included here to demonstrate how the method works in practice. Synthetic records for the model of Figure 3.3 are obtained for shot locations 1 to 19. Six traces on either side of the shot are generated for each shot location. Only diffracted waves and reflected waves are taken into consideration. Geometrical spreading is not taken into account. P-wave velocities in media I and II are 2000 m/s and 3000 m/s respectively.

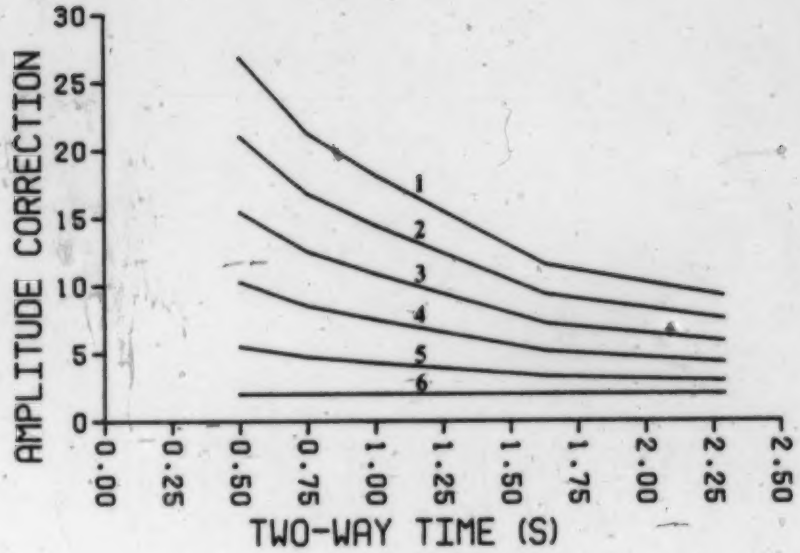

Figure 3.9 The amplitude correction function (1/R) plotted as a function of two-way time for various values of X_0. 1. X_0=250.0, 2. X_0=200.0, 3. X_0=150.0, 4. X_0=100.0, 5. X_0=50.0, 6. X_0=0.0.

The method is tested for synthetic data without and with added noise. Examples of the synthetic records with added noise are shown in Figures 3.10a and 3.10b, which exhibit a very low signal to noise ratio. The reflected energy can still be seen but the diffractions are not visible. Figures 3.10c and 3.10d show the NMO stacks of the 19 synthetic records. Only midpoint locations from 4 to 16 are used for this purpose. On the NMO stack of the synthetic data without noise (Figure 3.10c), the reflector as well as the diffractions beyond the edge of the reflector can be clearly seen. On the NMO stack of the synthetic data with added noise (Figure 3.10d), the reflector can still be seen but the diffractions are completely masked. Therefore it is difficult to determine the place of termination of the reflector.

The CFP stacking method is now applied to determine the discontinuity in the reflecting horizon. Since the amplitude on the diffracted signal falls very rapidly as the shot-receiver midpoint is moved away from the point vertically above the edge, only those receiver locations for which the shot-receiver midpoint is within 400 m of the point vertically above the edge are considered for CFP stacking purposes. Beyond 400 m the diffraction amplitudes are very low and hence the diffracted signal will be totally distorted. The choice of the threshold distance is an empirical arbitrary parameter, based on a plot like Figure 3.5.

CFP stacks of the synthetic data, (including moveout but not amplitude corrections to diffractions) without and with added noise are shown in Figures 3.11a and 3.11b respectively. The amplitude enhancement at the location of the diffractor is not very high in this case. Figures 3.11c and 3.11d show the CFP stacks, without and with added noise, when amplitude corrections were also performed. Both CFP stacks show considerable enhancement in signal amplitude at the reflector edge. This shows that the method works even for noisy data with a low signal to noise ratio.

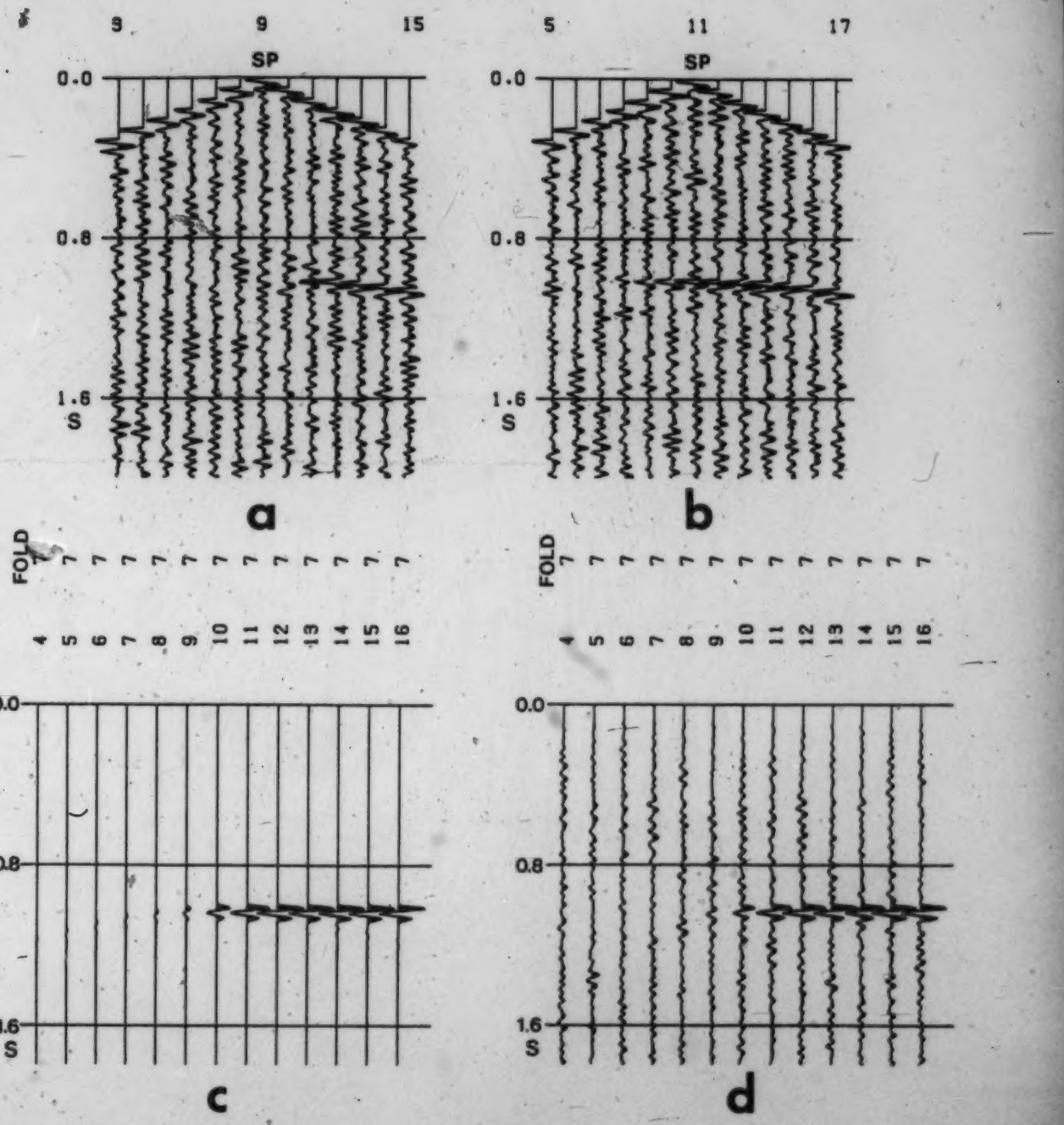
9
9
15
SP
0.0
0.8
1.6
S
a
5
11
17
SP
0.0
0.8
1.6
S
b
FOLD
7 7 7 7 7 7 7 7 7 7 7 7 7
4 5 6 7 8 9 10 11 12 13 14 15 16
FOLD
7 7 7 7 7 7 7 7 7 7 7 7 7
4 5 6 7 8 9 10 11 12 13 14 15 16
0.0
0.8
1.6
S
c
0.0
0.8
1.6
S
d

Figure 3.11 (a) and (b) are the CFP stacks of synthetic records without and with added noise respectively. Amplitude correction is not applied after correcting for moveout. (c) and (d) are the CFP stacks of synthetic records without and with added noise respectively. Amplitude correction is applied here after correcting for moveout.

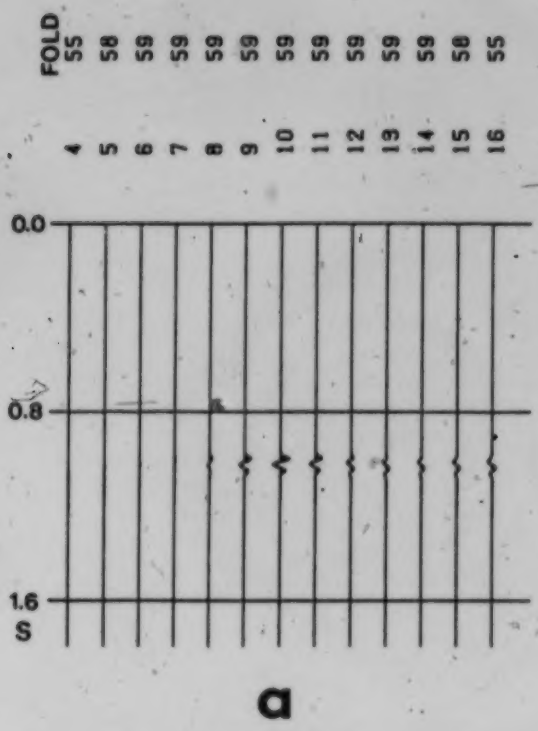
FOLD
55 58 59 59 59 59 59 59 59 59 59 58 55
4 5 6 7 8 9 10 11 12 13 14 15 16
0.0
0.8
1.6
S

a

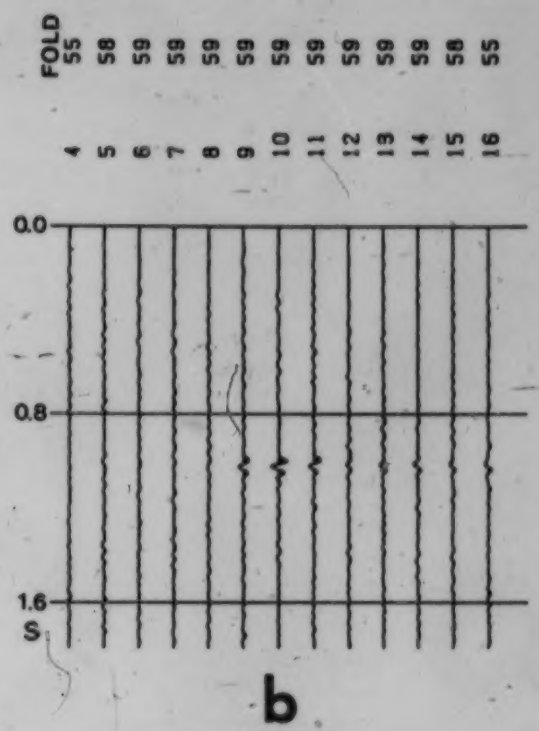
FOLD
55 58 59 59 59 59 59 59 59 59 59 58 55
4 5 6 7 8 9 10 11 12 13 14 15 16
0.0
0.8
1.6
S

b

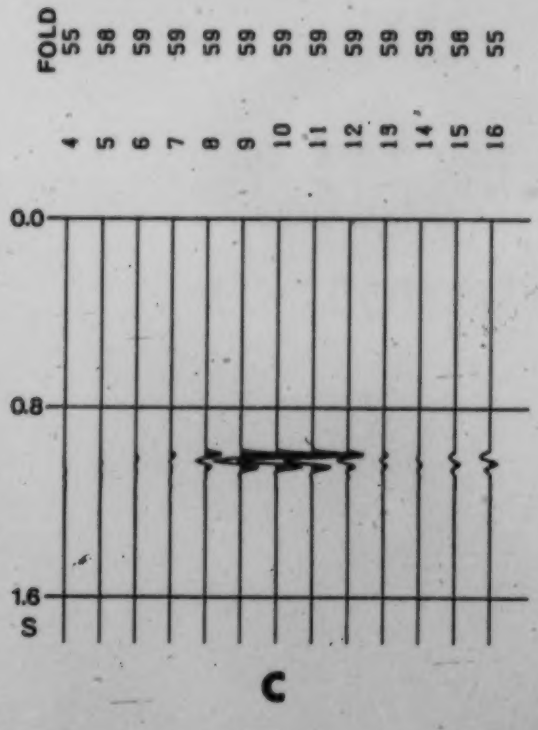
FOLD
55 58 59 59 59 59 59 59 59 59 59 58 55
4 5 6 7 8 9 10 11 12 13 14 15 16
0.0
0.8
1.6
S

c

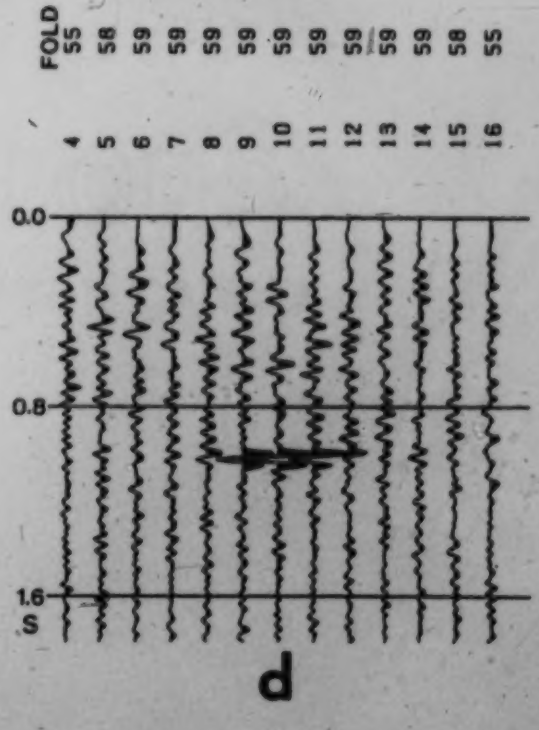
FOLD
55 58 59 59 59 59 59 59 59 59 59 58 55
4 5 6 7 8 9 10 11 12 13 14 15 16
0.0
0.8
1.6
S

d

One other difference between an NMO stack and a CFP stack is in the number of traces used to produce a single trace on these sections. Since a trace on CFP section is obtained by summing a large number of traces, the fold is very high. For the synthetic data considered here the highest fold on an NMO stack is 7, whereas on a CFP section it is 59.

From the above discussion it can be inferred that if the NMO stack does not show the location where a reflector is terminated then a CFP stack can be used to determine this location.

3.6 Application to real data

3.6.1 Reflection, gravity and magnetic survey in southern Alberta

Pancanadian Petroleum Limited carried out a Vibroseis survey in the Vulcan area (Southern Alberta) during November 1983. This survey method is established as an excellent tool for crustal studies (Fowler and Waters 1975, Schilt et.al. 1979, Oliver et.al. 1983). The data for line 83-421 was made available to us for scientific crustal investigations. Figure 3.12 shows the location map of the line, which is approximately 33 kms in length and is situated 4 kms east of Vulcan. It traverses North-South and cuts across a postulated Precambrian rift valley, which lies below the flat lying sediments (Kanasewich, 1968). The seismic instrumentation consisted of a 96-channel Texas Instruments DFS-V recording system employing four synchronized vibrator sources. The receivers were 8 Hz Mark Product geophones with 9 units per channel. An inline split-spread shooting pattern with spread over approximately 10 kms was used along with a shot point interval of 200 m and receiver group interval of 100 m. The source array was generated by moving four Vibroseis units thirty-two times to produce a single field record stack. An upsweep of 5 to 35 Hz over a 30 sec duration was used and the seismic data were recorded for 50 sec at 4 ms interval.

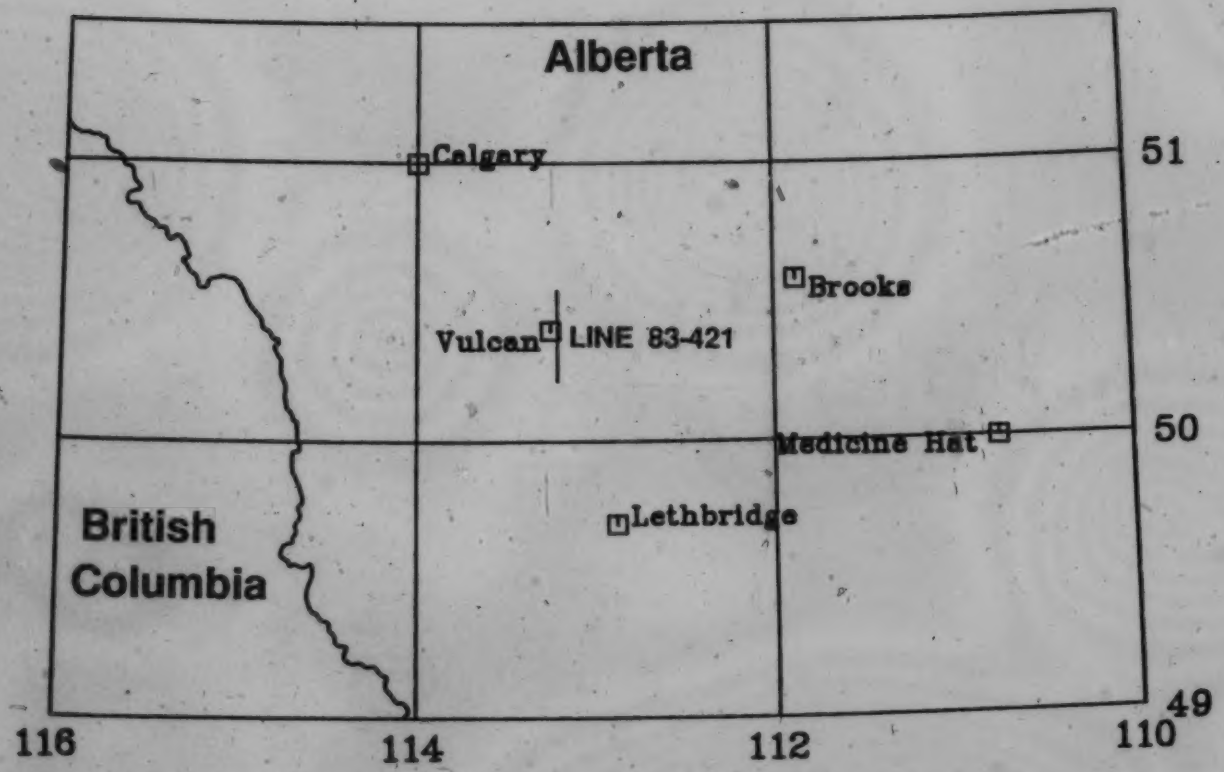

Figure 3.12 Location map of the Vibroseis line in Vulcan area of Southern Alberta.

Previous reflection research carried out in southern Alberta (Kanasewich & Cumming, 1965; Clowes et. al.,1967; Kanasewich, 1968) indicates several continuous deep reflecting horizons except for zones of fracturing and faulting. A prominent mid-crustal reflector, called the Riel discontinuity was also reported. At this reflector the velocity increases abruptly from 6.5 to 7.2 km/sec. Dips of up to 20 deg. necessitated migration. The results from Kanasewich (1968) are shown in Figure 3.13. Weak reflections were observed from the Mohorovicic discontinuity. Figure 3.13 also shows that the Moho changes in depth from 38 to 47 km while the Riel discontinuity changes in depth from 26 to 37 km. The anomalous magnetic and gravity trends show that the rift is continuous across Alberta and British Columbia.

The Bouguer gravity and aeromagnetic anomalies along the new seismic line 83-421 are shown in Figure 3.14a and 3.14b. The gravity anomaly also suggests the presence of buried low density section in the area under investigation.

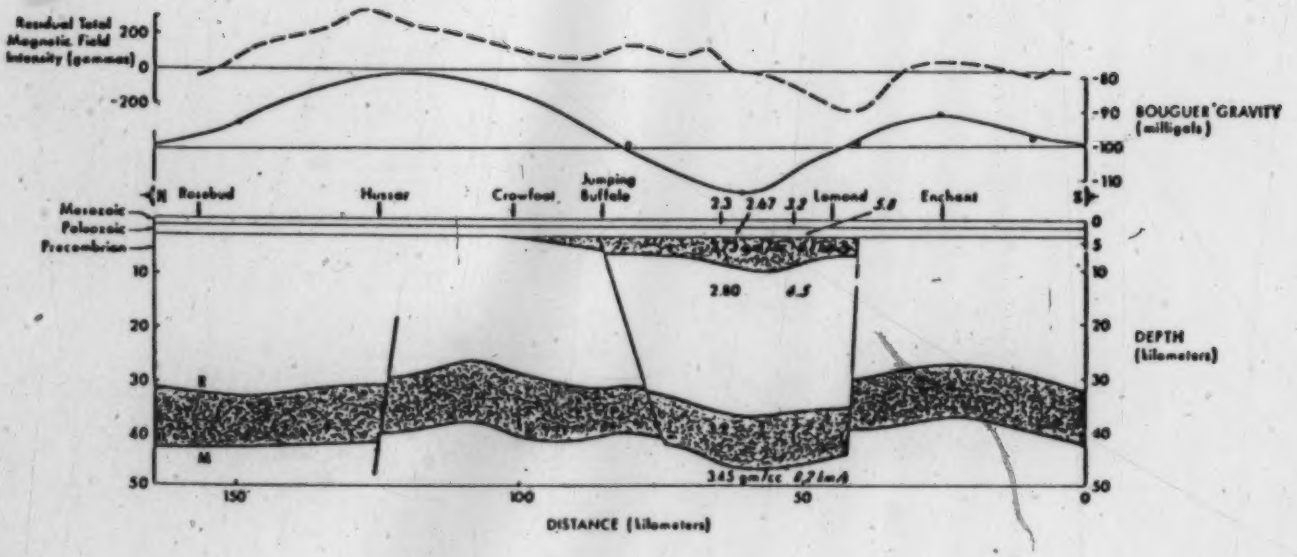

Figure 3.13 Seismic Reflection cross-section across southern Alberta (Reproduced from Kånasewich, 1968 with permission).

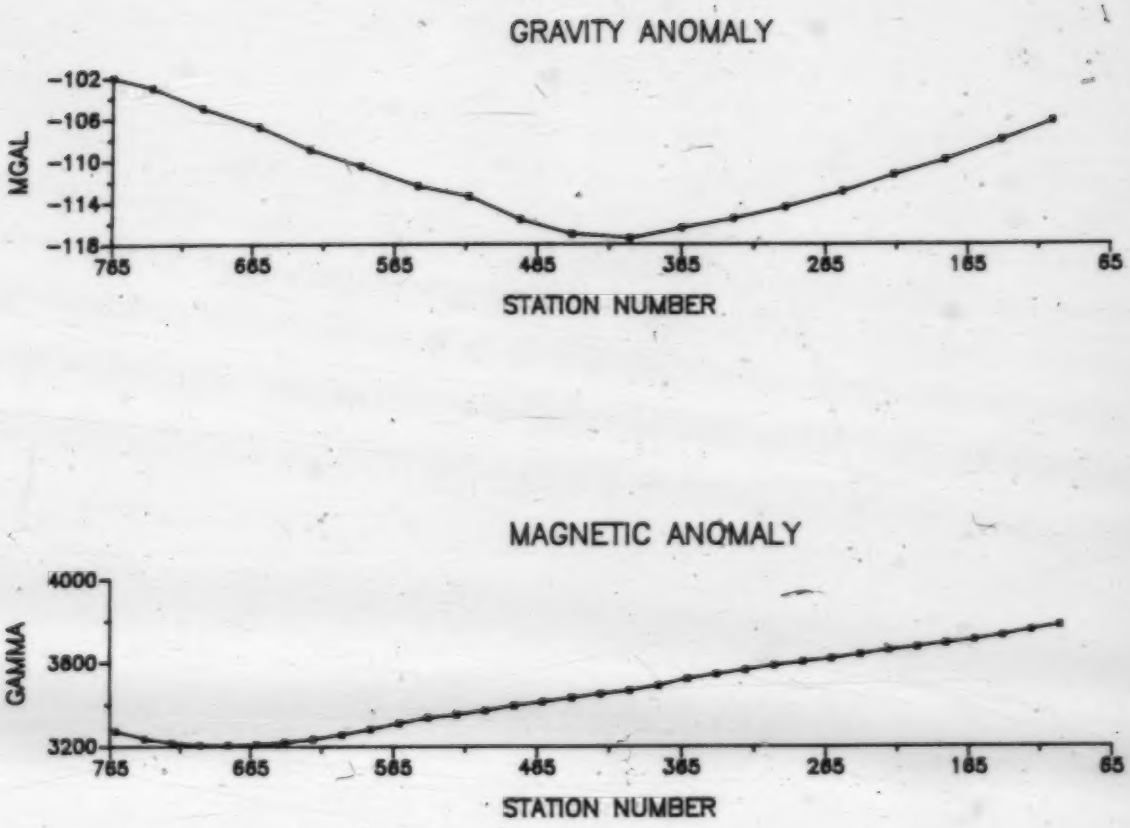

Figure 3.14 (a) The Bouger gravity anomaly and (b) the aeromagnetic anomaly along the Vulcan seismic line.

There are several discontinuous bands of correlatable energy in the Precambrian section beneath 2 secs. These reflecting events are correlatable across a considerable number of seismograms recorded along the continuous north-south profile. After the necessary processing steps, a common depth point stack of these seismograms was plotted as a preliminary cross-section (Figure 3.15). The seismic cross-section so obtained is also known as the brute stack. Two strong shallow reflectors were observed at two way reflection times of 1.0 and 1.4 seconds. These reflections are from the bottom of the Mesozoic and Paleozoic formations. There are no continuous reflectors visible below these two horizons, but reflection characteristics can be seen at several places. Small pieces of deep reflectors are visible between two way reflection times of 6.0 and 12.0 seconds. Although these reflectors are not correlatable throughout the extent of the profile, they do indicate the presence of deep reflecting horizons on the reflection profile. Their discontinuous characteristic is probably due to the fact that the area has undergone severe faulting and intrusion. The seismic records also show that the deep reflecting horizons are not horizontal. There are dips up to 20 degrees, present in this area. Because of the presence of steep dips (dips greater than 5 degs), the reflectors do not show up at their proper positions. This is due to the fact that the traces are corrected for normal moveout under the assumption of horizontal layering and the resulting traces are assigned to the center point between source and receiver. Also it is assumed that the normal reflecting point is situated exactly below the mid point of the source and receiver. For a dipping reflector the normal reflecting point cannot lie exactly below the mid point and hence the seismic section prepared under the assumption of horizontal reflecting boundaries will show the reflectors in displaced positions. These displaced reflectors on the seismic section should be moved to their proper positions in order to get a true picture of the subsurface geology. The process by which these events are moved to their true spatial positions, is known as migration.

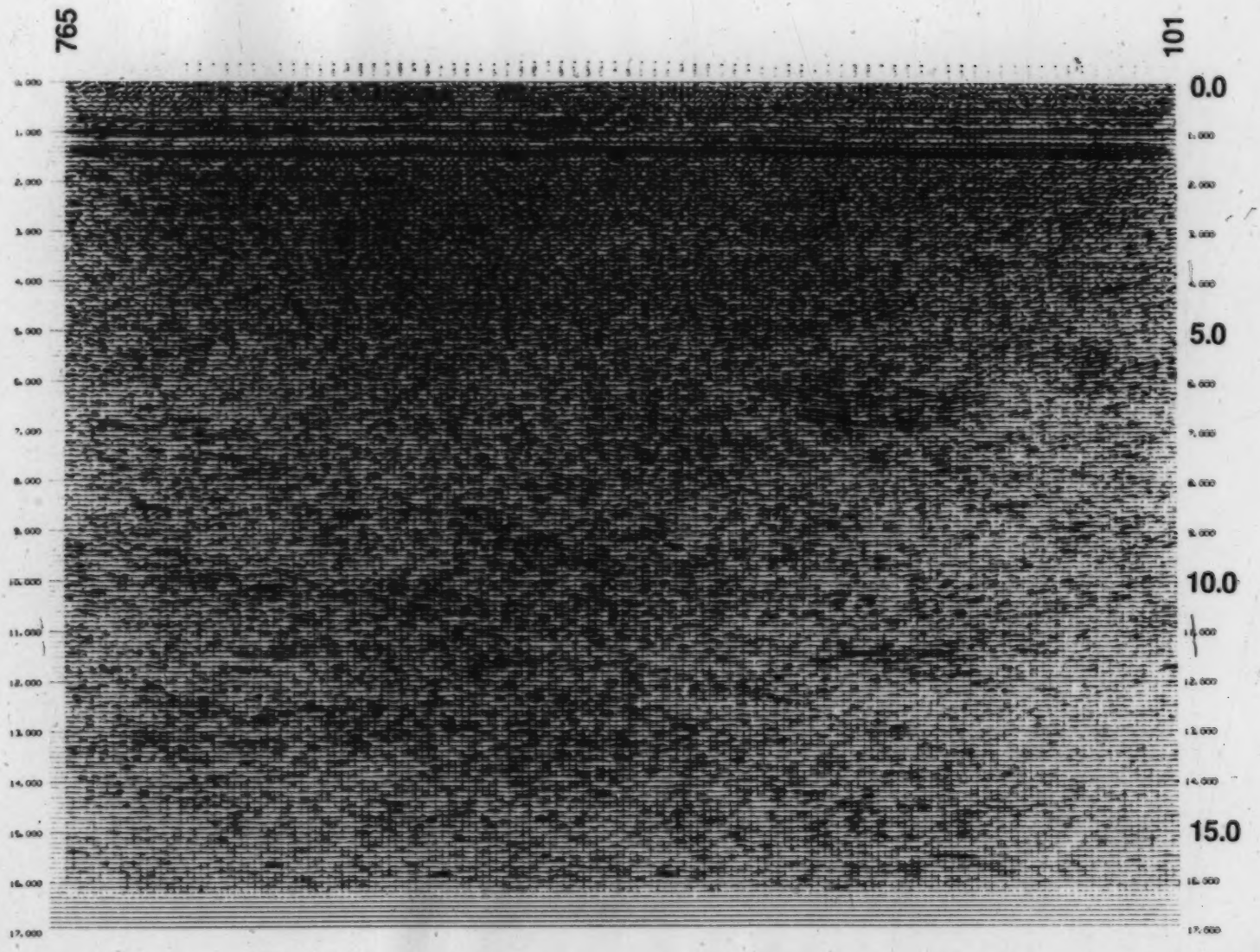

Figure 3.15 A common depth point stacked section of the Vulcan seismic line.

There are several methods used for the migration of seismic data. The most popular and recent amongst all is the wave-equation migration technique. This method is based upon the downward continuation of the recorded wavefield and makes use of the exploding reflector model. This model assumes that each point on a subsurface inhomogenity is a source, and these sources radiate upwards with only half the velocity normally associated with the geological section. Signals received at the surface due to this model are very close to those that would have been generated by sources and receivers occupying the same position on the surface. Also because the model involves waves travelling in one direction, only the upgoing wave of the solution to the wave-equation needs to be dealt with, using one-half of the normal velocities. The sources located at the subsurface inhomogenities explode simultaneously at time t=0 and depths z and the waves propagating from these sources are recorded at time t and depth z=0. In seismic exploration the wavefield at the surface is known, i.e. at z=0 and time t, so that we extrapolate it downwards, using one-half of the normal velocities, till t=o. The resulting picture gives us the true positions of the subsurface horizons. For the Vulcan data a frequency domain migration scheme was used.

The important factor in the migration of seismic data is the subsurface velocities. The velocities should be known fairly well in order to achieve good migration results. A basic assumption in the above mentioned migration technique is that the velocities are constant laterally. The method gives poor results if there are lateral velocity variations. For migrating the Vulcan seismic data, the velocity is not well known and the refraction and wide angle reflection velocities presented by Kanasewich(1968) were used.

The migrated seismic cross-section is illustrated in Figure 3.16. The seismic events are plotted as a function of two-way travel time. On the seismic cross-section, the reflections from the bottom of Mesozoic and Paleozoic are visible very distinctly. The Riel discontinuity, marked R, was identified on the basis of projection from the earlier line and is not a prominent reflector here. The horizon marked M indicates a reflection correlating in

depth with the Mohorovicic discontinuity. There is another distinctly visible midcrustal reflector in the Precambrian, which lies between the Riel discontinuity and the bottom of the Paleozoic. Also there are a number of faults present in Precambrian formations which extend downwards to the Mohorovicic discontinuity. Correlation of various events is based on time ties and reflection characteristics. Reflections have been emphasized by drawing heavier lines. There are no reflectors between the two-way reflection times of 1.4 and 5.0 seconds. However, the reflection characteristics present in this zone may be attributed to the multiple reflection activity due to the presence of two strong shallow reflectors.

As seen from the cross-section, the R discontinuity and the reflector above it have been continuously correlated over the entire length of the profile, while the reflection from M event is not that prominent. Other quasi-continuous horizons usually of poorer quality are also present.

The seismic cross-section of Figure 3.16 presents strong evidence for faulted and steeply dipping structures within the crust. Over the extent of the profile the Riel discontinuity varies in depth from 26 to 37 kms, whereas M varies in depth from 37 to 46 kms. This compares very well with previous investigations. Another midcrustal reflector marked C, varies in depth from 13 to 24 kms. This reflector was not identified in previous seismic work.

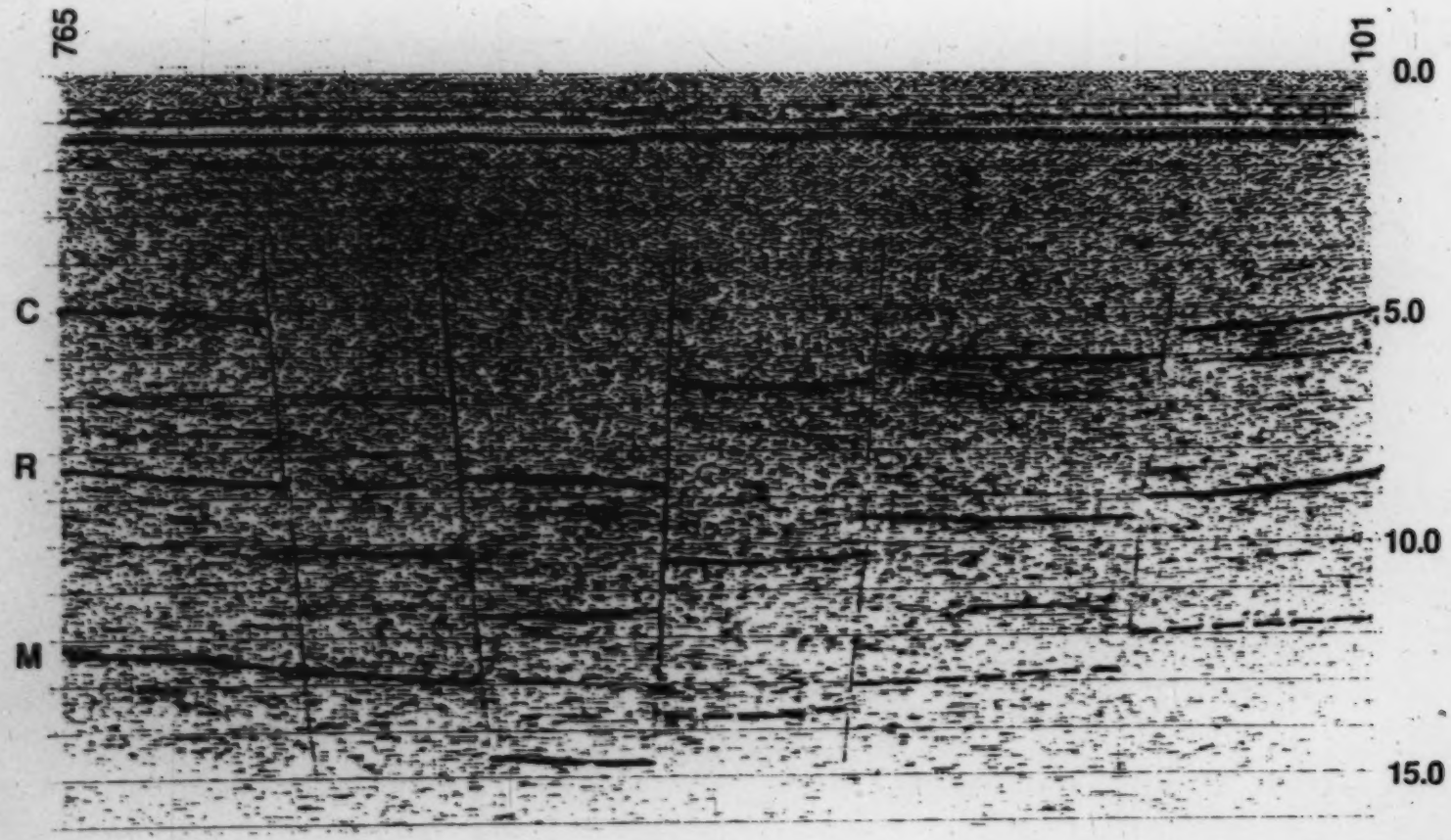

Figure 3.16 f-k migrated section of line 83-421 along with its interpretation.

The consistency of the reflection correlation across a faulted terrane can be assessed by making two dimensional gravity calculations. An attempt was made to prepare a gravity model of the seismic cross-section. For this purpose the interpreted seismic section was divided into several distinct blocks. Figure 3.17 shows the block diagram of gravity anomaly. The depth and thickness of each block was calculated based on the compressional wave velocity and two-way reflection time. The faults marked their lateral boundaries. The density contrasts are assigned to each block based on velocities and reflection characteristics. For the present study the values for density were taken from previous studies. The density contrasts for each block are also shown in figure 3.17.

The gravitational attraction due to a two-dimensional rectangular block is required in order to compute gravity anomaly along the profile due to the block model. The gravitational attraction due to the shaded block of Figure 3.18, at a point P on the surface is given by the following expression (Talwani et.al. 1959)

$$\Delta g_p = 2K\delta \left[x \ln \sqrt{\frac{D^2+x^2}{d^2+x^2}} - (x-b) \ln \sqrt{\frac{D^2+(x-b)^2}{d^2+(x-b)^2}} \right.$$

$$+ D\left(\tan^{-1}\frac{x}{D} - \tan^{-1}\frac{(x-b)}{D} \right)$$

$$\left. + d\left(\tan^{-1}\frac{x}{d} - \tan^{-1}\frac{(x-b)}{d} \right) \right] \qquad (3.23)$$

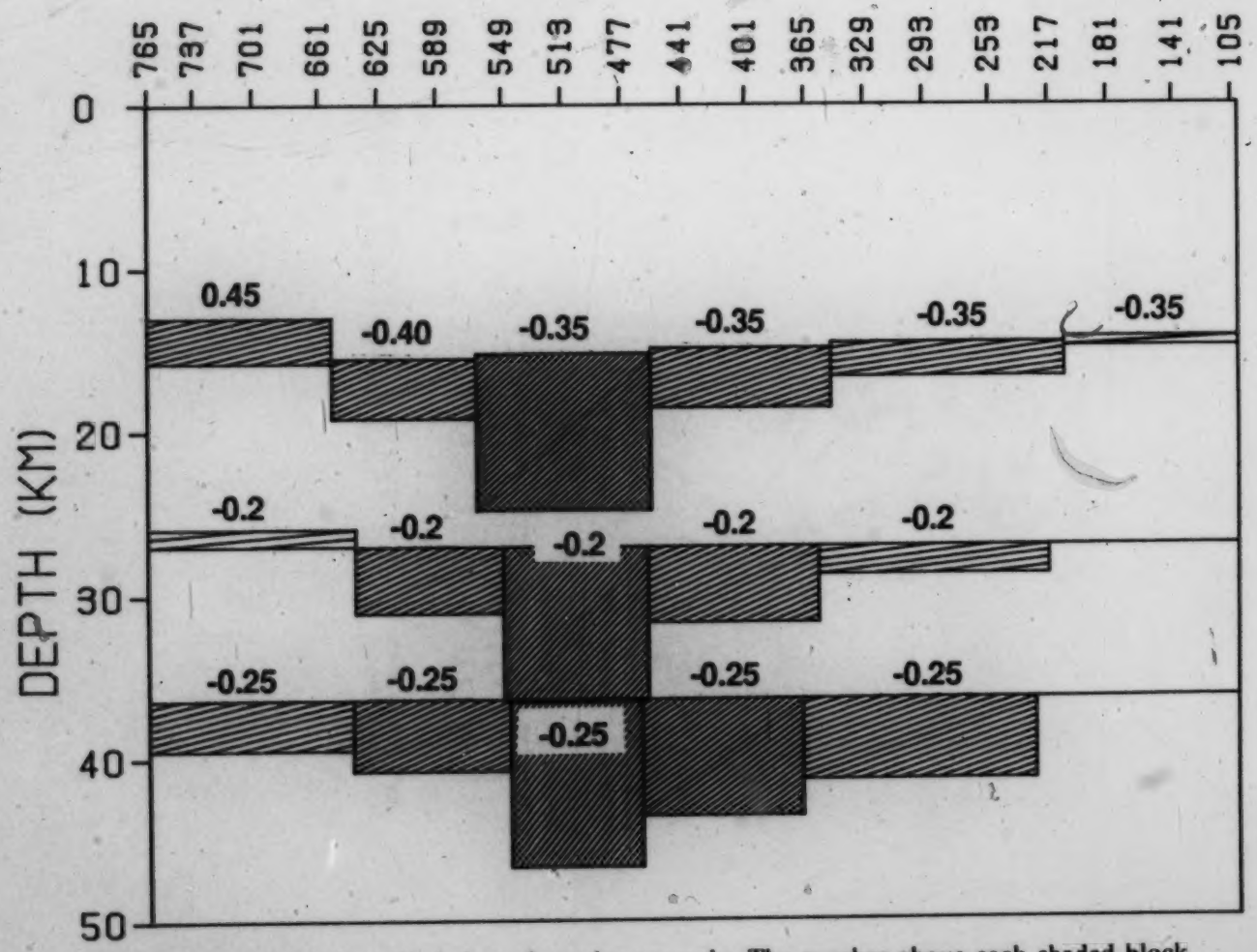

Figure 3.17 The model used for the calculation of gravity anomaly. The number above each shaded block represents the density contrast in gm/cc.

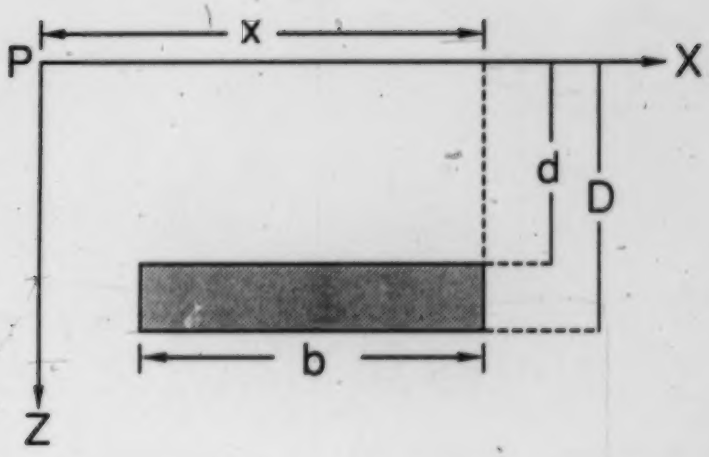

Figure 3.18 The schematic diagram for gravitational attraction due to shaded block at location P.

Here 'K' is the gravitational constant, 'δ' is the density contrast, 'x' is the horizontal distance to the right edge of the rectangular block, 'b' is the lateral extent, 'D' is the depth to the bottom and, 'd' is the depth to top. The gravity values due to each block are calculated at various stations along the profile. Then by adding the values at each station we get the gravitational attraction due to the seismic model. The computed gravitational attraction due to the seismic model is shown in Figure 3.19 along with the observed gravity values. There is not significant discrepancy between the observed gravity values and the computed ones. Therefore the seismic model is not far from the true subsurface picture.

The Vibroseis reflection survey carried out in the Vulcan area of southern Alberta shows distinct deep reflectors which are related to the crustal structure. The steep dips encountered necessited migration of the data. The seismic cross-section shows two good shallow reflectors between 0.5 and 1.5 seconds. The uppermost deep reflector varies in depth between 5 and 8 seconds. This reflector was not observed in previous studies. In general the structure appears to be very complex with several faults interrupting the continuity of reflectors. The interpretation of seismic and gravity data indicates that this section crosses a complex faulted graben associated with a Precambrian rift valley. Faults of small throw are thought to intersect the shallow reflectors. The identification of these faults is very important in obtaining a true picture of the subsurface. Also it is very important in oil prospecting, since they may form potential oil traps.

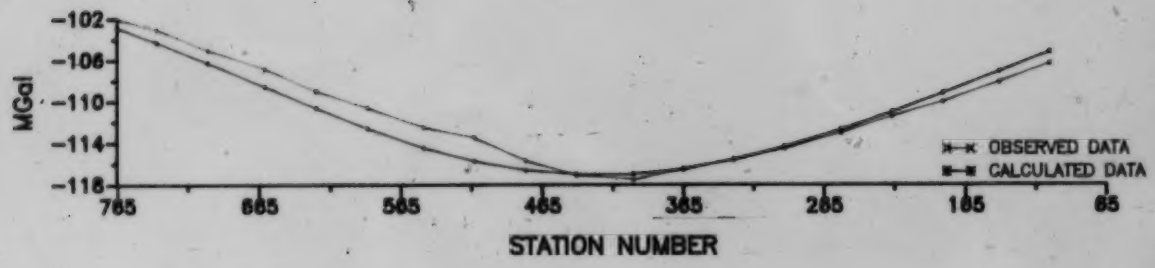

Figure 3.19 A comparison of observed and calculated gravity anomalies.

To test the performance of the CFP stacking method, we applied it to a small portion of the line (stations 440 to 500). A CMP stacked section of this portion is shown in Figure 3.20. On this section a strong shallow reflector is present at two-way reflection time of 1.4 sec, whereas the reflector at two-way time of 1.0 sec is of poor quality. A fault was thought to cross these reflectors between stations 471-479. This interpretation is questionable since the reflecting horizon at 1.4 sec appears quite continuous. It was thought that there may be a fault of small magnitude through the reflector at 1.4 sec, which cannot be identified on a CMP section due to the overlapping of diffractions. In order to resolve this question, a CFP stacked section of the same portion of the line was obtained and is shown in Figure 3.21. The velocity model used for the CFP stacking was the same as that of CMP stacking. In order to emphasize high amplitudes on CFP section, only the peaks and troughs having amplitudes above a preset threshold were colored. On this section high amplitudes are present between stations 471-476 and stations 457-464 at the two way reflection time of 1.4 sec, indicating that there are discontinuities. This is in good agreement with the interpreted fault through this reflector, thus reducing the ambiguity. Therefore when the CFP stacked section is interpreted along with the CDP stacked section, a better picture of the subsurface structures can be obtained.

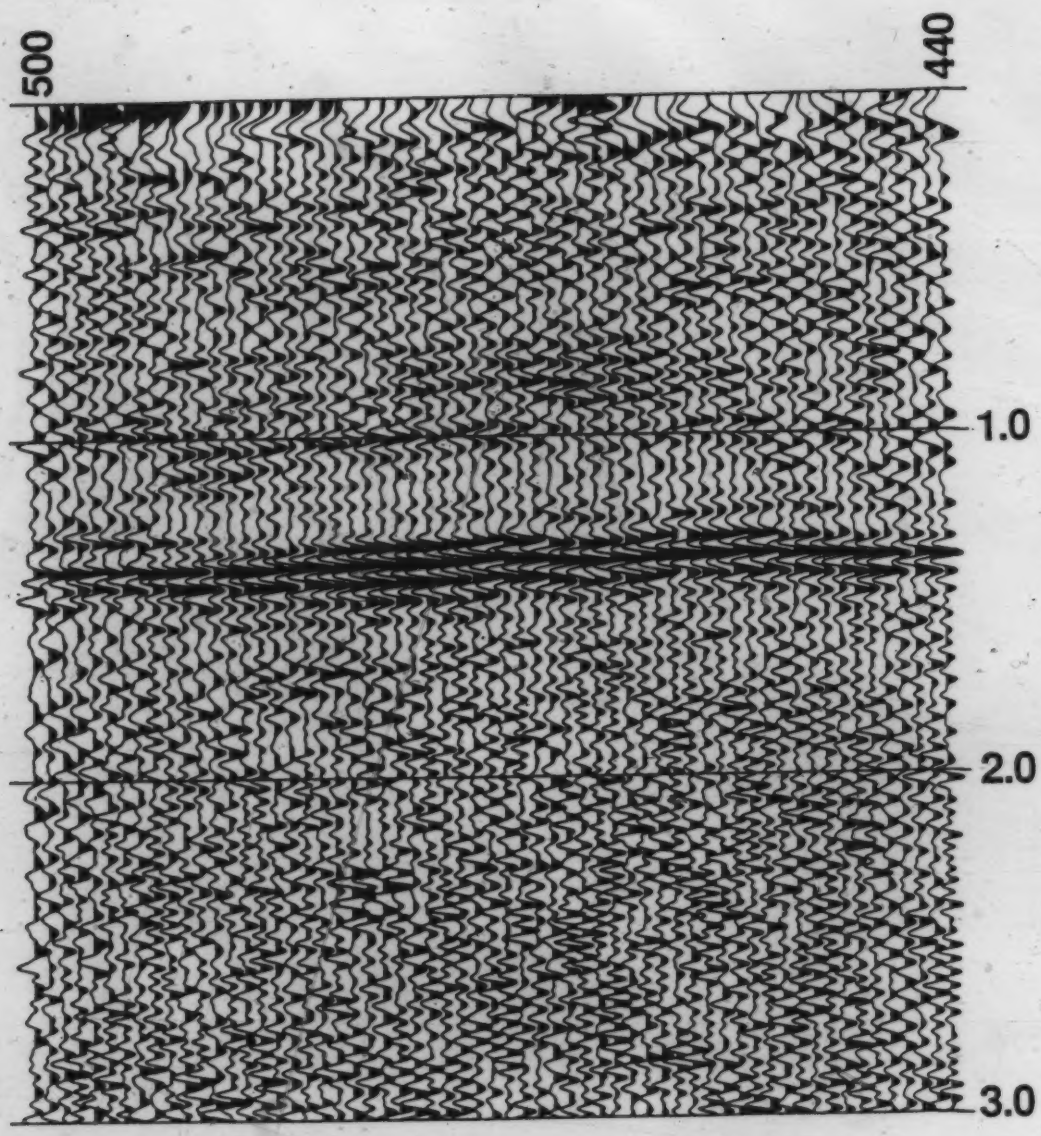

Figure 3.20 A CMP stacked section of a small portion (stations 440 to 500) of Vulcan Line.

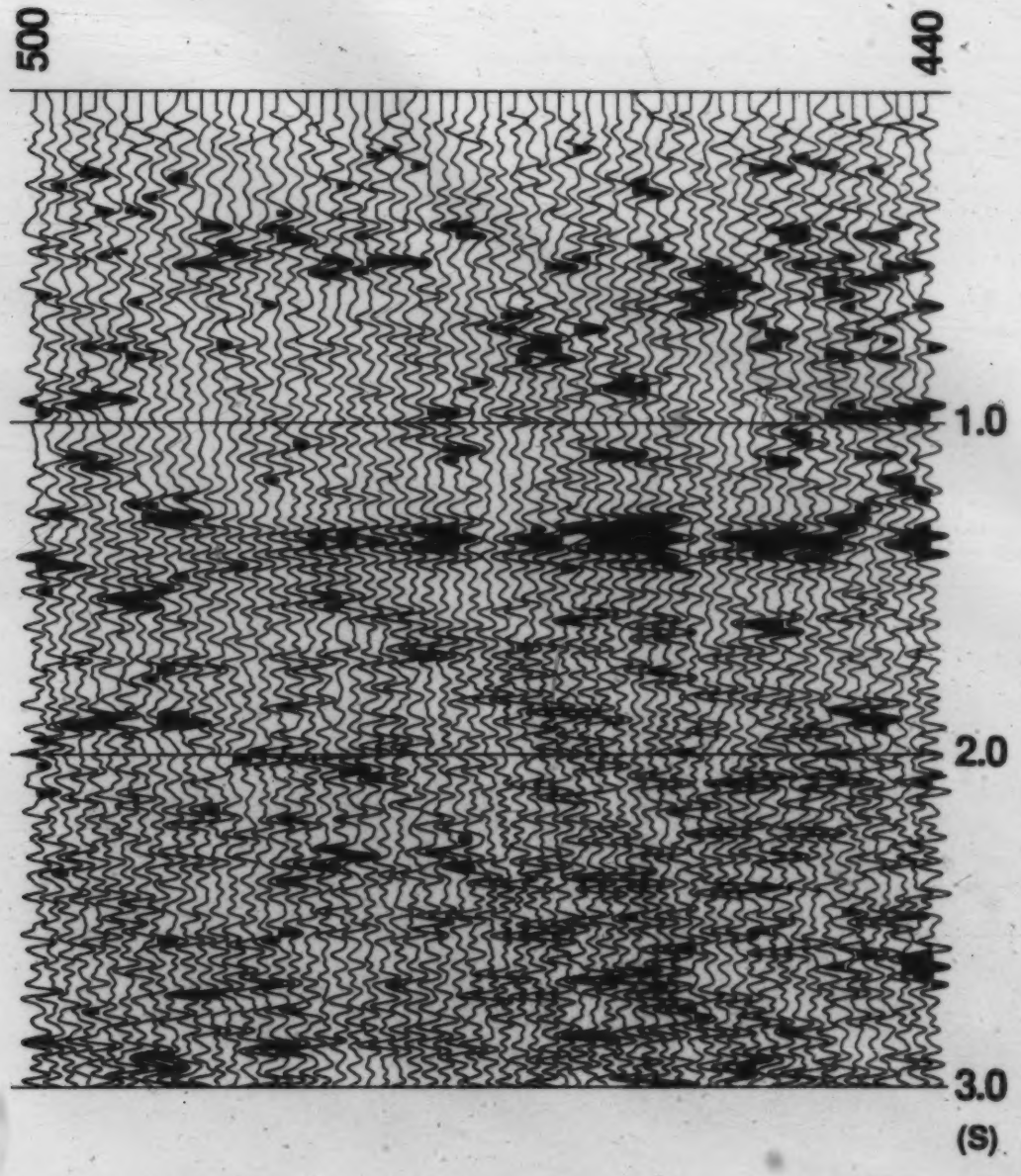

Figure 3.21 A CFP stacked section of the portion of Vulcan Line shown in Figure 3.20.

3.6.2 Application to data from south of Princess Well in Alberta

Next the CFP stacking method was applied to the reflection data from an EW line situated south of the Princess Well in Alberta. Figure 3.22 shows the location map of the line. The data was acquired by PanCanadian Petroleum Limited in March 1985 and a small portion of this line (approximately 6.8 km in length) was made available to us for CFP stacking. The seismic instrumentation consisted of a 120-channel DFS-V recording system employing airgun sources. An inline split-spread shooting pattern with a shot point interval of 34 m and a receiver group interval of 17 m was used. Each receiver group comprised of 9 geophone units in an inline pattern.

A CMP stack of this data with a maximum of 30-fold coverage after basic processing is shown in Figure 3.23. A very strong reflector (the top of the erosional surface of Mississippian deposits) at a two-way reflection time of 0.83 sec can be seen on this section. The reflectors between 1.0 and 1.4 sec are from Cambrian formations. The Precambrian crystalline basement is probably at 1.4 sec and is relatively continuous throughout the section except for the interruption by diffraction arcs. Note that the diffracted energy is quite remarkable on this section, and has not been completely removed by common midpoint stacking. If diffractions were not present no discontinuity would be infered in the reflecting horizons. In order to locate any discontinuities due to small faults or due to sudden change in lithology in this area, the CFP method was applied to this data.

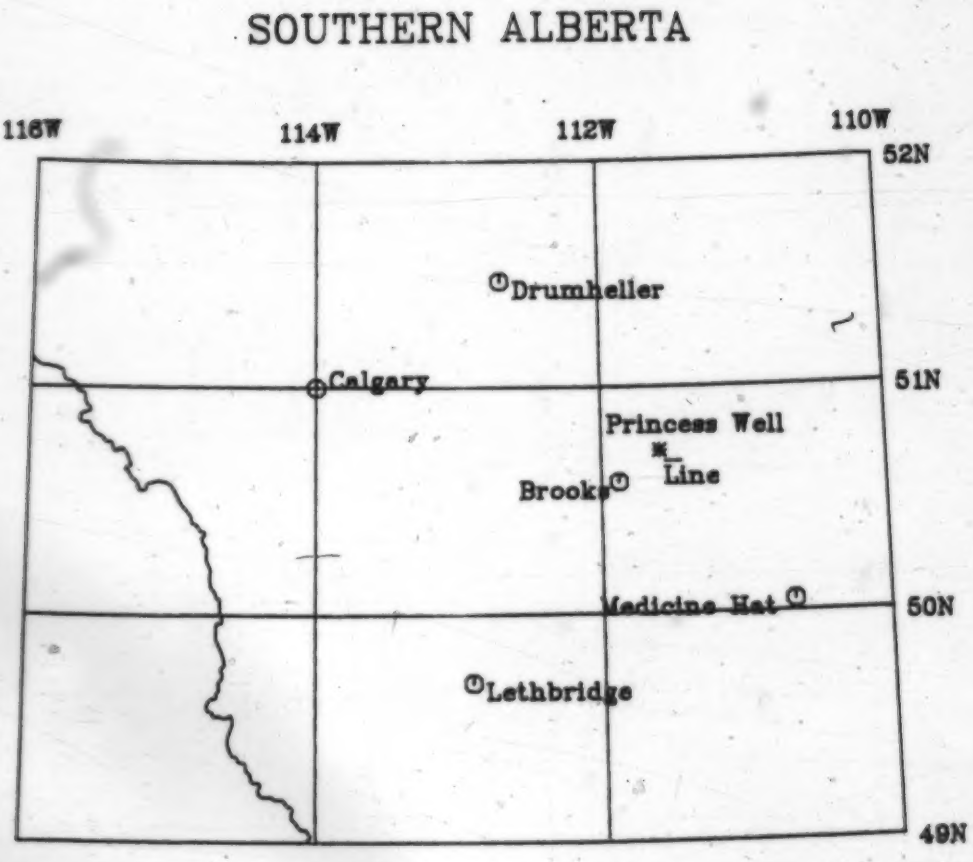

Figure 3.22 Map of Southern Alberta showing the location of the seismic line.

Figure 3.23 A CMP stacked section of a portion of the seismic line from Princess area. The data is courtesy of PanCanadian Petroleum Ltd. 2WS - Second white specks, bFS - base Fish scale, M - top of Mississippian, Wab - Wabamun, A - Arctomys, P - Pika, S - Stephen PC - Precambrian.

A CFP stacked section is shown in Figure 3.24. In order to emphasize high amplitudes on this section, the peaks and troughs having amplitudes below a certain level were not filled in. High amplitudes correspond to reflector discontinuities which may result from either faulting or sudden termination of a reflector or any lateral discontinuity in seismic velocity. One more important feature which can be seen on a CFP stacked section is the change in phase as one goes from one side of the fault to the other. Presently we don't dwell in detail the exact nature of these phase reversals and their role in locating faults accurately in space. This will be done after modelling in a later stage using finite difference synthetic seismograms for more complicated media.

The seismic section is on the northern edge of a major east-west rift of Precambrian origin (Kanasewich, 1968). It is also 6.4 km south of a well drilled through 1874 m of Phanerozoic sediments into a basement high with the basal core being a mafic metamorphic rock (R.A.Burwash, 1987, personal communication). The anomaly has a positive gravity expression and is presumed to be a volcanic extrusive through middle Cambrian sediments as a part of the rifting process. The diffraction patterns on the seismic section (Figure 3.23) interrupting Middle Cambrian Arctomys, Pika, and Stephen formations are interpreted as representing igneous intrusives (a in Figure 3.25) with some possible reactivation (b) and faulting (b) during the subsequent Paleozoic era. An interpretation of the section based on the CMP section and the CFP section is shown in Figure 3.25. Other diffracted patterns (c and d) may be due to erosional features, faults or carbonate buildups. In conclusion, with the help of the CFP section it was possible to delineate the boundaries of the igneous intrusive. Also the faults and other discontinuities were easier to identify with the aid of this CFP section. Thus a better picture of the subsurface was obtained.

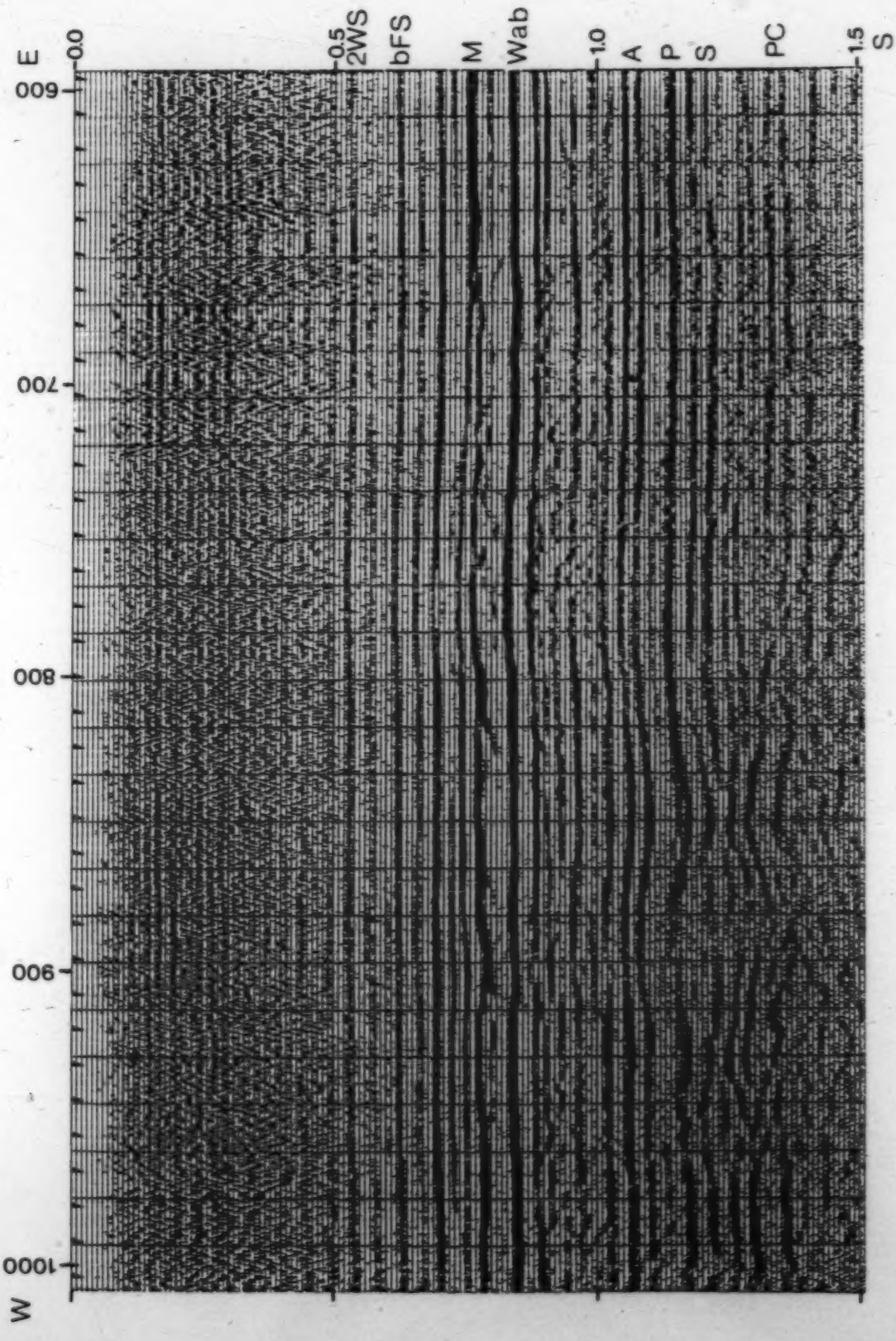
E
600
700
800
900
1000
W
0.0
0.5
2WS
bFS
M
Wab
1.0
A
P
S
PC
1.5
S

Figure 3.24. A CFP stacked section of the line from Princess area. The solid shaded peaks indicate a positive polarity on the diffraction stack. The shaded gray peaks indicate negative polarity.

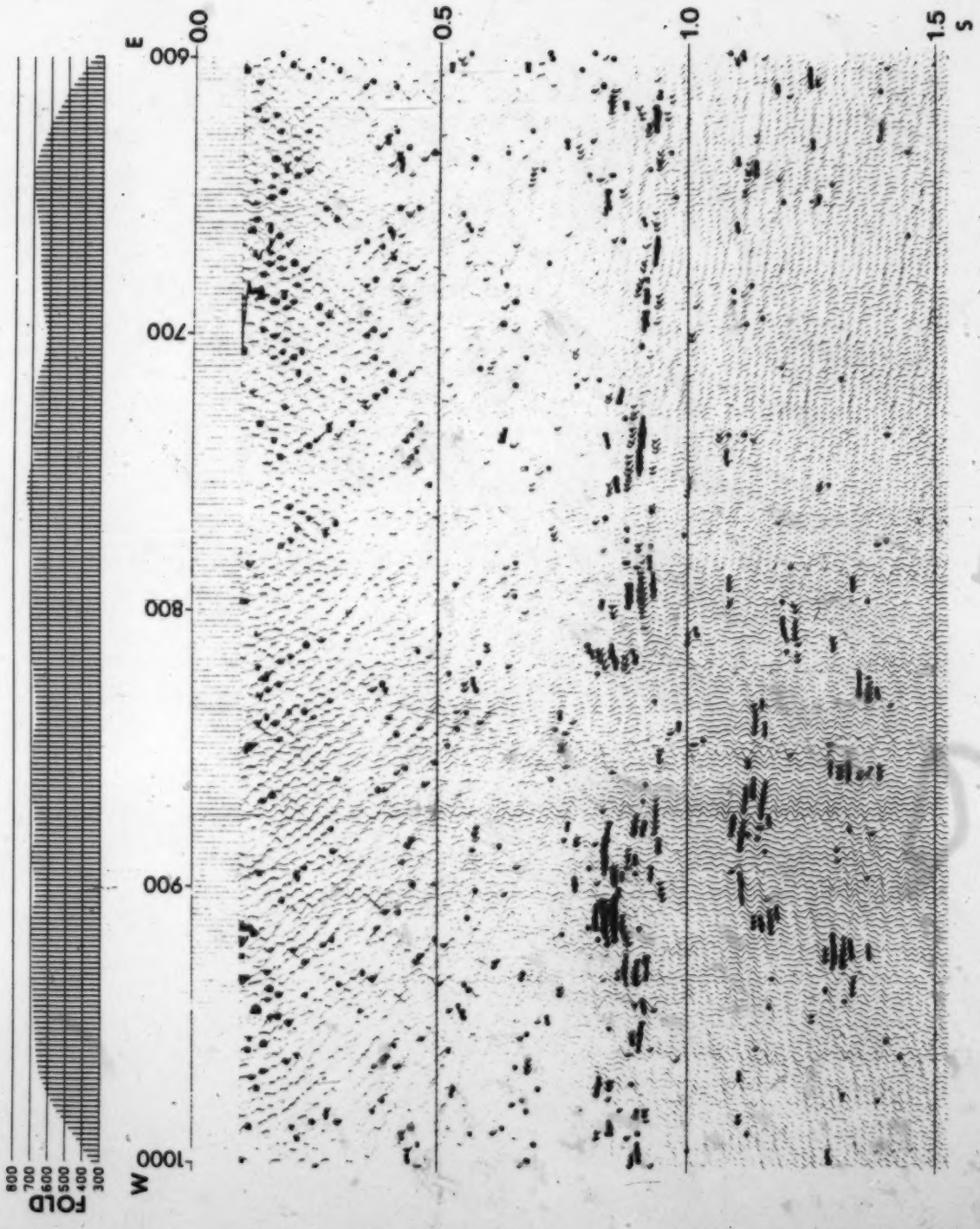
E
W
600
700
800
900
1000
0.0
0.5
1.0
1.5
s
FOLD
800
700
600
500
400
300

Figure 3.25 A line drawing of the Princess section along with the diffraction and fault interpretation made on the basis of the CFP stacked section. a. Boundary of the igneous intrusive, b. possible reactivation, c. possible erosional feature or carbonate buildup, d. faulting.

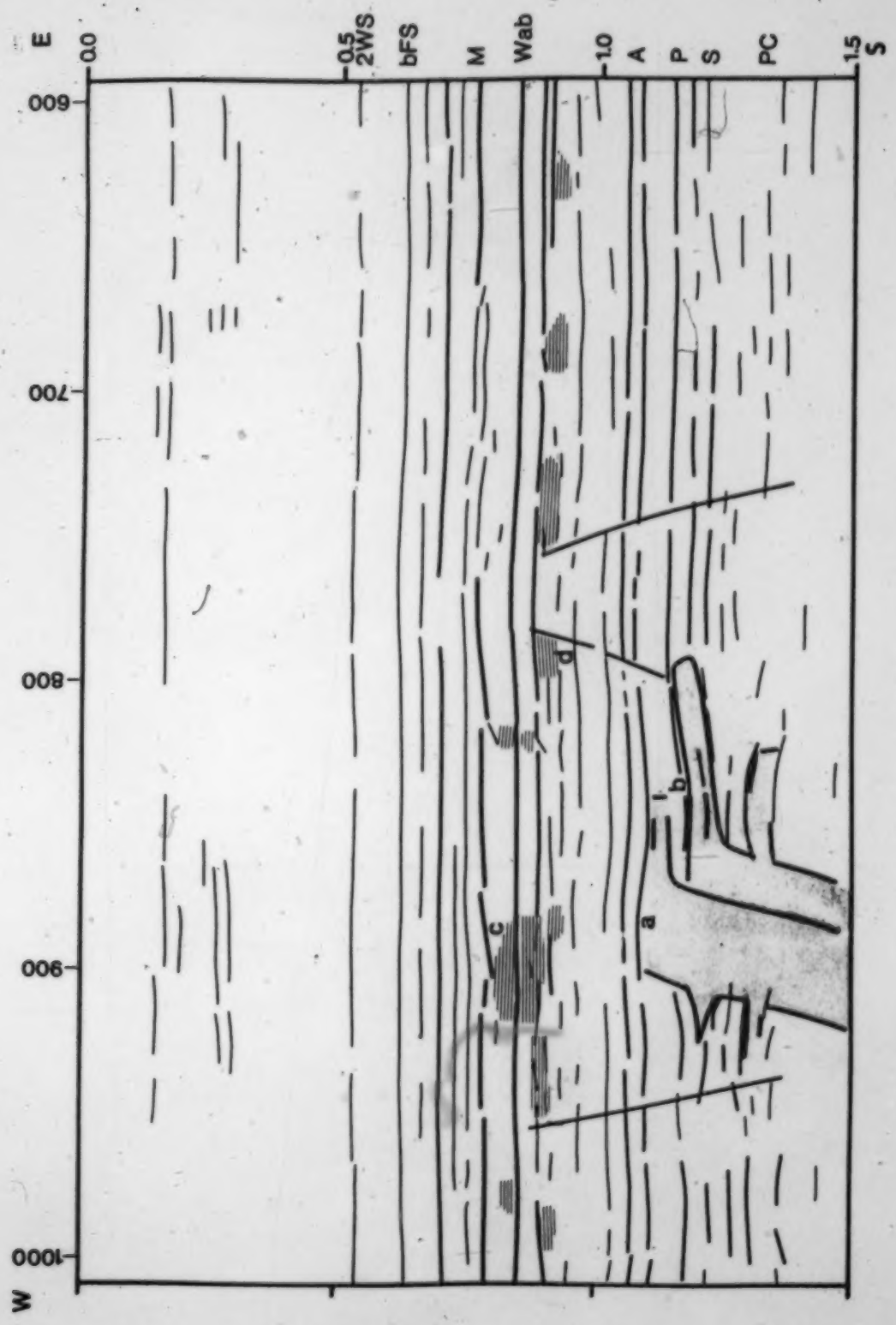
E
0.0
0.5
2WS
bFS
M
Wab
1.0
A
P
S
PC
1.5
S
600
700
800
900
1000
W
a
b
c
d

Depth migration before stack also collapses all the diffraction hyperbolas to their respective apexes, but the computing cost is prohibitively expensive. Instead two plots of continuity and discontinuity would serve the same purpose at a relatively lower cost. Another advantage of having a CFP stacked section is the fact that it shows the discontinuities explicitly and hence can be useful to locate them even if the dimensions are small, e.g. a fault with a small throw. On migrated sections it might be difficult to locate such features since reflections are also present. The interpretation must be carried out by superimposing the CFP stacked section on top of the CMP stacked section. An attempt was made to plot both sections, one on top of the other, with different colors. But due to inadequate plotting facility at the University the results were not satisfactory.

The method also seems to be helpful in preventing an interpreter from choosing a diffraction event as an anticline on the CMP stacked section. The scattering due to an anticline is much weaker as compared to that for a sharp discontinuity. Hence on a CFP stacked section an anticline will not show high amplitude, whereas a sharp discontinuity can be located by high amplitude.

3.6.3 Application to data from Melville Island

Next the CFP stacking method was applied to the reflection data from a NS line (67-X) from Melville Island. Figure 3.26. shows the location map of the line. The data was acquired by Chevron in October 1972. The seismic instrumentation consisted of a 48-channel DFS-V recording system employing explosive sources. An inline split-spread shooting pattern with a shot point interval of 880' and a receiver group interval of 220' was used. Each receiver group comprised of 9 geophone units in an inline pattern, with geophone spacing of 25'.

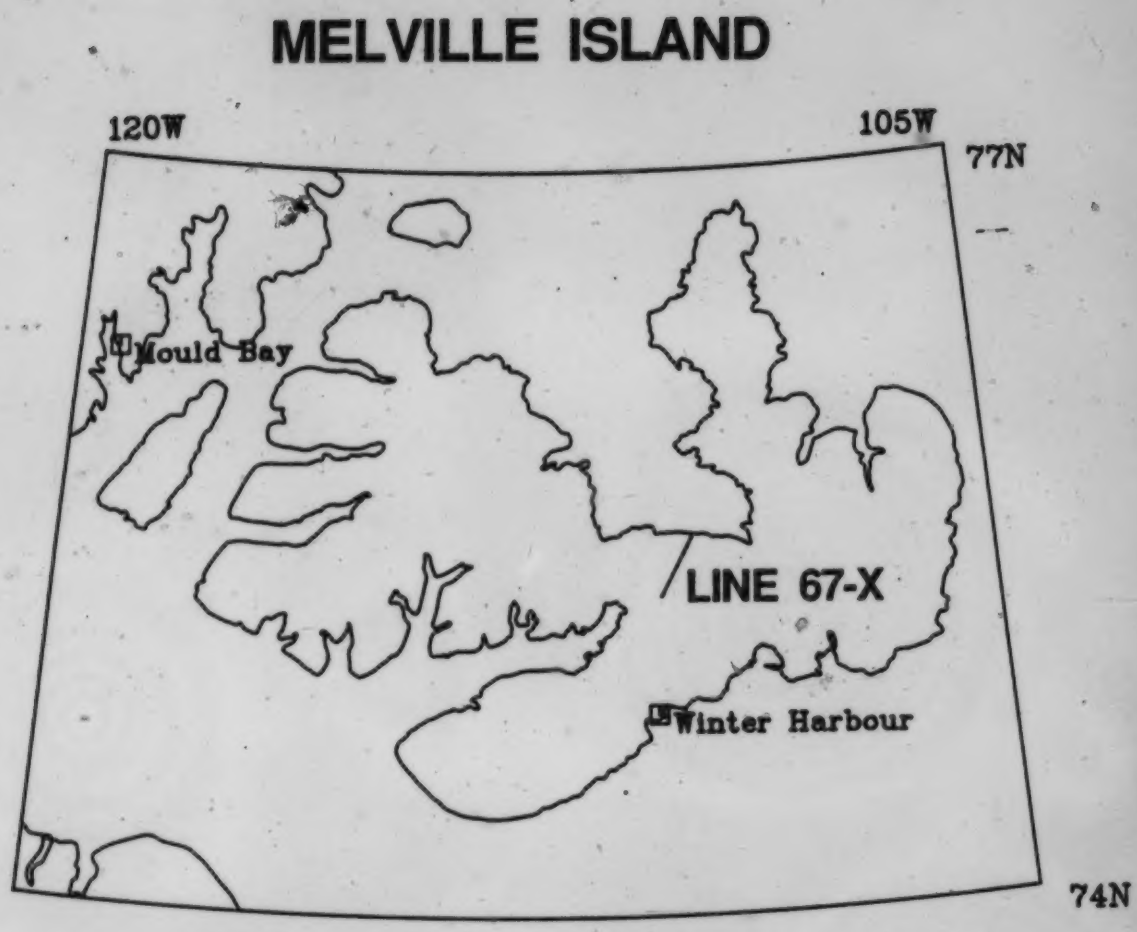

Figure 3.26 A map of Melville Island along with the location of the NS line 67-X.

A CDP stack of this data with a maximum of a 6-fold coverage after basic processing is shown in Figure 3.27. There are several strong reflectors present on this section with evidence of folding and faulting. There is a well drilled through location 270 of this line. The horizons are identified by correlating them with the well data and are marked on the CDP section.

The CDP section along the line shows that the structure in this region consists of a very complex fault system. Two systems of faulting are indicated which are late Devonian and early Mississippian in age. The earlier of these two faulting systems resulted from a northern compressional force with the later one from a southern compressional force. There are two other major structural/ stratigraphic features:

1. The buildup of limestone in the lower Devonian formations.

2. The varying thickness of the Ordovician evaporite section (indicated as a salt unit) suggests that the movement of salt gave rise to anticlinal features on the section. This salt tectonic feature preceded the compressional forces.

The reflectors are relatively continuous throughout the section except for the interruption by diffraction arcs. Note that the diffracted energy is quite remarkable on this section, and has not been completely removed by common midpoint stacking. If the diffractions were not present it would be difficult to infer any discontinuities in the reflecting horizons. In order to locate any discontinuities due to small faults or due to sudden change in lithology in this area, the CFP method was applied to this data.

A CFP stacked section is shown in Figure 3.28. In order to emphasize the high amplitudes on this section, only the peaks and troughs having amplitudes above a certain preset threshold value are plotted. High amplitudes correspond to reflector discontinuities which may result from either faulting or sudden termination of a reflector or any lateral discontinuity in seismic velocity. The boundary between the Silurian and U. Ordovician formations is clearly visible on CFP section. This is due to the change of facies at the

Figure 3.27 A CDP stack of the seismic data from line 67-X. D - Devonian, S - Silurian, UO - Upper Ordovician, MO - Middle Ordovician, C - Cambrian, PC - Precambrian.

THE QUALITY OF THIS MICROFICHE IS HEAVILY DEPENDENT UPON THE QUALITY OF THE THESIS SUBMITTED FOR MICROFILMING.

UNFORTUNATELY THE COLOURED ILLUSTRATIONS OF THIS THESIS CAN ONLY YIELD DIFFERENT TONES OF GREY.

LA QUALITE DE CETTE MICROFICHE DEPEND GRANDEMENT DE LA QUALITE DE LA THESE SOUMISE AU MICROFILMAGE.

MALHEUREUSEMENT, LES DIFFERENTES ILLUSTRATIONS EN COULEURS DE CETTE THESE NE PEUVENT DONNER QUE DES TEINTES DE GRIS.

MELVILLE ISLAND LINE 67-X
CDP STACK

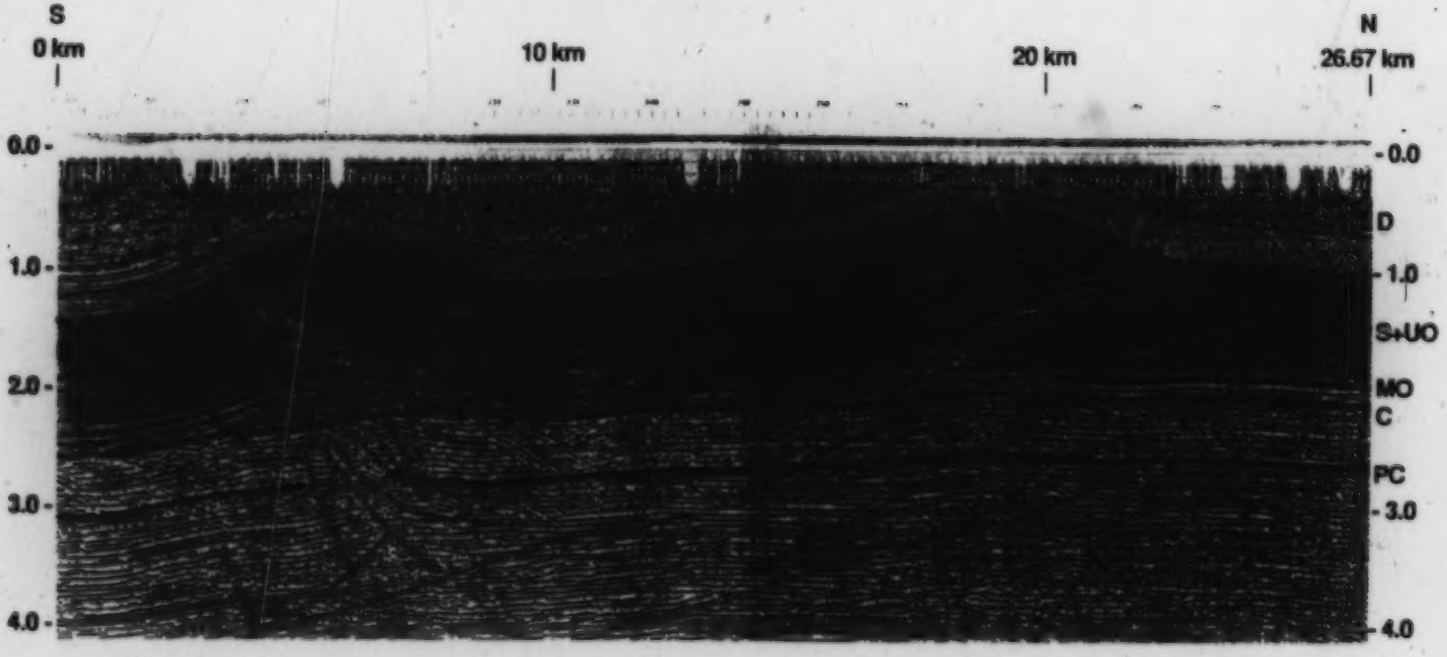

boundary. The outline of the salt unit is also quite remarkable on the CFP stacked section. Besides these two major features there are several indications of faulting. The interpretation carried out so far is also illustrated in Figure 3.28.

Velocity model plays a very important role in CFP stacking process. Due to the computing limitation at the University we could not experiment the stacking process with various velocity models.

3.7 Conclusions

A new processing method was developed to image seismic acoustic impedance discontinuities by using the diffracted elastic energy. The process is analogous to the conventional CDP method. The CFP method destroys the reflected energy and concentrates the diffracted energy at the location of diffracting centers. The method exploits the difference in reflection and diffraction moveouts. An amplitude correction is also incorporated to compensate for the rapid fall of diffraction amplitude from receiver to receiver.

Synthetic data as well as real data show that the CFP stacking method helps in the identification of subsurface discontinuities by stacking diffracted energy at diffracting points. The CFP section is a complementary presentation to the normal CMP stacked section. Therefore it helps the interpreter in determining the structure of the subsurface. The method appears to be particularly useful for finding unconformities, lateral inhomogeneities and faults with throws of small magnitude.

Figure 3.28 A CFP stack of the seismic data from line 67-X. Peaks (blue) and troughs (red) having amplitudes above a preset threshold are plotted.
Light blue - boundary between Silurian and Upper Ordovician, Pink - salt unit.

MELVILLE ISLAND LINE 67-X
CFP STACK

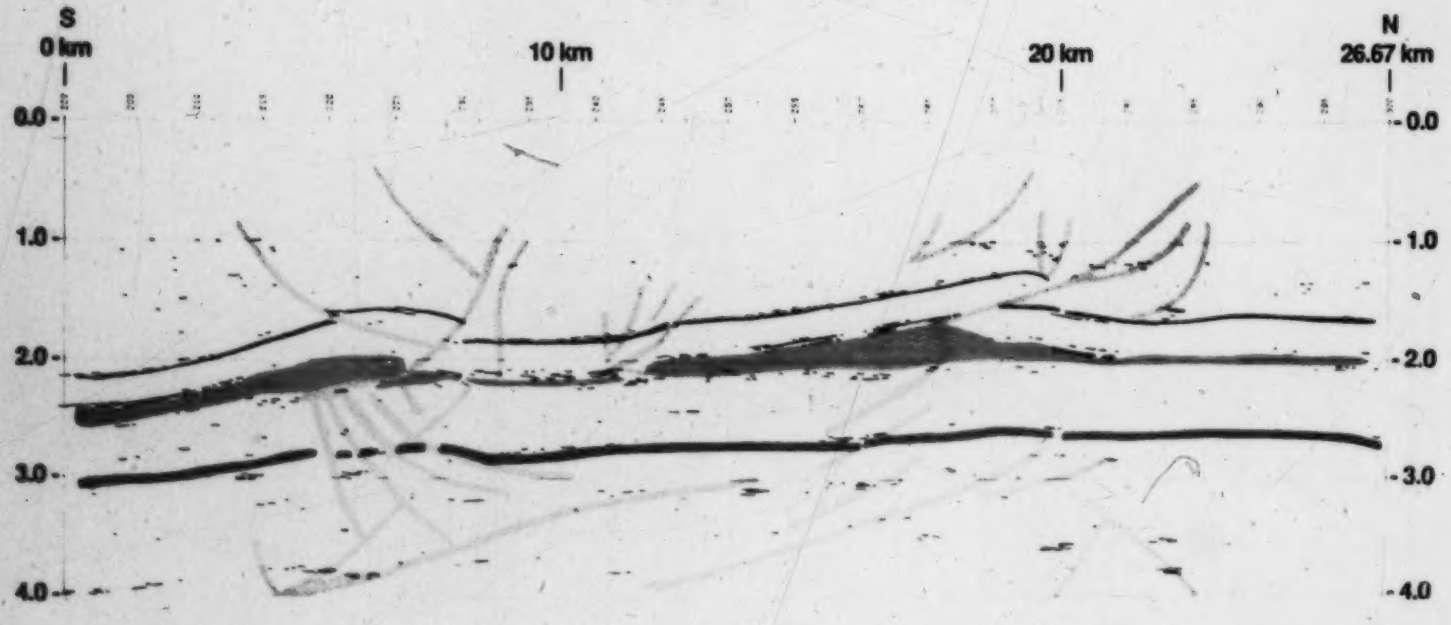

CHAPTER 4

RESOLUTION WITH REFLECTED AND DIFFRACTED WAVES

4.1 Introduction

The Common Fault Point (CFP) method described in chapter 3 is quite promising for imaging seismic subsurface discontinuities. The imaging method makes use of the diffracted waves produced by discontinuities and is sensitive to several physical parameters. Source signature, subsurface velocities and the dimensions of the discontinuity are a few of the important parameters which affect the resolution on CFP stacked section. To achieve the best results in interpretation, due consideration must be given to effects produced by these parameters.

This chapter describes the limitations imposed by these parameters on the interpretation of the CFP section. The problems of vertical and lateral resolution of a method are the most important of all for interpretation. Broadly speaking the resolution is dependent upon the dominant frequency in the source pulse, therefore it is important to know the nature of the source pulse before hand. We begin with a description of the source wavelet used for the following study.

4.2 Description of the source pulse

The time variation of the source pulse for generating the synthetic seismograms is expressed by

$$f(t) = t \exp(-\alpha t^2) \tag{4.1}$$

where α is a source constant. Any bandlimited pulse of finite time duration can be used. I have used this expression because it is mathematically more tractable. Also during processing the pulse can be shaped to any desired form by deconvolution. The frequency spectrum of the source pulse is given by

$$F(\omega) = \frac{1}{2\pi} \int_{-\infty}^{\infty} t\, e^{-\alpha t^2} e^{-i\omega t}\, dt$$

$$= -\frac{i\,\omega}{4\pi^2 \alpha^{3/2}} \exp[-\omega^2/4\alpha] \qquad (4.2)$$

The maxima of the amplitude spectrum is obtained by equating the first derivative to zero i.e.

$$F'(\omega) = \frac{1}{4\pi^2 \alpha^{3/2}} \left[1 - \frac{\omega^2}{2\alpha}\right] \exp[-\omega^2/4\alpha] = 0 \qquad (4.3)$$

This gives the dominant frequency $\omega_0=(2\alpha)^{1/2}$. This frequency is dependent upon the source constant α. Therefore a source pulse with a particular dominant frequency can be generated by finding α from

$$\alpha = \frac{\omega_0^2}{2} \qquad (4.4)$$

For a source pulse with a dominant frequency of 30 Hz α=17765. The time domain representation of this pulse and its amplitude spectrum are shown in Figures 4.1a and 4.1b respectively. The peak to trough width of the pulse calculated in time domain is $(2/\alpha)^{1/2}$. The above mentioned representation of the source pulse is chosen in order to derive conclusions regarding the relationship between wavelength and resolution.

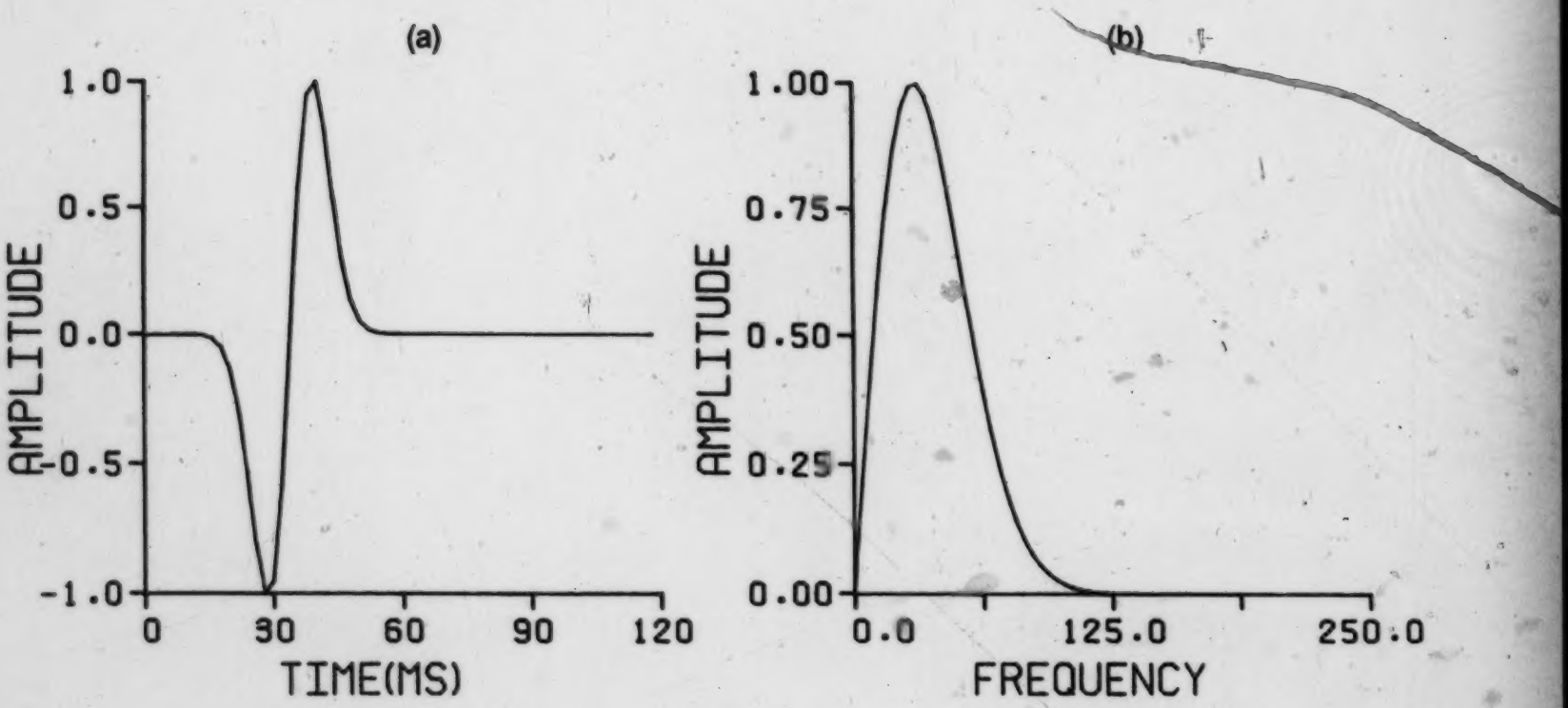

Figure 4.1 (a) Time domain representation of the seismic pulse used for generating synthetic seismograms for the step fault and dyke models. (b) Amplitude spectrum of the source pulse.

4.3 Resolution of the CFP Stacking Method

The determination of vertical and lateral extent of discontinuities is as important as detecting their presence. In reflection seismology several attempts have been made to increase the resolving power of the seismic method. The size of the Fresnel zone (Sheriff 1980) and the basic characters of the seismic wavelet are the most important factors controlling the horizontal and vertical resolution respectively. The problem of vertical resolution is discussed by Widess (1973), Schoenberger (1974), Sheriff (1977), Koefoed (1981), and Kallweit and Wood (1982). Here we shall apply the same principle to determine the resolving power of the CFP stacking method.

Resolution is the ability to distinguish separate features, and is commonly expressed as the minimum distance between two features, such that two can be defined rather than one. Seismic interpretation is concerned with resolution in two directions, vertical (in time or in depth) and horizontal (from trace to trace). In this section, first some definitions for the resolution are presented followed by the discussions of vertical and horizontal resolution. Since the characteristics of the seismic wavelet are the basic factors affecting the vertical resolution, we derive the resolution criterion for the wavelet of section 4.2.

4.3.1 Definitions of resolution criteria

Rayleigh (Longhurst, 1967, p.165), Ricker (1953), and Widess (1973) described several resolution criteria. They considered symmetric zero-phase wavelets, whereas here we use these criteria for an antisymmetric wavelet. However, the definitions for the resolution criteria are still valid.

Rayleigh's Criterion

In the optical analogy a point source is similar to a reflection spike, an optical

instrument is analogous to the earth, and the diffraction pattern plays the role of a band limited wavelet. When parallel light rays pass through a narrow slit, a diffraction pattern is produced. The intensity of the central maximum has a finite width inversely proportional to the slit aperture (Figure 4.2). Rayleigh observed empirically that there is a limit of resolution between two diffraction slits. Rayleigh defined the peak to trough separation (b/2), that is, the central maximum to adjacent minimum time interval of a diffraction pattern as the limit of resolution. Therefore to resolve two point source objects their separation should be greater than or equal to the peak to trough separation of the diffraction pattern (Figure 4.2).

Now consider the wavelet of Figure 4.1. The peak to trough separation for the wavelet of 30 Hz dominant frequency (α=17765) is given by

$$W = \sqrt{\frac{2}{\alpha}} = \sqrt{\frac{2}{17765}}$$

$$= 10.6 \text{ msecs} \qquad (4.5)$$

Therefore the wavelets should be separated by at least 10.6 msec in order to identify them as two distinct features. For frequencies of 100 Hz and 200 Hz, the peak to trough separations are 3.18 msec and 1.59 msec respectively. For a velocity of 2400 m/sec the difference in raypaths should be 25.4 m for 30 Hz, 7.6 m for 100 Hz and 3.8 m for 200 Hz. Figure 4.3 presents the composite of two pulses for a separation of 10.6 msec and it clearly shows the presence of two separate events. Thus Rayleigh's limit of resolution for an antisymmetric wavelet is also equal to peak to trough separation.

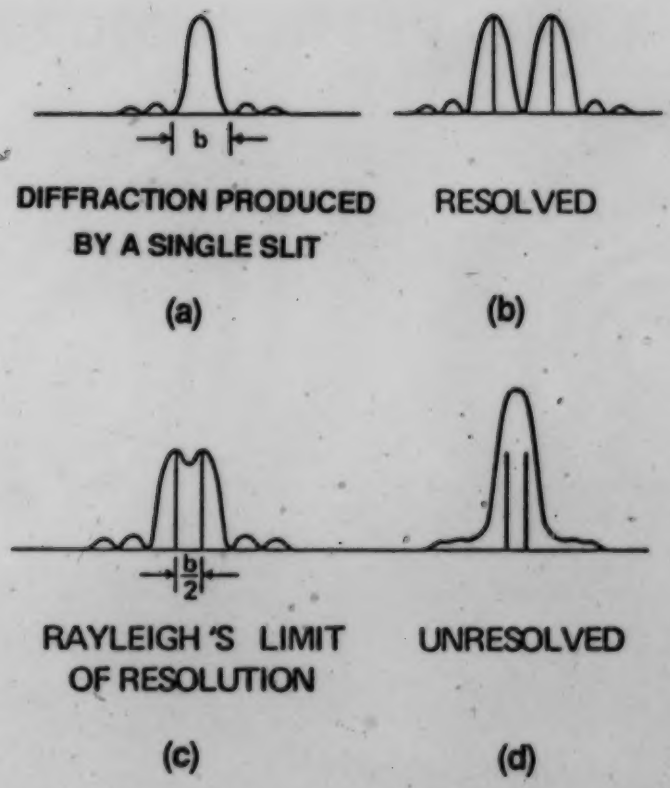

Figure 4.2 Rayleigh's criterion for resolution (a) diffraction pattern produced by a single slit (b) Resolved diffraction pattern from two slits (c) Rayleigh's limit of resolution for two slits (d) unresolved diffraction pattern from two slits.

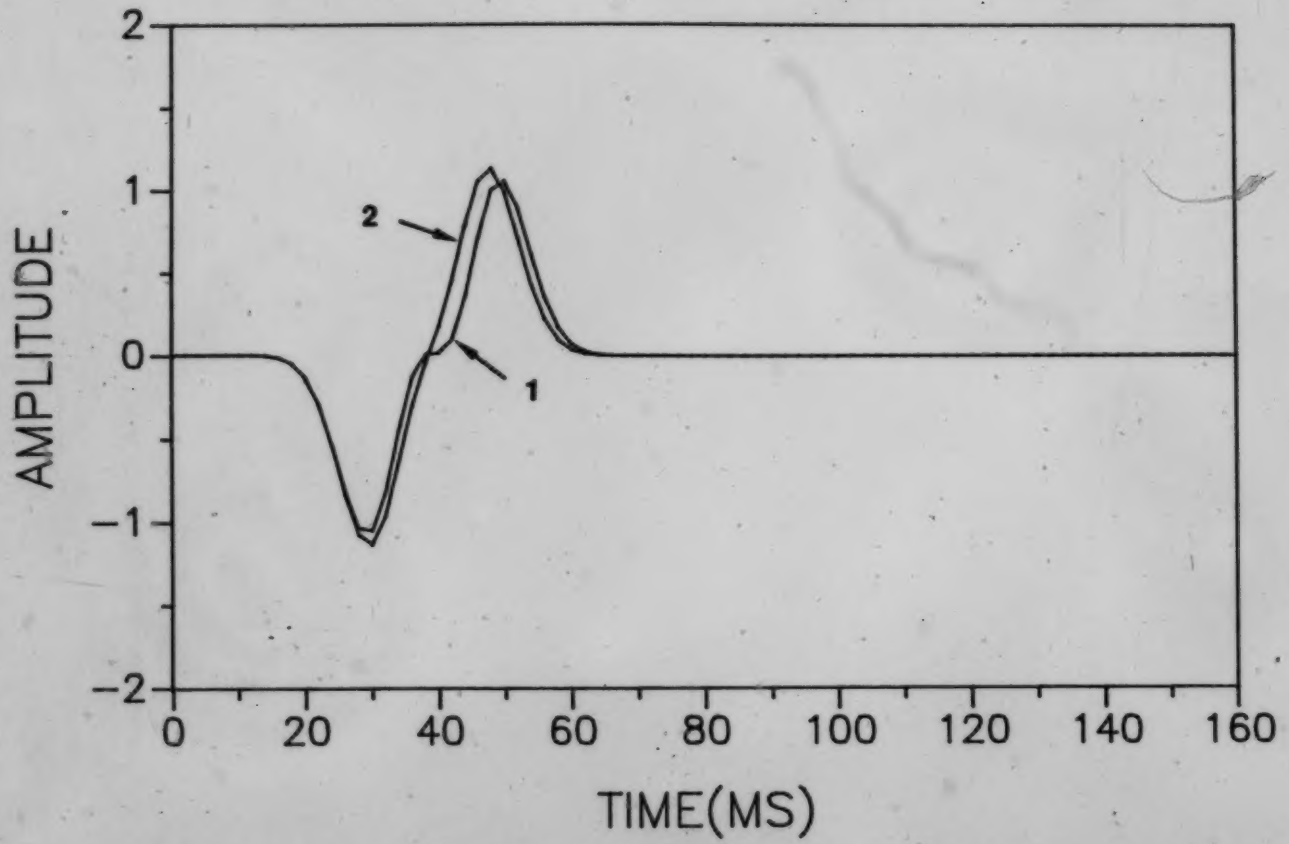

Figure 4.3 A comparison of Rayleigh's and Ricker's criterion of resolution for an antisymmetric wavelet. 1. Rayleigh's limit of resolution 2. Ricker's limit of resolution.

Ricker's Criterion

By studying the composite of two symmetric zero-phase wavelets as a function of separation, Ricker (1953) found that the central maxima get closer and the amplitudes decrease as separations decrease, merging finally into one single major peak. Ricker defined the limit of resolution as that separation where the composite waveform has zero curvature at its central maximum, that is, a flat spot (Figure 4.4). This limit can be found mathematically by differentiating the composite waveform twice and equating to zero. For a symmetric zero-phase wavelet this condition occurs when the separation is equal to the separation of inflection points on the central maximum.

Now let us apply this principle to the antisymmetric wavelet of Figure 4.1. The composite of two wavelets separated by a time duration T is given by

$$C(t) = W(t) + W(t+T) \tag{4.6}$$

where

$$W(t) = t \exp(-\alpha t^2)$$

The flat spot is obtained by setting the second derivative with respect to time equal to zero and evaluating it at the origin i.e.

$$\begin{aligned} C''(t)\big|_{t=0} &= W''(t) + W''(t+T)\big|_{t=0} \\ &= 0 \end{aligned} \tag{4.7}$$

This gives

$$T = \sqrt{\frac{3}{2\alpha}} \tag{4.8}$$

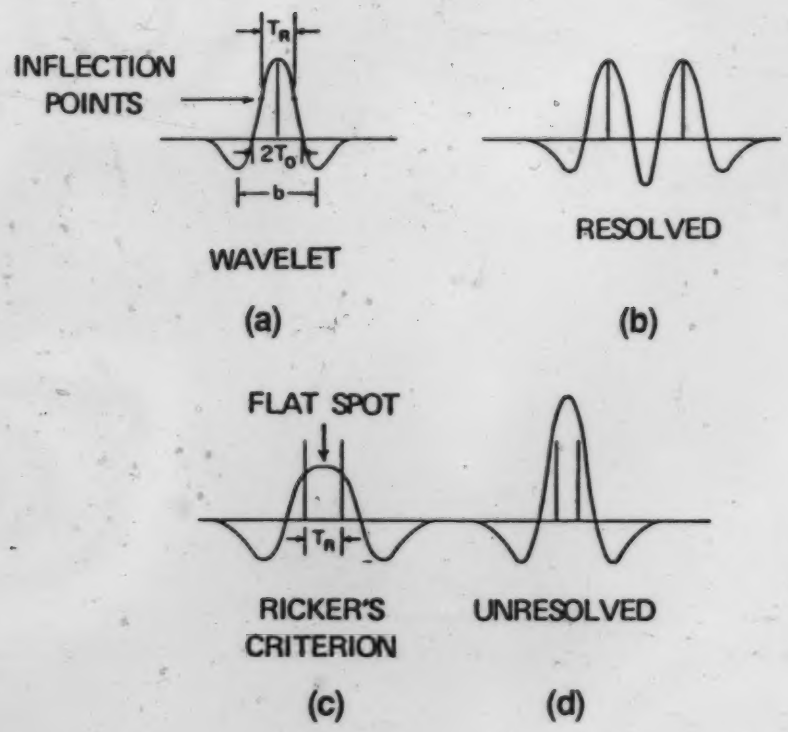

Figure 4.4 Ricker's criterion for resolution. (a) a symmetric Ricker's wavelet (the second derivative of a Gaussian function) (b) two resolved wavelets (c) Ricker's limit of resolution (d) two unresolved wavelets.

For a 30 Hz dominant frequency T=9.2 msec. This limit is less than Rayleigh's limit of resolution. Figure 4.3 also compares the composite wavelets for the separations of 9.2 msec and 10.6 msec. One cannot detect the presence of two wavelets for a separation equal to Ricker's limit, while for a separation equal to Rayleigh's limit one can easily identify two wavelets. Thus, for an antisymmetric wavelet, Rayleigh's criterion is better than Ricker's.

Widess Criterion

Widess (1973) described the criterion for the limit of resolution for the composite of two symmetric zero-phase wavelets of opposite polarities. He observed that as the separation decreases, at one point the composite of two wavelets of opposite polarity approximates the derivative of the wavelet. For a symmetric wavelet this limit occurs when the separation is 1/8 of the wavelength corresponding to the predominant frequency. However in actual practice, because of the presence of noise, the limit is higher.

For the antisymmetric wavelet considered here the composite of two wavelets of opposite polarity approximates the derivative when the time separation is equal to 9.2 msec (Figure 4.5). Thus, in this case the resolution limit can also be obtained from the second derivative (see Ricker's criterion). This was also pointed out by Kallweit and Wood (1982).

In conclusion, we see that the Rayleigh's, Ricker's, and Widess criterion can also be applied to antisymmetric wavelets.

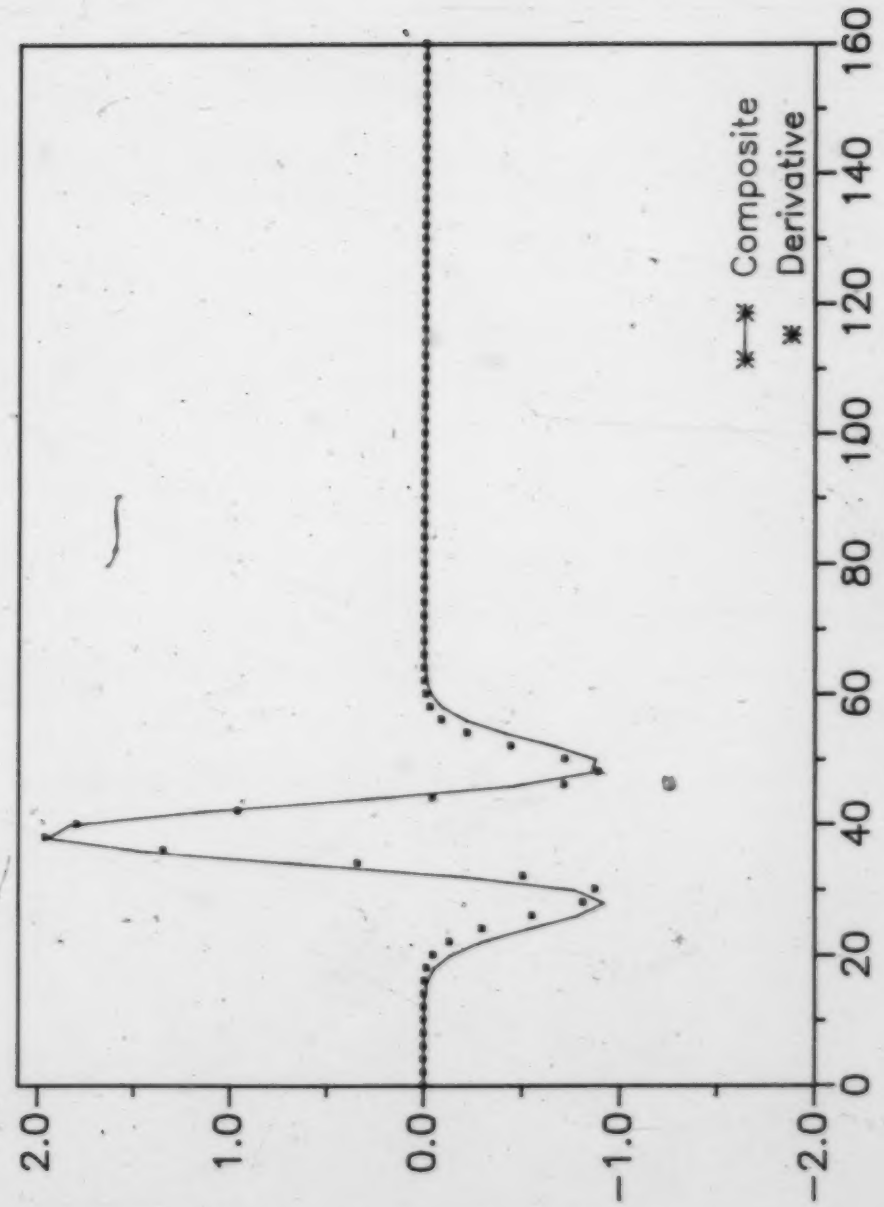

Figure 4.5 Widess criterion applied to an antisymmetric wavelet.

4.3.2 Discussion on Resolution Criterion

In this section an assessment of the above resolution criteria is made by plotting the composite of two wavelets as a function of separation, first for the wavelets of the same polarity followed by the wavelets of opposite polarity. Figure 4.6 shows the composite of two wavelets of the same polarity plotted as a function of separation. Figure 4.7a shows the maximum absolute amplitude of the composite wavelet plotted as a function of separation. The amplitude of the composite monotonically decreases with the separation. For a separation of 10 msec on Figure 4.6, one can easily identify the presence of two separate features. This is also shown in Figure 4.3. Although for the Ricker's criterion it is not as obvious as for Rayleigh's criterion (Figure 4.3).

Figure 4.8 illustrates the composite of two wavelets of opposite polarity plotted as a function of separation, while Figure 4.7b shows the maximum absolute amplitude plotted as a function of separation. In this case the amplitude is maximum for a separation of about 10.6 msec which is the Rayleigh's criterion. But the derivative of the wavelet approximates the composite for a separation of 9.6 msec (Figure 4.5). Thus Widess criterion seems to work in this case. This is not quite so evident on Figure 4.8.

Therefore we can conclude that for two antisymmetric wavelets of the same polarity, Rayleigh's criterion works better than the Ricker's criterion, whereas for two antisymmetric wavelets of opposite polarity, the Widess criterion applies.

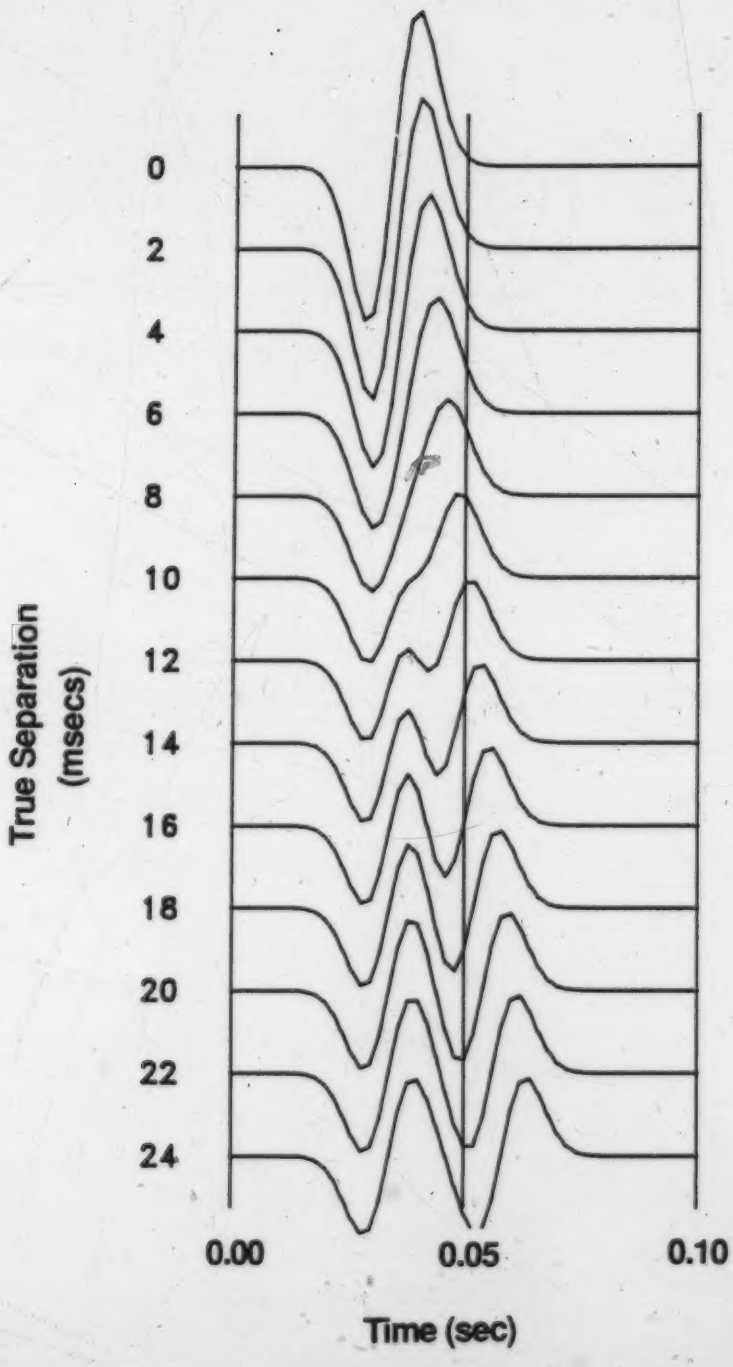

Figure 4.6 Composite of two wavelets of same polarity plotted as a function of separation.

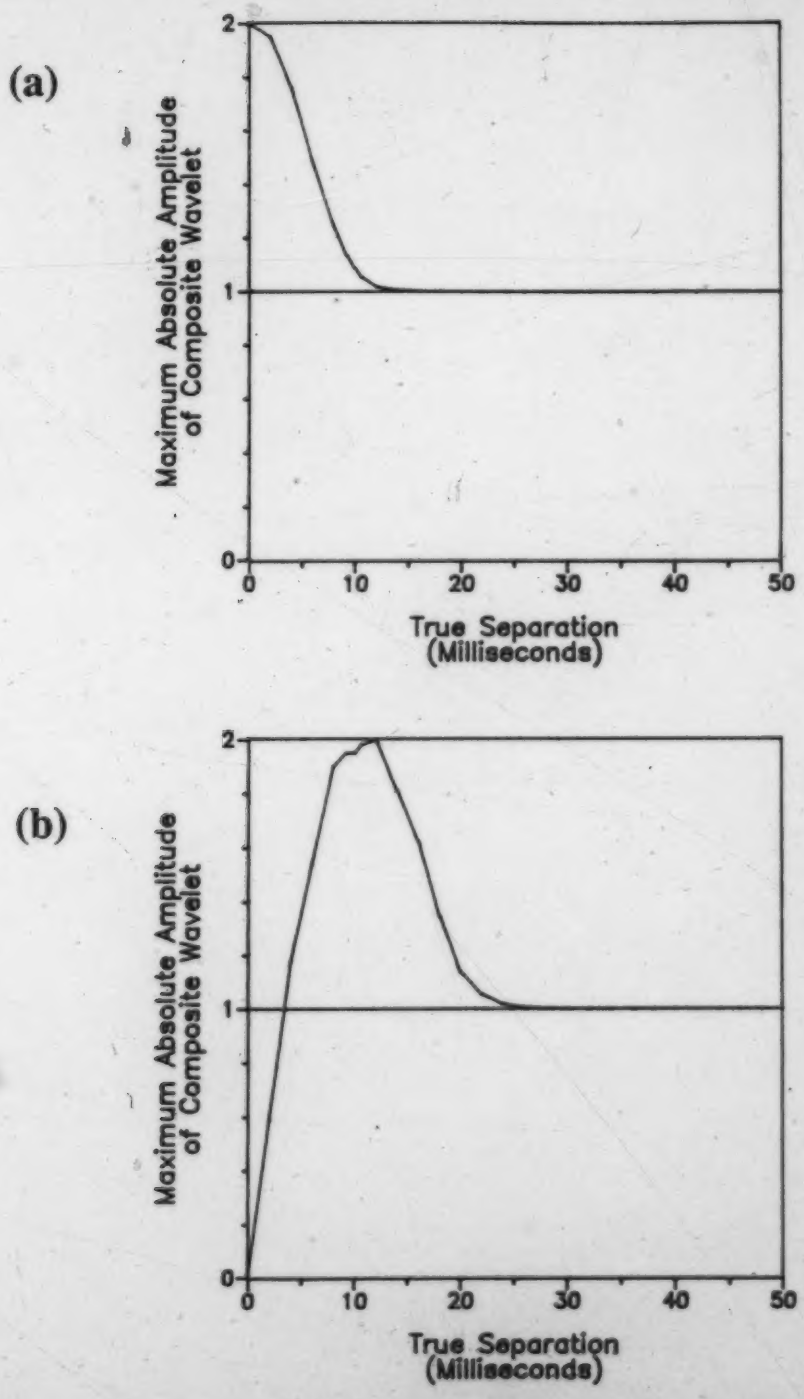

Figure 4.7 (a) The maximum absolute amplitude of the composite of two wavelets of same polarity plotted as a function of separation. (b) The maximum absolute amplitude of the composite of two wavelets of opposite polarity plotted as a function of separation.

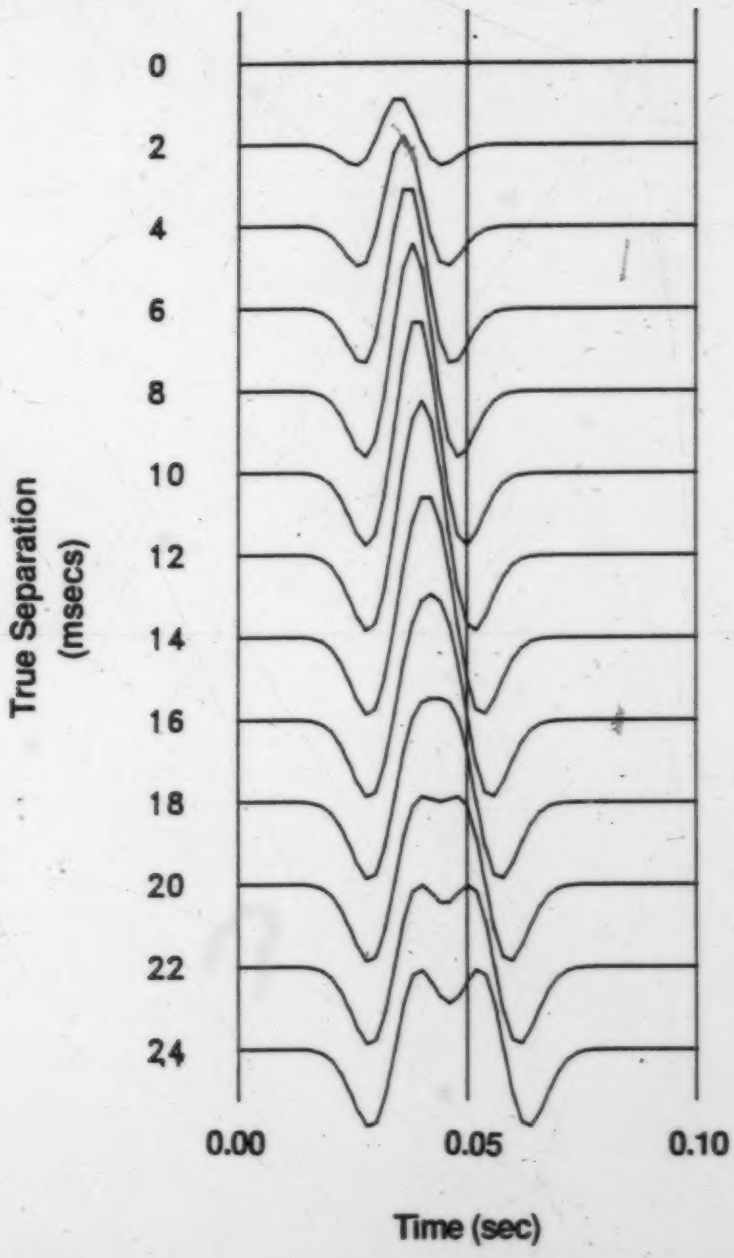

Figure 4.8 Composite of two wavelets of opposite polarity plotted as a function of separation.

4.3.3 Vertical Resolution

To demonstrate how the method works in practice and also to determine the vertical resolution of the method, synthetic records for a step fault model were generated. Figure 4.9 shows the geometry of the step fault model. The fault is located beneath surface location 20 and Δz indicates the throw of the step fault. The velocities in the upper and lower media are 2400 m/s and 3000 m/s respectively. The receiver spacing for generating synthetic data is 50 m. For the antisymmetric seismic pulse used (dominant frequency 30 Hz) the dominant wavelength is 80 m (for a velocity of 2400 m/s). Therefore theoretically speaking, on a CFP section the vertical limits of resolution according to Rayleigh's, Ricker's and Widess' criteria are $\lambda/6.29$, $\lambda/7.25$ and $\lambda/7.25$ respectively. Now let us see if these definitions apply to the vertical fault model.

We begin with the value of Δz equal to the dominant wavelength (λ) of the seismic pulse. The corresponding CDP stacked section and CFP stacked section are shown in Figure 4.10a. In this case the diffracted waves from the edges of two flat reflectors on either side of the fault are two separate events (Figure 4.10a). Accordingly, on the corresponding CFP stacked section two distinct regions with high amplitudes are visible. Also note the change in phase of these two events. This is because they are on opposite sides of the fault plane.

For $\Delta z=\lambda/2$ the two diffracted events have started merging on the CDP stacked section (figure 4.10b). On CFP section (Figure 4.10b) one can still identify them as two separate diffracted events.

For $\Delta z=\lambda/4$ it is really hard to identify them as two separate events (Figure 4.10c) but on CFP stacked section the region of high amplitude indicates that there is a discontinuity in the reflector at that location. Also they are resolved according to the Widess criterion. This discontinuity is also evident on the CDP stacked section. For $\Delta z=\lambda/16$ one cannot see any discontinuity in the reflecting horizon on the CDP stacked section, although one can still

discover its presence by crosscorrelating the traces if the data is acquired at a small sampling interval. However, on the CFP stacked section the discontinuity is indicated by the high amplitude (Figure 4.10d). Thus, in such a case the CFP section helps in interpretation. For $\Delta z<\lambda/16$ the amplitude on the CFP section is very small.

One other difference between an NMO stack and a CFP stack is in the number of traces used to produce a single trace on these sections. Since a trace on the CFP section is obtained by summing a large number of traces, the fold is very high. For the synthetic data considered here the highest fold on an NMO stack is 13, whereas on a CFP section it is 133.

Figure 4.11 illustrates how the peak amplitude on the CFP section varies with $\Delta z/\lambda$. The amplitudes are relative to the amplitude for $\Delta z/\lambda=1/4$. For $\Delta z/\lambda<1/16$ this amplitude will be very small and it will be hard to identify it on CFP section against the background noise. The variation in peak amplitude is similar to that shown in Figure 4.7b. Considering a step fault model is in fact equivalent to considering two seismic pulses of opposite polarity. The theoretically predicted limit of vertical resolution is equal to $\lambda/7.25$. But from the results illustrated in Figure 4.10 the limit of vertical resolution for the CFP method using an array of receivers is approximately equal to $\lambda/16$ which is about half of the theoretical value for a single detector. Thus CFP method gives better vertical resolution than the limits described in section 4.3.1.

Figure 4.12 illustrates how the amplitude on the CFP stacked section varies laterally for different values of Δz. The amplitudes are normalized with respect to the maximum amplitude. The nature of amplitude drop is the same for all values of Δz. Therefore, this data does not allow us to make any inferences regarding the relationship between the amplitude drop and fault throw.

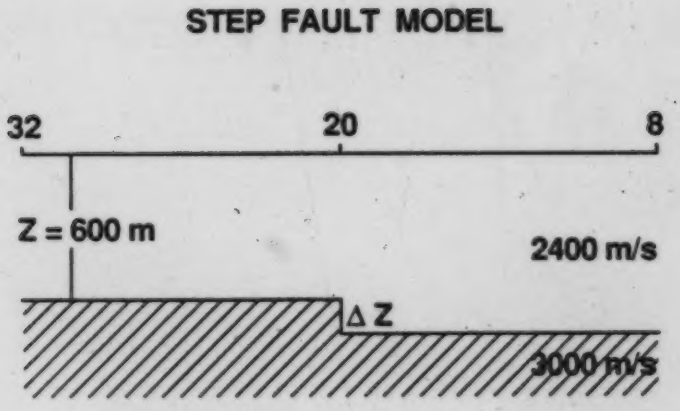

Figure 4.9 Geometry of the step fault model.

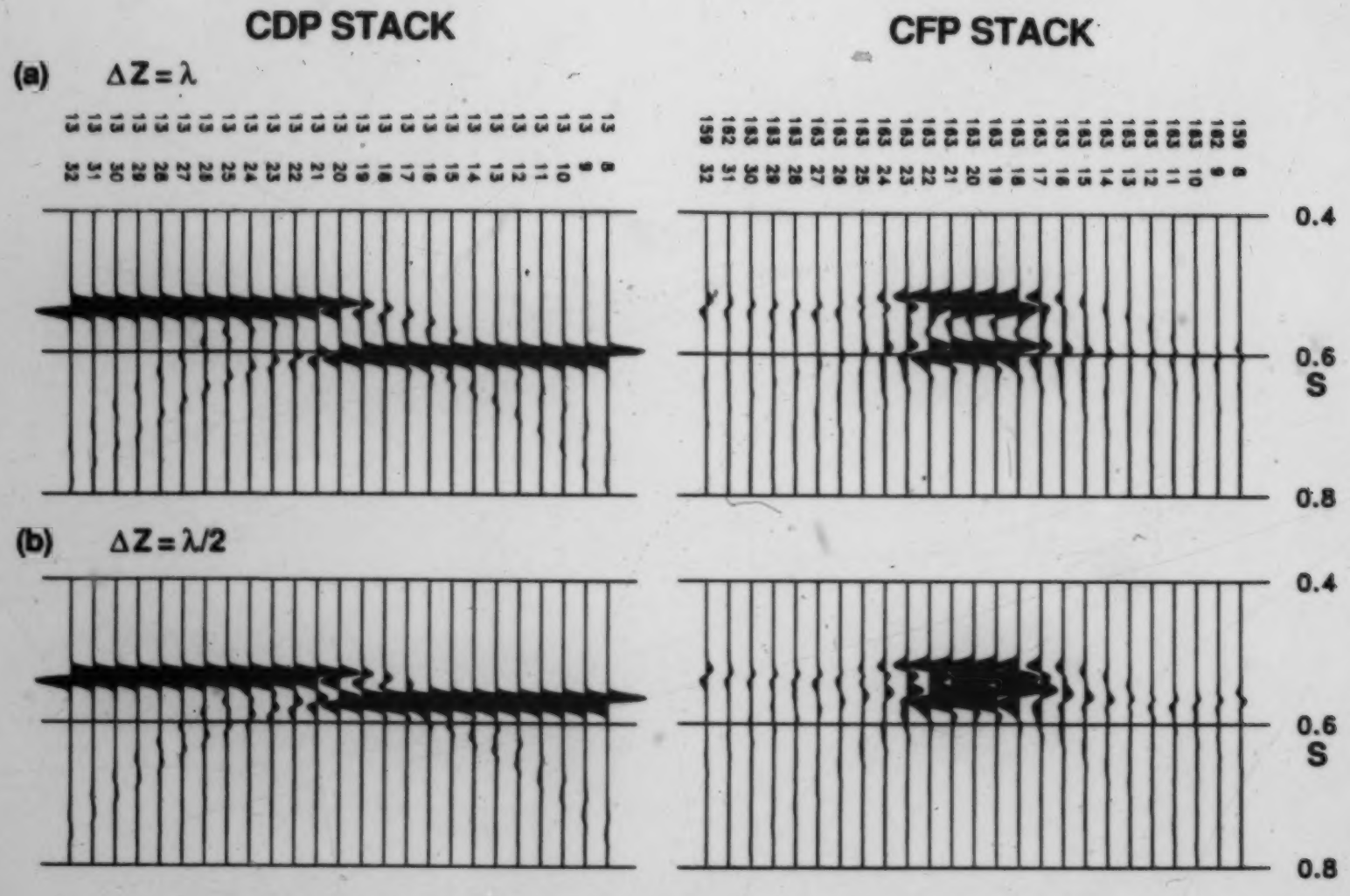

Figure 4.10 (a and b) CDP and CFP stacked sections of the step fault model for (a) $\Delta z=\lambda$ (b) $\Delta z=\lambda/2$.

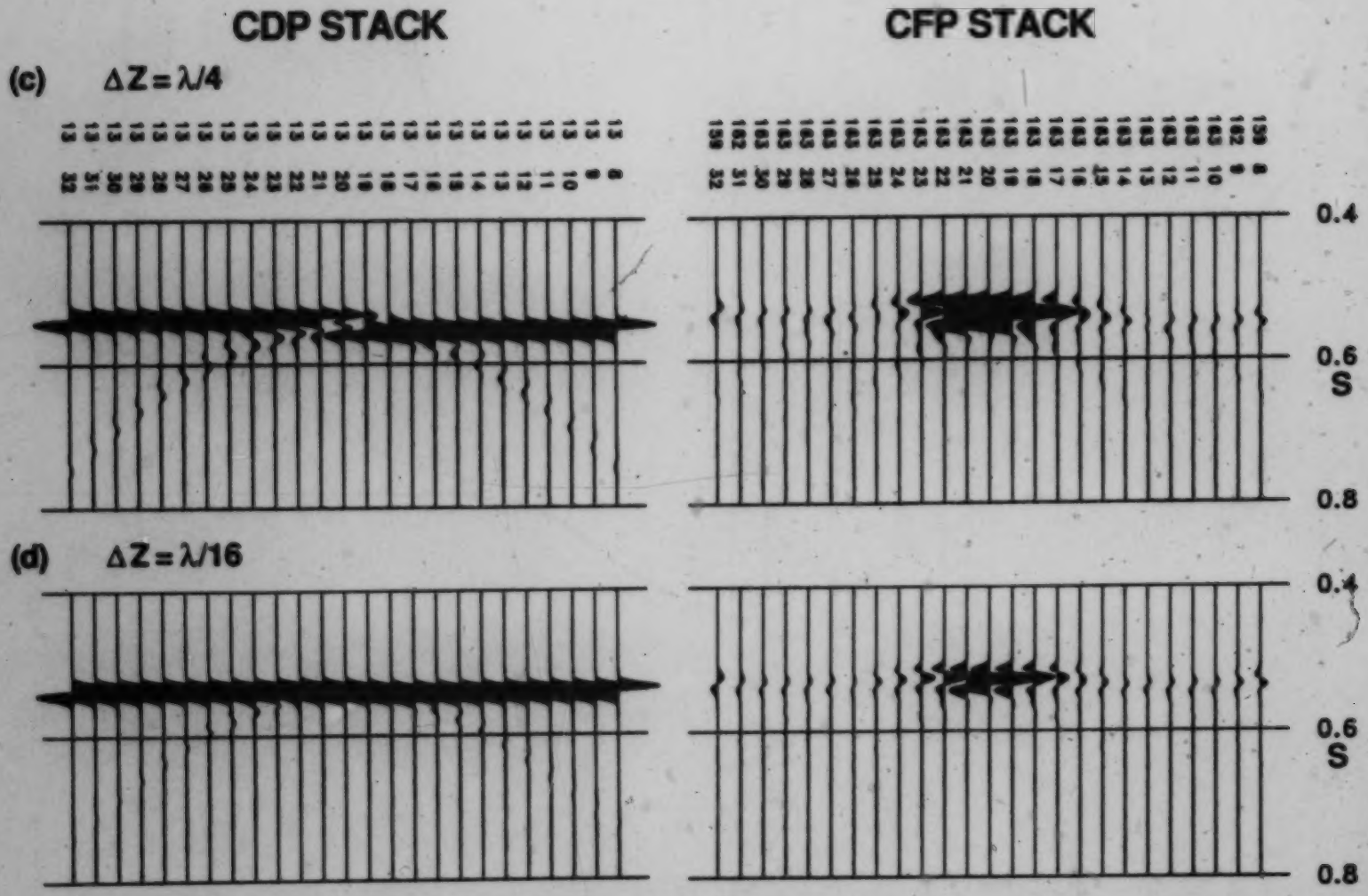

Figure 4.10 (c and d) CDP and CFP stacked sections of the step fault model for (a) Δz=λ/4 (b) Δz=λ/16.

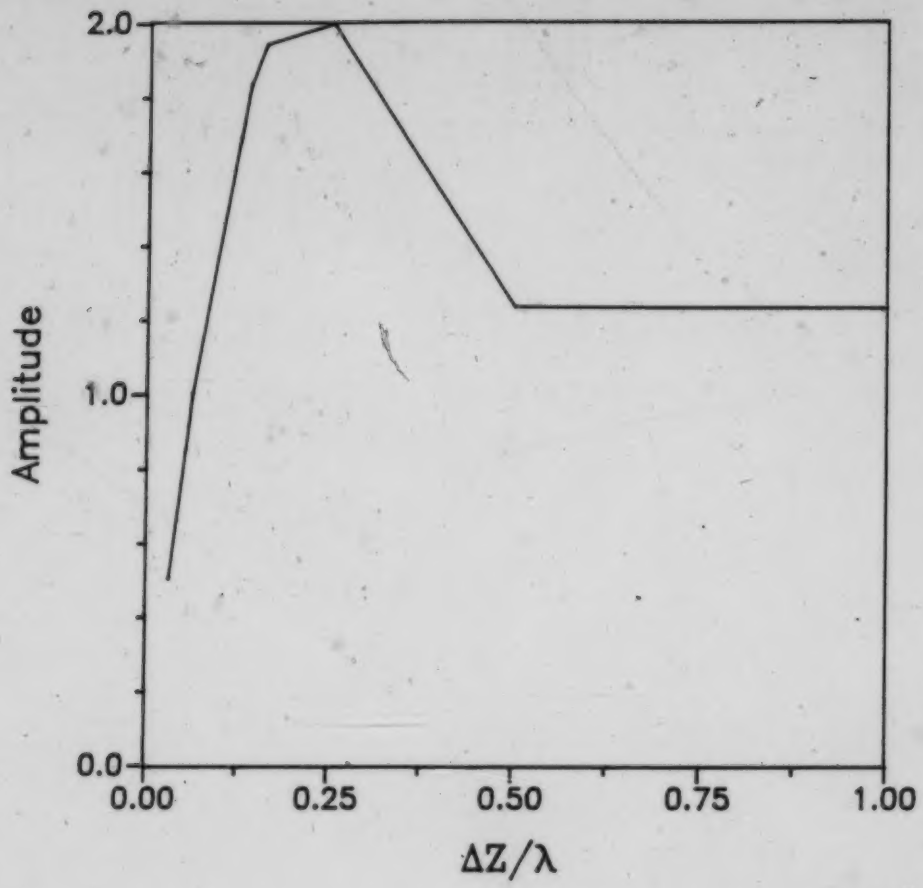

Figure 4.11 Variation of the peak amplitude on the CFP section plotted as a function of $\Delta z/\lambda$.

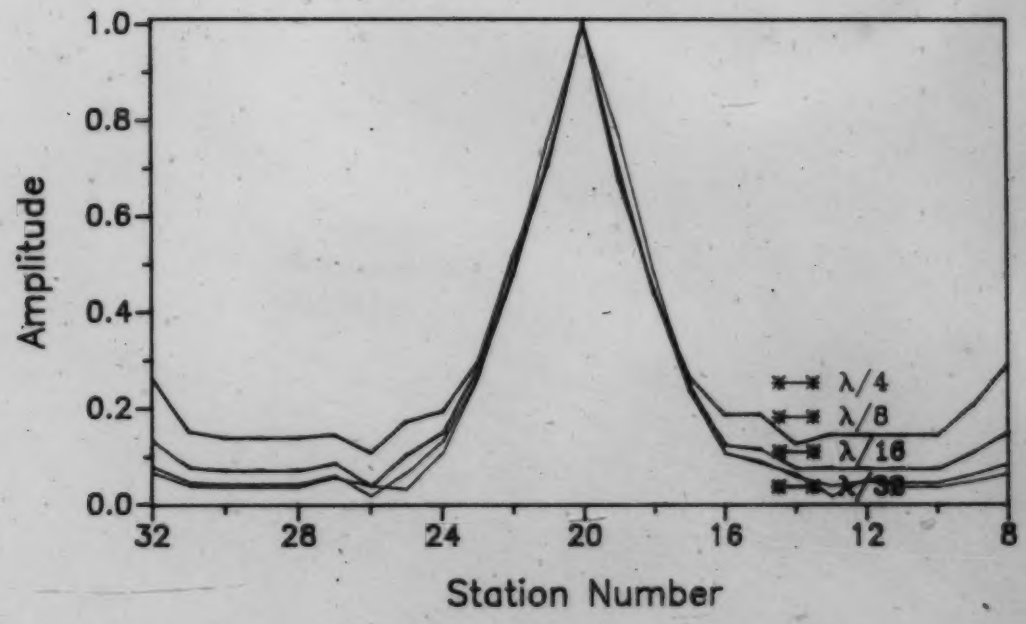

Figure 4.12 Amplitude on CFP section for step fault model plotted as a function of horizontal distance.

4.3.4 Lateral Resolution

The reflected energy seen on a seismic trace is not caused just by a point of the subsurface, but rather an area of the reflector is involved in producing the recorded wave. This area is equal to the first Fresnel zone. A reflection from a plane reflector is one-half of the response of the first Fresnel zone. The first Fresnel zone is the area on the reflector from which reflected energy can reach a detector within the first half cycle of the reflection. The concept of an area rather than a point on the reflector being involved in reflection is the essence of understanding spatial resolution.

Since wavelength depends on frequency, the extent of the Fresnel zone depends on frequency (Figure 4.13). Hence different portions of the reflector are effective for the different frequency components which together make up the seismic waveform. The area of the first Fresnel zone for spherical waves is (Sheriff 1980)

$$R = \frac{V}{2}\sqrt{\frac{t}{f}} \tag{4.9}$$

where R is the radius of the Fresnel zone, V is the velocity above the reflector, t is the two-way travel time and f is the frequency. For a frequency of 30 Hz, two-way travel time of 0.5 sec and velocity of 2400 m/s, the radius of the Fresnel zone is 155 m. Thus the size of the Fresnel zone increases with depth and therefore a deeper feature has to be larger in areal extent to produce the same effect as a smaller shallow feature.

The change in waveshape produced by an edge of a reflector can be explained by considering Fresnel zones (Sheriff 1977). Consider the model of the edge of a reflector (Figure 4.14). When the observation point is away from the edge, all the frequency components contribute in a normal way (Figure 4.14). As the observation point approaches the edge the low frequency components see the edge earlier to high frequency components because the size of the Fresnel zone for low frequency is bigger than that for high frequencies. Therefore a small amount of low frequency components arrive at the detector

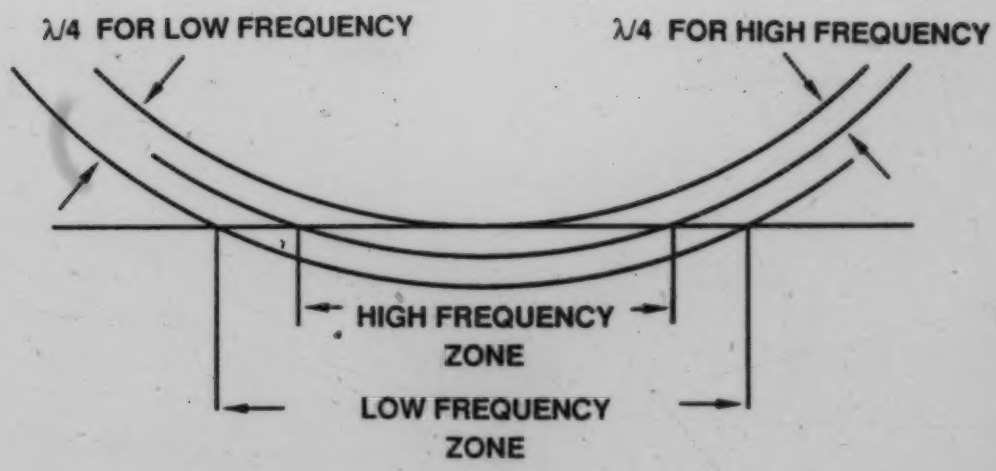

Figure 4.13 Relationship between the extent of the Fresnel zone and frequency.

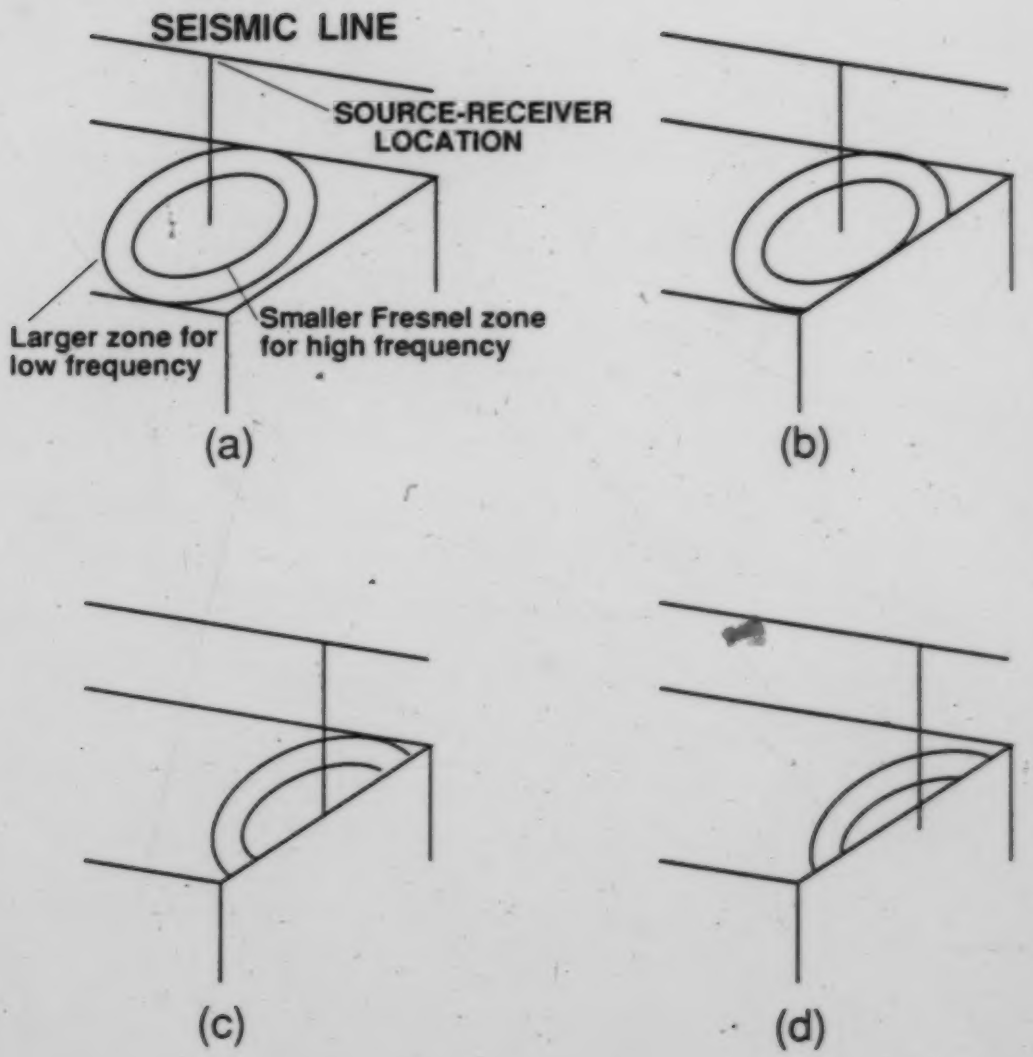

Figure 4.14 Fresnel zone explanation for changes in waveshape produced by the edge of a feature.

changing the waveshape. For an observation point directly above the edge, Fresnel zones for all the frequencies have half the area they had when remote from the edge, hence the reflection wavelet has half the amplitude. For an observation point beyond the reflector the area of the high frequency zones is smaller compared to that for low frequency zones. Hence the waveshape changes. Therefore the edge of a reflector is seen over a region rather than a point directly above it.

Spatial resolution can also be explained from the viewpoint of diffractions. A diffraction represents the effect of a point in the subsurface. When two points are separated by the Fresnel zone, two points are seen rather than one hence they are resolved. When two points are closer than the size of the Fresnel zone we do get indications of the presence of two points but cannot resolve them.

Now let us determine the horizontal resolution for the CFP method. For this method lateral resolution addresses the question of how far apart two diffraction points should be in order to be seismically visible and identifiable. To test the method consider the model of a dyke (Figure 4.15). The receiver spacing chosen for generating synthetic seismograms is 20 m here. This is because we are interested in looking at small lateral changes. We will see the CDP stacks and CFP stacks of this model for the width of dyke varying from $\lambda/4$ to 2λ (Figure 4.16). For $w=\lambda/4$, on CDP stacked section we only see a point diffractor having hyperbolic characteristics. This is because the width of the dyke is less than the size of the Fresnel zone. But on the CFP stacked section one can see the existence of two point diffractors. Their spatial separation on this section is not the true separation, but still it helps us identify two separate diffracting points. For $w=\lambda/2$ and λ again the CDP stacked section does not give any indication for the presence of two point diffractors, but the CFP stacked section does show two distinct features. But once more the width observed on the CFP section is not the true width. For $w=2\lambda$, both CDP and CFP sections show the presence of two subsurface diffractors. Also in this case the width observed on the CFP

section is the true width, although the width is half the size of the Fresnel zone. Figure 4.17 illustrates the amplitude on the CFP section plotted as a function of horizontal distance. The amplitudes are normalized with respect to the highest amplitudes on each CFP section. This illustrates clearly that for the horizontal separation of half the size of the Fresnel zone one can easily detect, resolve and determine the true separation. But for a spatial separation of less than half the size of the Fresnel zone one can detect and resolve two point diffractors but their true separation is hard to determine. Thus CFP stacking method can detect the presence of two point diffractors even if their horizontal separation is less than Fresnel zone. Therefore the lateral resolvability of CFP method is better than that of CDP method.

4.3.5 Resolution and Recording parameters

Choosing the correct recording parameters is also important in achieving the resolution limits which the CFP stacking method has to offer. The sampling interval and receiver spacing are the two most important parameters which we shall discuss below.

To reconstruct the original wavelet the sampling interval should be such that it has at least two samples for each frequency contained in the wavelet. Since the shape of the wavelet is important for vertical resolution (section 4.3.3), the sampling interval should be small enough for the reconstruction process to be complete. With the modern day recording systems one can obtain sampling intervals down to 1/2 msec and hence all the desired frequencies are properly sampled. Frequencies which are not of interest are removed by filtering. Therefore this parameter is not of great concern in modern seismic surveys.

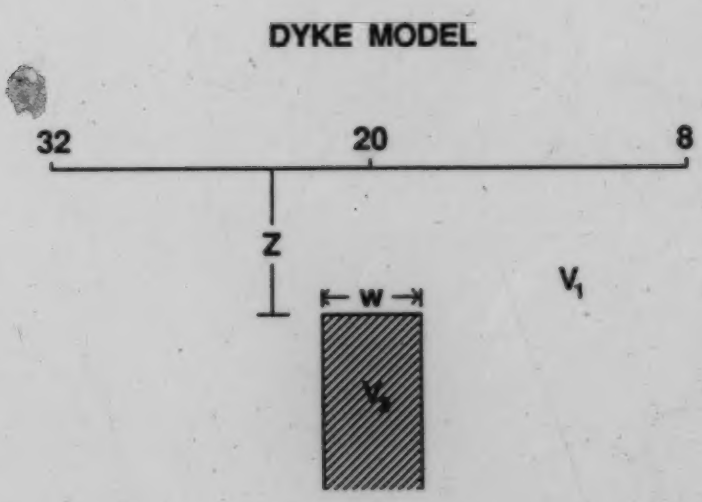

Figure 4.15 The model of a dyke.

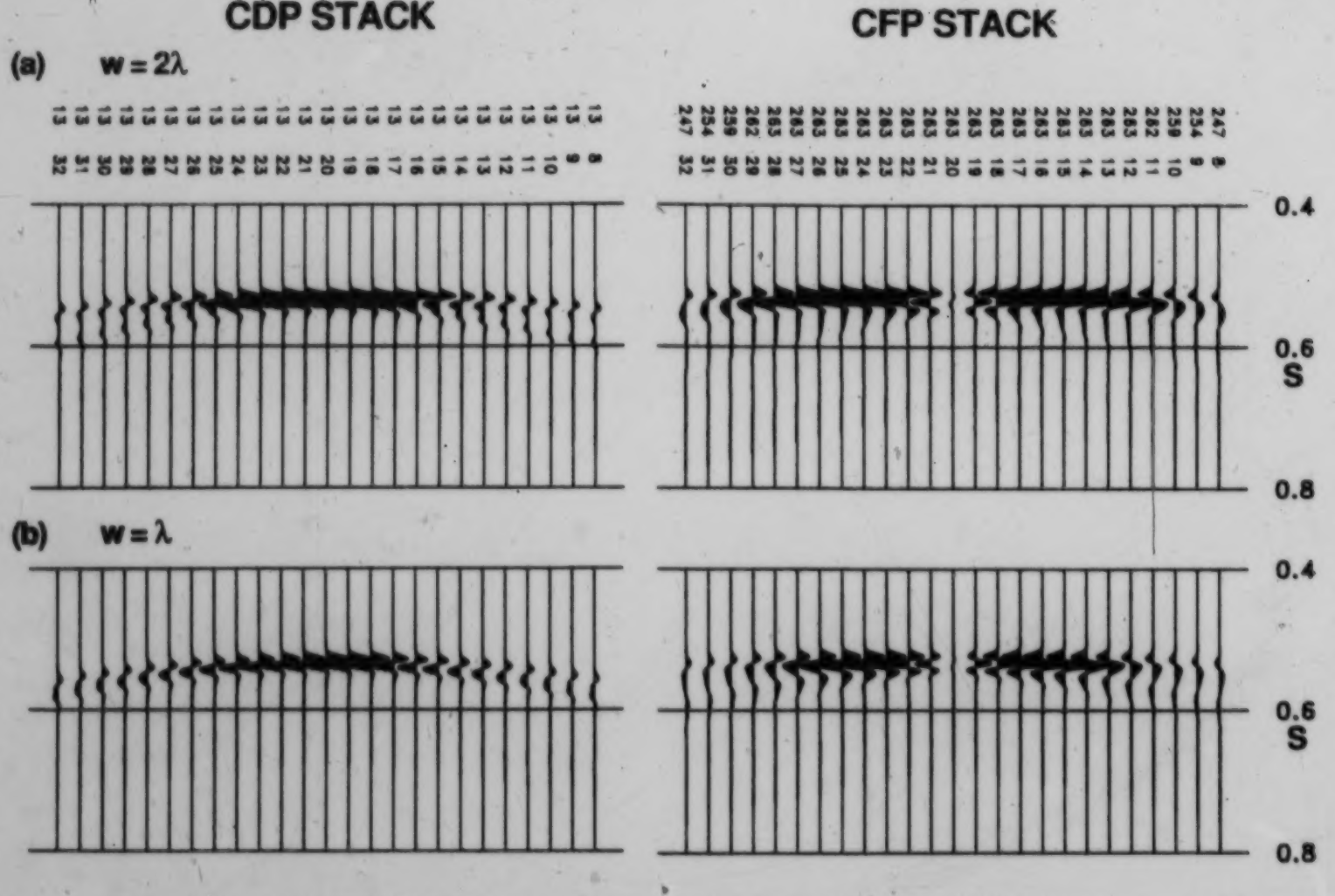

Figure 4.16 (a and b) CDP and CFP stacked sections of the dyke model for widths of (a) 2λ (b) λ.

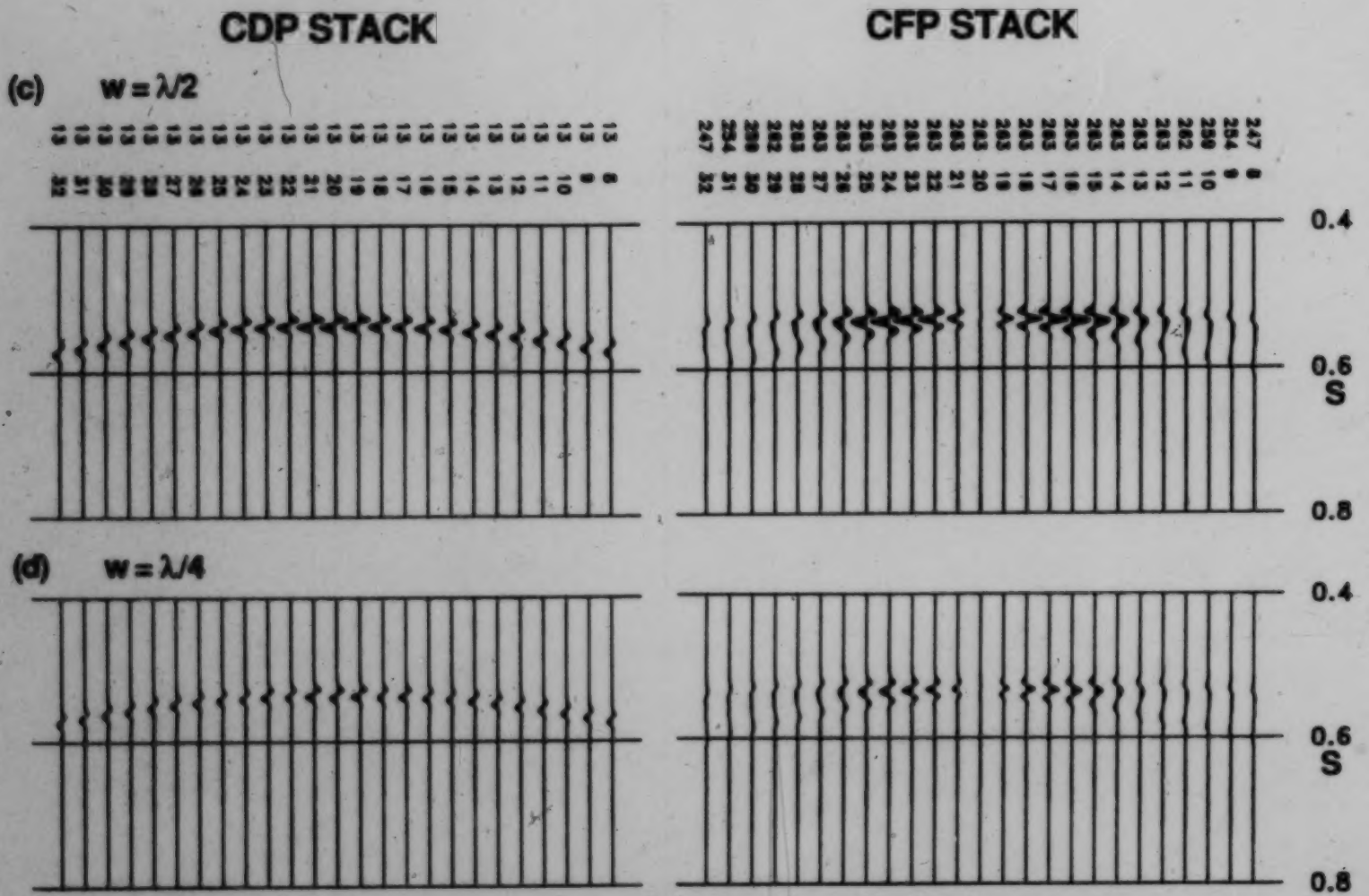

Figure 4.16 (c and d) CDP and CFP stacked sections of the dyke model for widths of (a) λ/2(b) λ/4.

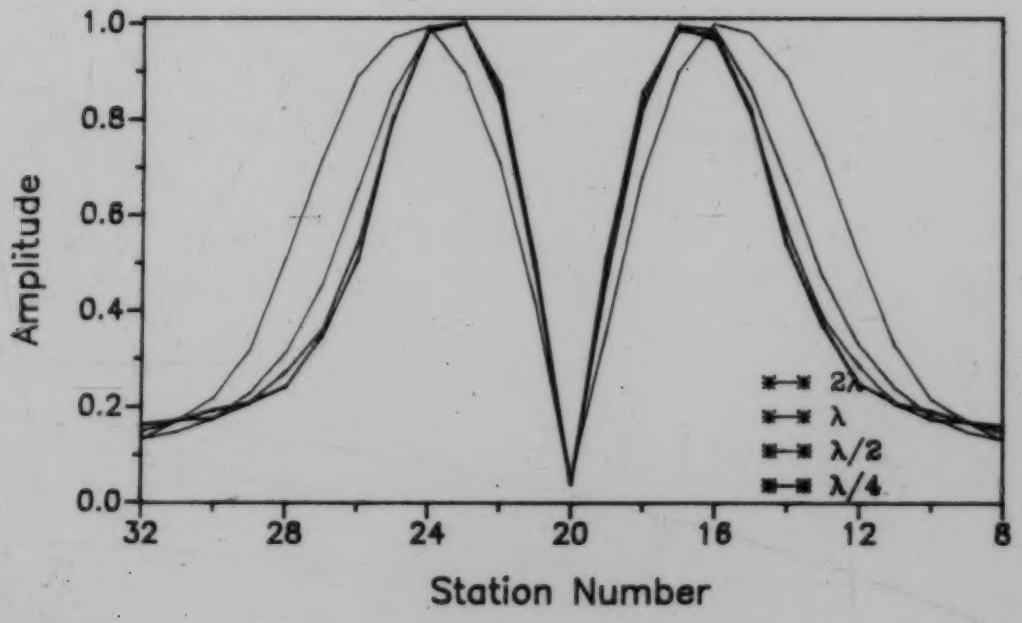

Figure 4.17 Amplitude on CFP section for dyke model plotted as a function of horizontal distance.

Resolution also depends upon the receiver group spacing chosen at the time of recording. To determine small changes in the shape of the wavefronts arriving at the receivers, the receiver group spacing should be as small as possible. These small changes are related to the changes in physical parameters of the subsurface. Receiver group spacing affects lateral resolution more than vertical resolution. To determine the limit on lateral resolution of the CFP method (section 4.3.4) a receiver spacing of 20 m was used, whereas to determine the limit on vertical resolution (section 4.3.3) a receiver spacing of 50 m was used.

4.4 Conclusions

The determination of the vertical and lateral extent of discontinuities is an important aspect in interpreting seismic reflection data. Two coherent wavelets arriving at a receiver location with a time lag are said to be resolved if the time lag is greater than or equal to the resolution criteria of Rayleigh, Ricker or Widess. These criteria are applicable to both symmetric and antisymmetric wavelets.

Source signature, subsurface velocities and the depth of the discontinuity are the most important parameters affecting the resolution. These parameters control the dominant wavelength in the source pulse and the size of the Fresnel zone. The size of the Fresnel zone increases with depth. Any band-limited wavelet with a finite time duration can be used for a source pulse.

The success of the method also depends upon having coherent sources to generate seismic data. For synthetic model studies carried out here this is not a problem. For the real data, the prestack seismograms can be corrected for the lack of coherency during processing, for instance by deconvolution into a zero phase wavelet.

The limits of vertical and lateral resolution were determined by using a step fault and

dyke model respectively. The lateral resolution depends upon the size of the Fresnel zone. The lateral resolvability of the CFP method is better than that of the CDP method, since the CFP method can detect the presence of two point diffractors even if their horizontal separation is less than the size of the Fresnel zone. However a numerical evaluation of the distance between the point diffractors can be carried out only if their separation is greater than or equal to the size of the Fresnel zone. The vertical resolution of the CFP method using an array of receivers is found to be of the order of $\lambda/16$ which is half of the theoretically predicted value for a single source and receiver.

CHAPTER 5
CONCLUSIONS

A tomographic method has been developed to determine the three-dimensional structure and velocity gradients from seismic reflection traveltime data. As a part of the tomographic imaging algorithm, a forward modeling technique was developed to accommodate vertical velocity gradients. The interfaces separating geological media with different physical parameters were modelled by polynomial surfaces. Interfaces with other mathematical expressions, e.g. Fourier series, splines etc., can be easily incorporated in the forward modeling algorithm. The velocity in each layer was either a constant or a linear function of depth. Taking more complicated functions of velocity only complicates the algebra involved but is otherwise straightforward. The forward problem of determining traveltimes for specified source-receiver locations (ray tracing) was solved by the bending method and using algorithms for the solution of a set of nonlinear equations. The efficiency of the ray tracing algorithm can be judged from the fact that it takes about 4.5 sec of CPU time on Amdahl 5870 to trace rays for 225 source-receiver pairs.

A computationally stable, damped least-squares iterative method was developed for inversion. The inversion for third layer with synthetic data required about 9.0 sec of CPU time. The solution was obtained by minimizing the difference between the observed traveltimes and the traveltimes calculated by assuming an earth model. The model is modified iteratively till the differences in traveltimes were less than a preset threshold. Although the method deals with only one type of wave (P wave), other types of waves and converted phases can also be accommodated in the algorithm. The inversion scheme demonstrates the viability of constructing the three-dimensional structure and velocity model from seismic reflection data.

The inversion process was applied to a small reflection data set from a seismic line on Vancouver Island. A three-dimensional structure and velocity with gradients was obtained for this region by taking advantage of the crookedness of the line. For inversion of reflectors C and E approximately 2.0 sec and 3.8 sec of CPU time was necessary for each iteration. This example shows the effectiveness of the method in producing three-dimensional structures from crooked line surveys. The small set of data limited us to assume plane interfaces. The calculated values of the velocity at the top and velocity gradient for reflector C and E are 6.85 km/s, 0.034 km/s/km and 7.7 km/s, 0.0 km/s/km respectively. These reflectors dip towards the northeast at angles of 3° and 8° respectively. The high velocity values above the reflector E are consistent with refraction models.

Velocity data obtained from inversion was used to migrate reflection data of all four lines and contour maps for the depths of subduction and decollement zones were prepared. Both of these reflectors generally dip towards northeast.

Diffractions are produced by waves intersecting discontinuities in the subsurface acoustic impedance. Therefore the presence of diffraction arcs on seismic sections are indications of these discontinuous features. A new technique, called the Common Fault Point (CFP) technique, has been developed to image such discontinuities in the acoustic impedance. The method uses diffraction hyperbolas observed on prestack traces and concentrates the diffracted energy at the apex. The method exploits the difference between reflection moveout and diffraction moveout. A stacked trace for a surface location is obtained by assuming diffractors to be located beneath that location, applying appropriate moveout and amplitude corrections and summing. A CFP stacked section is obtained by repeating the process for each surface location and discontinuities are displayed by high amplitudes at their true time or depth locations.

The potential of the method is demonstrated by applying it to three seismic data sets. The boundary of a volcanic intrusion into Cambrian formations in the Princess area of

southern Alberta was mapped by CFP method. There are several other high amplitude features on the CFP section whose geological significance is unknown. Extensive modeling studies should be carried out in future to understand these features. The velocity model selected for stacking purpose plays a very important role in the results obtained. CFP stacks with various velocity models should be obtained before making any definite interpretations. The developed method is computationally expensive if many different velocity models are tried and the limitation of computing funds restricted our full experimentation. But modern day supercomputers or array processors make it quite feasible for industrial applications. The method also needs modifications to accommodate complicated velocity models.

A careful interpretation of the seismic data from the Vulcan area of Southern Alberta revealed a midcrustal reflector denoted by C. This reflector was not observed in previous studies. The data also showed the existence of a buried Precambrian rift valley. The consistency of the reflection correlation across this faulted terrane was assessed by making two-dimensional gravity calculations.

Application of CFP method to data from Melville Island clearly identified the boundary between Silurian and Upper Ordovician formations. The diffractions produced by change in facies at this boundary helped in its identification. The outline of the salt unit was also visible on CFP section.

Two coherent wavelets arriving at a receiver location with a time lag are said to be resolved if the time lag is greater than or equal to the resolution criteria of Rayleigh, Ricker or Widess. These criteria are applicable to both symmetric and antisymmetric wavelets.

Source signature, subsurface velocities and the depth of the discontinuity are the most important parameters affecting the resolution. These parameters control the dominant wavelength in the source pulse and the size of the Fresnel zone. The size of the Fresnel zone increases with depth. Any band-limited wavelet with finite a time duration can be used

for a source pulse.

The limits of vertical and lateral resolution were determined by using a step fault and dyke model respectively. The lateral resolution depends upon the size of the Fresnel zone. The lateral resolvability of the CFP method is better than that of the CDP method, since the CFP method can detect the presence of two point diffractors even if their horizontal separation is less than the size of the Fresnel zone. However a numerical evaluation of the distance between the point diffractors can be carried out only if their separation is greater than or equal to the size of the Fresnel zone. The vertical resolution of the CFP method using an array of receivers is found to be of the order of $\lambda/16$ which is half of the theoretically predicted value for a single source and receiver.

REFERENCES

Aki, K., and Lee, W. H. 1976. Determination of Three-dimensional velocity anomalies under a seismic array using first P arrival times from local earthquakes. Journal of Geophysical Research, **81**, 4381-4399.

Aki, K., and Richards, P. G., 1980, Quantitative seismology: Theory and Methods, Volumes I and II, W. H. Freeman and Company, San Francisco.

Backus, G. E., and Gilbert, J. F., 1967, Numerical application of a formalism for geophysical inverse problems, Geophysical Journal, **13**, 247-276.

Backus, G. E., and Gilbert, J. F., 1968, The resolving power of gross-earth data, Geophysical Journal, **16**, 169-205.

Backus, G. E., and Gilbert, J. F., 1970, Uniqueness in the inversion of inaccurate gross-earth data, Philosophical Transactions of the Royal Society of London, **266**, 123-192.

Banioff, H., 1954, Orogenesis and deep crustal structure: additional evidence from seismology: Geological Society of America Bulletin, 65, 385-400.

Bath, M., 1968, Mathematical aspects of seismology, Amsterdam, Elsevier.

Bath, M., 1974, Spectral Analysis in Geophysics: Elsevier Scientific Publishing Company; Amsterdam.

Berryhill, J.R., 1977, Diffraction response for nonzero separation of source and receiver: Geophysics, **42**, 1158-1176.

Bishop, T. N., Bube, K. P., Cutler, R. T., Langan, R. T., Love, P. L., Resnick, J. R., Shuey, R. T., Spindler, D. A., and Wyld, H. W. 1985. Tomographic determination of velocity and depth in laterally varying media. Geophysics, **50**, 903-923.

Chander, R. 1977. On tracing seismic rays with specified end points in layers of constant velocity and plane interfaces. Geophysical Prospecting, **25**, 120-124.

Chiu, S. K. L., Kanasewich, E. R., and Phadke, S. 1986. Three-dimensional determination of structure and velocity by seismic tomography. Geophysics, **51**, 1559-1571.

Chiu, S. K. L., and Stewart, R. R., 1987, Tomographic determination of three-dimensional seismic velocity structure using well-log, vertical seismic profiles and surface seismic data, Geophysics, **52**, 1085-1098.

Clowes, R.M., Kanasewich, E.R., and Cumming, G.L., 1968, Deep crustal seismic reflections at near-vertical incidence: Geophysics, **33**, 441-451.

Clowes, R.M., Ellis, R.M., Hajnal, Z., Jones, I.F., 1983, Seismic reflections from subducting lithosphere: Nature, **303**, 668-670.

Clowes, R. M., Green A. G., Yorath, C. J., Kanasewich, E. R., West, G. F., and Garland, G. D., 1984, Lithoprobe - A national program for studying the third dimension of geology. Journal of the Canadian Society of Exploration Geophysicists, **20**, 23-39.

Clowes, R. M., Brandon, M. T., Green, A. G., Yorath, C. J., Sutherland Brown, A., Kanasewich, E. R., and Spencer, C., 1987, LITHOPROBE - southern Vancouver Island: Cenozoic subduction complex imaged by deep seismic reflections, Canadian Journal of Earth Sciences, **24**, 31-51.

Coney, P. J., 1981, Accretionary tectonics in western North America, in Dickinson, W. R., and Payne, W. D. (eds.), Relations of tectonics to ore deposits in the southern Cordillera, Arizona Geological Society Digest, **15**, 23-37.

Coney, P. J., Siberling, N. J., Jones, D. L., and Richter, D. H., 1981, Structural relations along the leading edge of Wrangellia terrane in the Clearwater Mountains, Alaska, United States Geological Survey Circular 823-B, 56-58.

Cook, F. A., Albaugh, D. S., Brown, L. D., Kaufman, S., Oliver, J. E.,and Hatcher, R. D.,Jr., 1979, Thin-skinned tectonics in the crystalline southern Appalachian; COCORP seismic reflection profiling of the Blue Ridge and Piedmont, Geology, **7**, 563-567.

Cox, A. V., Dalrymple, G. B., and Doell, R. R., 1967, Reversals of the earth's magnetic field, Scientific American, **216**, 44-45.

Cutler, R. T., Bishop, T. N., Wyld, H. W., Shuey, R. T., Kroeger, R. A., Jones, R. C., and Rathbun, M. L., 1984, Seismic tomography formulation and methodology. Presented at the 54th Annual International Meeting, Society of Exploration Geophysicists, Atlanta.

Davis, G. H., 1984, Structural geology of rocks and regions, John Wiley & Sons.

Dix, C.H., 1952, Seismic prospecting for oil: Harper.

Dobrin, M.B., 1976, Introduction to Geophysical Prospecting: McGraw-Hill Book Company.

Draper, N. R., and Smith, H., 1981, Applied regression analysis, 2nd edition, Wiley, New York.

Fowler, J.C. and Waters, K.H., 1975, Deep crustal reflection recordings using "Vibroseis" methods- A feasibility study: Geophysics, **40**, 399-410.

Gazdag, J., 1978, Wave equation migration with the phase shift method, Geophysics, **43**, 1342-1351.

Gjoystdal, H., and Ursin, B. 1981. Inversion of reflection times in three dimensions. Geophysics, **86**, 972-983.

Gjoystdal, H., Reinhardsen, J. E., and Ursin, B. 1984. Traveltime and wavefront curvature calculations in three-dimensional inhomogeneou layered media with curved interfaces. Geophysics, **49**, 1466-1494.

Golub, G. H., and Reinsch, C. 1970. Singular value decomposition and least-squares solution, in Wilkson, J., and Reinsch, C., Eds., Handbook for automatic computation, II, Linear algebra. Springer-Verlag.

Gradshteyn, I. S., and Ryzhik, I. M., 1980, Table of Integrals, Series, and Products, corrected and enlarged edition, Academic Press.

Green, A. G., Clowes, R. M., Yorath, C. J., Spencer, C., Kanasewich, E. R., Brandon, M. T., and Sutherland Brown, A., 1986, Seismic reflection imaging of the subducting Juan de Fuca plate, Nature (London), **319**, 210-213.

Haagedorn, J.G., 1954, A process of seismic reflection interpretation: Geophysical Prospecting, **2**, 85-127.

Hawley, B. W., Zandt, G., and Smith, R. B. 1981. Simultaneous inversion for hypocenters and lateral velocity variations. Journal of Geophysical Research, **86**, 7073-7086.

Hilterman, F.J., 1970, Three-dimensional seismic modeling: Geophysics, **35**, 1020-1037.

Hilterman, F.J., 1975, Amplitudes of seismic waves - A quick look: Geophysics, **40**, 745-762.

Hoerl, A. E., and Kennard, R. W. 1970. Ridge regression: biased estimation for nonorthogonal problem. Technometrics, **12**, 55-67.

Hoerl, A. E., Kennard, R. W., and Baldwin, K. F. 1975. Ridge regression: some simulation. Communication in Statiatics, **4**, 105-123.

Hubral, P., 1975, Locating a diffractor below plane layers of constant interval velocity and varying dip: Geophysics, **23**, 313-322.

Hyndman, R.D., Riddihough, R.P., and Herzer, R., 1979, The Nootka fault zone - new plate boundary off Western Canada: Geophys. J. Roy. Astro. Soc., 58, 667-683.

Isacks, B., Oliver, J., and Sykes, L. R., 1968, Seismology and the new global plate tectonics: Journal of Geophysical Research, 73, 5855-5899.

Jackson, D. D., 1972, Interpretation of inaccurate, insufficient and inconsistent data, Geophysical Journal, **28**, 97-109.

Julian, B. R., and Gubbins, D. 1977. Three-dimensional seismic ray tracing. Journal of Geophysics. **43**, 95-113.

Jupp, D. L. B., and Vozoff, K., 1975, Stable iterative methods for the inversion of geophysical data, Geophysical Journal of Royal Astronomical Society, **42**, 957-976.

Kak, A. C., 1979, Computeerized tomography with X-ray, Emission, and Ultrasound Sources, Proc. IEEE, **67**, 1245-1272.

Kak, A. C., 1981, Guest ed., Computerized Medical Imaging, Special issue of IEEE Trans., Biomed. Eng.

Kallweit, R. S., and Wood, L. C., 1982, The limits of resolution of zero-phase wavelets: Geophysics, **47**, 1035-1046.

Kanasewich, E.R., 1968, Precambrian Rift: Genesis of Strata-Bound Ore Deposits: Science, 161, 1002-1005.

Kanasewich, E. R., 1981, Time sequence analysis in geophysics, 3rd edition, The University of Alberta Press.

Kanasewich, E. R., and Chiu, S. K. 1985. Least-squares inversion of spatial seismic refraction data. Bulletin of Seismological Society of America, **75**, 865-880.

Kanasewich, E.R., and Cumming, G.L., 1965, Near-vertical incidence seismic reflections from the 'Conrad' discontinuity: J. Geophys. Res., 70, 3441-3446.

Kanasewich, E. R., and Phadke, S., 1986, Location of fault edges on seismic sections, Presented at the Canadian Society of Exploration Geophysicists National Convention, May 13th-16th, Calgary, Alberta.

Kanasewich, E. R., and Phadke, S. M., 1988, Imaging discontinuities on seismic sections, Geophysics, **53**,

Keen, C.E., and Hyndman, R.D., 1979, Geophysical review of the continental margins of eastern and western Canada: Can. J. Earth Sci., 16, 712-747.

Koefoed, O., 1981, Aspects of vertical seismic resolution: Geophys. Prosp., **29**, 21-30.

Krey, T., 1952, The significance of diffraction in the investigation of faults: Geophysics, **17**, 843-858.

Kunz, B.F.J., 1960, Diffraction problems in fault interpretation: Geophys. Prosp., **8**, 381-388.

Lanczos, C., 1961, Linear differential operators, Van Nostrand, Princeton, 665-679.

Landa, E., Shtivelman, V., and Gelchinsky, B., 1987, A method for detection of

diffracted waves on common-offset sections: Geophys. Pros., **35**, 359-373.

Lawson, C. L., and Hanson, R. J., 1974, Solving least-squares problems, Prentice- Hall, Engle-wood cliffs, New Jersy.

Levenberg, K. 1944. A method for the solution of certain nonlinear problems in least squares. Quarterly of Applied Mathematics. **2**, 164-168.

Lines, L. R., and Treital, S., 1984, Tutorial: A review of least-squares inversion and its application to geophysical problems, Geophysical Prospecting, **32**, 159-186.

Longhurst, R. S., 1967, 2nd edition, Geometrical and physical optics, London, Longman Green and Co.

Margenau, H., and Murphy, G. M., 1956, The mathematics of physics and chemistry, Princeton, Van Nostrand Co. Inc.

Marquardt, D. W. 1963. An algorithm for least-squares estimation of nonlinear parameters. Journal of Society of Industrial Applied Mathematics. **11**, 55-67.

McMechan, G. A., 1983, Seismic tomography in boreholes, Geophysical Journal of Royal Astronomical Society, **74**, 601-612.

McMechan, G. A., and Spence, G. D., 1983, P-wave velocity structure of the earth's crust beneath Vancouver Island, Can. J. Earth Sci., **20**, 742-752.

Menke, W., 1984, Geophysical data analysis: Discrete inverse theory, Academic Press Inc. Monger, J.W.H., and Price, R.A., 1979, Geodynamic evolution of Canadian Cordillera - progress and problems: Can. J. Earth Sci., **16**, 770-791.

Nafe, J. E., and Drake, C. L., 1963, Physical properties of marine sediments, in The Sea, 3, 794-815, ed. Hill, M. N., Wiley, New York.

Norton, S. J., and Linzer, M., 1979, Ultrasonoc reflectivity tomography: reconstruction with circular transducer arrays, Ultra. Imaging, **1**, 154-184.

Oliver, J., Cook, F., and Brown, L., 1983, COCORP and the continental crust: J. Geophys. Res., 88, 3329-3347.

Phadke, S., and Kanasewich, E. R., 1987, Seismic tomography for obtaining velocity gradients and 3D structure, Paper presented at the Canadian Society of Exploration Geophysicists National Convention, May 12-14, Calgary, Alberta, Canada.

Phadke, S. M., and Kanasewich, E. R., 1987, Imaging discontinuities on seismic sections, Paper presented at the Society of Exploration Geophysicists Fifty-seventh Annual International Meeting and Exposition, New Orleans, U.S.A.

Powell, M. J. 1970. A hybrid method for nonlinear equations, in Rabinowitz, P., Ed.,Numerical methods for nonlinear algebraic equations. Gordon and Breach Inc.

Ricker, N., 1953, Wavelet contraction, wavelet expansion and the control of seismic resolution: Geophysics, **18**, 769-792.

Riddihough, R. P., 1977, A model for recent plate interactions off Canada's west coast, Canadian Journal of Earth Sciences, **14**, 384-396.

Riddihough, R.P., 1978, The Juan de Fuca plate, Transactions: Amer. Geophys. Union, 59, 836-842.

Schilt, S., Oliver, J., Brown, L., Kaufman, S., Albaugh, D., Brewer, J., Cook, F., Jensen, L., Krumhansl, P., Long, G., and Steiner, D., 1979, The hetrogeneity of the continental crust: Results from deep crustal seismic reflection profiling using the Vibroseis technique: Rev. Geophys. Space Phys., **17**, 354-368.

Schilt, F.S., Kaufman, S., and Long, G.H., 1981, A three-dimensional study of seismic diffraction patterns from deep basement sources: Geophysics, **46**, 1673-1683.

Schoenberger, M., 1974, Resolution comparison of minimum-phase and zero-phase signals: Geophysics, **39**, 826-833.

Sheriff, R. E., 1977, Limitations on resolution of seismic reflections and geologic detail derivable from them: AAPG Special Memoir 26, 477-502.

Sheriff, R. E., 1980, Nomograms for Fresnel-zone calculation: Geophysics, **45**, 968-972.

Spence, G. D., Clowes, R. M., and Ellis, R. M. 1985. Seismic structure across the active subduction zone of western canada. Journal of Geophysical Research, **90**, 6754-6772.

Stark, H., and Paul, I., 1981, An investigation of computerized tomography by direct fourier inversion and optimum interpolation, IEEE, Trans. Biomed. Eng., **BME-28**, 496-505.

Stolt, R. H., 1978, Migration by Fourier Transform, Geophysics, **43**, 23-48.

Stone, C.B., 1974, Geophysical hydrocarbon indicators: Paper presented at the 36th Annual International E.A.E.G. Meeting, Madrid, Spain.

Talwani, M., Worzel, J. L., and Landisman, M., 1959, Rapid gravity computatins for two-dimensional bodies with application to the Meandocino Submarine Fracture Zone, Journal of Geophysical Research, **64**, 49-59.

Telford, W. M., Geldart, L. P., Sheriff, R. E., and Keys, D. A. 1982. Applied Geophysics. Cambridge University Press.

Trorey, A.W., 1970, A simple theory for seismic diffractions, Geophysics, **35**, 762-784.

Trorey, A.W., 1977, Diffractions for arbitrary source-receiver locations: Geophysics, **42**, 1177-1182.

Waters, K.H., 1981, Reflection Seismology: A Tool For Energy Resource Exploration: John Wiley and Sons.

Widess, M. B., 1973, How thin is a thin bed?: Geophysics, **38**, 1176-1180.

Wiggins, R. A., 1972, The generalized linear inverse problem: Implication of surface waves and free oscillations for earth structure, Reviews of Geophysics and Space Physics, **10**, 251-285.

Wilson, J. T., 1965, A new class of faults and their bearing on continental drift: Nature, 207, 343-347.

Yorath, C. J., Clowes, R. M., Green, A. G., Sutherland Brown, A., Brandon, M. T., Massey, N. W. D., Spencer, C., Kanasewich, E. R., and Hyndman, R. D., 1985a, Lithoprobe, phase 1: Southern Vancouver Island: preliminary analyses of reflection seismic profiles and surface geological studies, *In* Current Research, part A, Geological Survey of Canada, Paper 85-1A, 543-554.

APPENDIX I

PARTIAL DERIVATIVES

The partial derivatives appearing in equations (2.9) to (2.16) are given in this appendix. The interfaces are represented by polynomials of the form

$$z_i = a_0 + f_i(x,y) \qquad i = 1, \ldots L \tag{I.1}$$

Therefore derivatives $(\partial z_i/\partial x_i)$ and $(\partial z_i/\partial y_i)$ can be very easily calculated by differentiating equation (I.1). Other partial derivatives are as follows

(1) For equations (2.13) and (2.14)

$$v_i' = v_i + k_i (z_i - z_{i-1}) \tag{I.2}$$

$$\frac{\partial v_i'}{\partial x_i} = k_i \frac{\partial z_i}{\partial x_i} \tag{I.3}$$

$$\sin \theta_i' = \frac{v_i'}{v_i} \sin \theta_i \tag{I.4}$$

$$\frac{\partial \theta_i'}{\partial x_i} = \frac{1}{v_i' \cos \theta_i'} \left\{ \sin \theta_i \frac{\partial v_i'}{\partial x_i} + v_i' \cos \theta_i \frac{\partial \theta_i}{\partial x_i} \right\} \tag{I.5}$$

$$\tan \theta_i = \frac{N_i}{D_i} \tag{I.6}$$

$$N_i = 2 v_i k_i \left[(x_i - x_{i-1})^2 + (y_i - y_{i-1})^2 \right]^{1/2} \tag{I.7}$$

$$D_i = k_i^2 \left[(x_i - x_{i-1})^2 + (y_i - y_{i-1})^2 \right] + (v_i')^2 - v_i^2 \tag{I.8}$$

$$\frac{\partial \theta_i}{\partial x_i} = \frac{D_i \frac{\partial N_i}{\partial x_i} - N_i \frac{\partial D_i}{\partial x_i}}{N_i^2 + D_i^2} \tag{I.9}$$

$$\frac{\partial N_i}{\partial x_i} = 2\, v_i\, k_i \left[(x_i - x_{i-1})^2 + (y_i - y_{i-1})^2 \right]^{-1/2} (x_i - x_{i-1}) \tag{I.10}$$

$$\frac{\partial D_i}{\partial x_i} = 2\, k_i^2 (x_i - x_{i-1}) + 2\, v_i \frac{\partial v_i}{\partial x_i} \tag{I.11}$$

$$\frac{\partial v_i}{\partial y_i} = k_i \frac{\partial z_i}{\partial y_i} \tag{I.12}$$

$$\frac{\partial \theta_i}{\partial y_i} = \frac{1}{v_i \cos \theta_i} \left\{ \sin \theta_i \frac{\partial v_i}{\partial y_i} + v_i \cos \theta_i \frac{\partial \theta_i}{\partial y_i} \right\} \tag{I.13}$$

$$\frac{\partial \theta_i}{\partial y_i} = \frac{D_i \frac{\partial N_i}{\partial y_i} - N_i \frac{\partial D_i}{\partial y_i}}{N_i^2 + D_i^2} \tag{I.14}$$

$$\frac{\partial N_i}{\partial y_i} = 2\, v_i\, k_i \left[(x_i - x_{i-1})^2 + (y_i - y_{i-1})^2 \right]^{-1/2} (y_i - y_{i-1}) \tag{I.15}$$

$$\frac{\partial D_i}{\partial y_i} = 2\, k_i^2 (y_i - y_{i-1}) + 2\, v_i \frac{\partial v_i}{\partial y_i} \tag{I.16}$$

(2) For equations (2.15) and (2.16)

$$v_{i+1} = v_{i+1} + k_{i+1} (z_{i+1} - z_i) \tag{I.17}$$

$$\frac{\partial v_{i+1}}{\partial x_i} = - k_{i+1} \frac{\partial z_i}{\partial x_i} \tag{I.18}$$

$$\sin \theta_{i+1} = \frac{v_{i+1}}{v_{i+1}} \sin \theta_{i+1} \tag{I.19}$$

$$\frac{\partial \theta_{i+1}}{\partial x_i} = \frac{1}{v_{i+1} \cos \theta_{i+1}} \left\{ \sin \theta_{i+1} \frac{\partial v_{i+1}}{\partial x_i} + v_{i+1} \cos \theta_{i+1} \frac{\partial \theta_{i+1}}{\partial x_i} \right\} \tag{I.20}$$

$$\tan \theta_{i+1} = \frac{N_{i+1}}{D_{i+1}} \tag{I.21}$$

$$N_{i+1} = 2 v_{i+1} k_{i+1} \left[(x_{i+1} - x_i)^2 + (y_{i+1} - y_i)^2 \right]^{1/2} \tag{I.22}$$

$$D_{i+1} = k_{i+1}^2 \left[(x_{i+1} - x_i)^2 + (y_{i+1} - y_i)^2 \right] + (v_{i+1})^2 - v_{i+1}^2 \tag{I.23}$$

$$\frac{\partial \theta_{i+1}}{\partial x_i} = \frac{D_{i+1} \frac{\partial N_{i+1}}{\partial x_i} - N_{i+1} \frac{\partial D_{i+1}}{\partial x_i}}{N_{i+1}^2 + D_{i+1}^2} \tag{I.24}$$

$$\frac{\partial N_{i+1}}{\partial x_i} = -2 v_{i+1} k_{i+1} \left[(x_{i+1} - x_i)^2 + (y_{i+1} - y_i)^2 \right]^{-1/2} (x_{i+1} - x_i) \tag{I.25}$$

$$\frac{\partial D_{i+1}}{\partial x_i} = 2 v_{i+1} \frac{\partial v_{i+1}}{\partial x_i} - 2 k_{i+1}^2 (x_{i+1} - x_i) \tag{I.26}$$

$$\frac{\partial v_{i+1}}{\partial y_i} = - k_{i+1} \frac{\partial z_i}{\partial y_i} \tag{I.27}$$

$$\frac{\partial \theta_{i+1}}{\partial y_i} = \frac{1}{v_{i+1} \cos \theta_{i+1}} \left\{ \sin \theta_{i+1} \frac{\partial v_{i+1}}{\partial y_i} + v_{i+1} \cos \theta_{i+1} \frac{\partial \theta_{i+1}}{\partial y_i} \right\} \tag{I.28}$$

$$\frac{\partial \theta_{i+1}}{\partial y_i} = \frac{D_{i+1} \frac{\partial N_{i+1}}{\partial y_i} - N_{i+1} \frac{\partial D_{i+1}}{\partial y_i}}{N_{i+1}^2 + D_{i+1}^2} \tag{I.29}$$

$$\frac{\partial N_{i+1}}{\partial y_i} = -2 v_{i+1} k_{i+1} \left[(x_{i+1} - x_i)^2 + (y_{i+1} - y_i)^2 \right]^{-1/2} (y_{i+1} - y_i) \tag{I.30}$$

$$\frac{\partial D_{i+1}}{\partial y_i} = 2 v_{i+1} \frac{\partial v_{i+1}}{\partial y_i} - 2 k_{i+1}^2 (y_{i+1} - y_i) \tag{I.31}$$

APPENDIX II

DIFFRACTION RESPONSE FOR NONZERO SOURCE-RECEIVER SEPARATION

The diffraction response for nonzero source-receiver separation is derived here, for the case when the shot-receiver axis is perpendicular to the edge of a truncated horizontal plane reflector. The derivation follows that of Berryhill (1977). The problem is solved by making use of Kirchhoff's retarded potential method. The field variation is expressed in terms of the velocity potential ϕ which is related to pressure by

$$p(x,y,z;t) = \rho \frac{\partial \phi(x,y,z;t)}{\partial t} \tag{II.1}$$

where ρ is the density. Both ϕ and p satisfy the acoustic wave equation. The potential at an external point 'ϕ_e' is expressed in terms of the incident potential 'ϕ_{inc}' and the retarded surface potential by (Bath 1968, Longhurst 1967)

$$\phi_e(t) = \phi_{inc}(t) + \frac{1}{4\pi} \iint_S \left\{ \frac{1}{r} \frac{\partial}{\partial n} \left[\phi_s(t-r/c) \right] - \frac{\partial}{\partial n} \left(\frac{1}{r} \right) \phi_s(t-r/c) + \frac{1}{cr} \frac{\partial r}{\partial n} \frac{\partial}{\partial t} \left[\phi_s(t-r/c) \right] \right\} dS \tag{II.2}$$

Imposing the rigid boundary condition of $(\partial\phi/\partial n)=0$ on surface S, we get

$$\phi_e(t) = \phi_{inc}(t) + \frac{1}{4\pi} \iint_S \left\{ \frac{1}{r^2} \frac{\partial r}{\partial n} \left[\phi_s(t-r/c) + \frac{r}{c} \frac{\partial}{\partial t} \phi_s(t-r/c) \right] \right\} dS \tag{II.3}$$

where c is the velocity, $\phi(t-r/c)$ is the retarded time potential and S is the boundary (interface). If the field point lies on the surface S then (Hilterman 1970)

$$\phi_s(t) = 2\,\phi_{inc}(t) + \frac{1}{2\pi}\iint_S \left\{ \frac{1}{r^2}\frac{\partial r}{\partial n}\left[\phi(t-r/c) + \frac{r}{c}\frac{\partial}{\partial t}\phi(t-r/c)\right]\right\} dS \tag{II.4}$$

using equation (II.1) in (II.3) we obtain the pressure field, i.e.

$$p_e(t) = p_{inc}(t) + \frac{1}{4\pi}\iint_S \left\{ \frac{1}{r^2}\frac{\partial r}{\partial n}\left[p_s(t-r/c) + \frac{r}{c}\frac{\partial}{\partial t}p_s(t-r/c)\right]\right\} dS \tag{II.5}$$

$$p_s(t) = 2\,p_{inc}(t) + \frac{1}{2\pi}\iint_S \left\{ \frac{1}{r^2}\frac{\partial r}{\partial n}\left[p(t-r/c) + \frac{r}{c}\frac{\partial}{\partial t}p(t-r/c)\right]\right\} dS \tag{II.6}$$

The pressure field at a distance D for a source function f(t) can be expressed by

$$p_D(t) = \frac{1}{D} f\left(t - \frac{D}{c}\right) \tag{II.7}$$

This represents a spherical wavefront having unit pressure at unit radius expanding from the source s.

Suppose r_s is the distance from a point on the surface to the source s and r_g is the distance from a point on the surface to the receiver g (Figure II.1). Approximating equation (II.7) by

$$p_s(t) \cong 2\frac{1}{r_s} f\left(t - \frac{r_s}{c}\right) \tag{II.8}$$

substituting (II.8) in (II.5) and dropping $p_{inc}(t)$, we obtain the diffraction response due to truncated reflector as

$$p_g(t) = \frac{1}{2\pi}\iint_S \left[\frac{1}{r_s} f\left(t - \frac{r_s}{c} - \frac{r_g}{c}\right) + \frac{r_g}{c}\frac{1}{r_s}\frac{\partial}{\partial t} f\left(t - \frac{r_s}{c} - \frac{r_g}{c}\right)\right]\frac{\cos\theta_g}{r_g^2} dS \tag{II.9}$$

where $\cos\theta_g = (\partial r_g/\partial n)$ (see Figure 1). The traveltime τ for the given source-receiver locations is given by

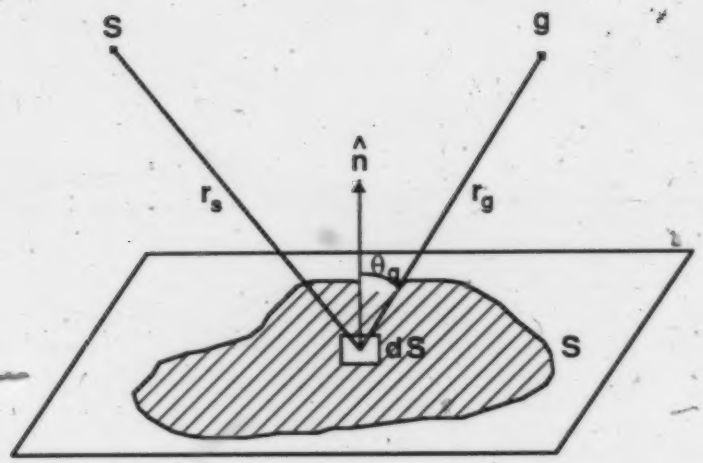

Figure II.1.Geometry for the Kirchhoff formulation of diffraction response.

$$\tau = \left(\frac{r_s + r_g}{c}\right) \tag{II.10}$$

To express dS in terms of dτ, prolate spheroidal coordinate system is used. The useful property of this system is the fact that each ellipsoid of revolution is the locus of points for which the sum of distances (r_s+r_g) is some constant. Thus each ellipsoid of revolution is a surface of constant traveltime τ. Prolate spheroidal coordinates are related to cartesian coordinates by (Margenau and Murphy 1956)

$$\begin{aligned} x &= a \cosh u \cos v \\ y &= a \sinh u \sin v \sin \phi \\ z &= a \sinh u \sin v \cos \phi \\ dx^2 + dy^2 + dz^2 &= a^2 (\sinh^2 u + \sin^2 v)(du^2 + dv^2) \\ &\quad + a^2 \sinh^2 u \sin^2 v \, d\phi^2 \end{aligned} \tag{II.11}$$

The origin is taken at the source-receiver midpoint and the source and receiver are located at -a and a respectively on the X-axis (Figure II.2). Constant u and v represent families of ellipses and hyperbolas orthogonal to one another. The ellipses and hyperbolas are rotated about the X-axis to form ellipsoids and hyperbolaids of revolution. The third coordinate is the angle of rotation φ. Moreover $u \geq 0$, $0 \leq v \leq \pi$, and $0 \leq \phi \leq 2\pi$. Now τ and σ are defined by

$$\begin{aligned} \tau &= \frac{r_s + r_g}{c} = 2a \cosh u / c \\ \sigma &= \frac{r_s - r_g}{c} = 2a \cos v / c \end{aligned} \tag{II.12}$$

Then

$$\begin{aligned} r_s &= a(\cosh u + \cos v) = c(\tau + \sigma)/2 \\ r_g &= a(\cosh u - \cos v) = c(\tau - \sigma)/2 \end{aligned} \tag{II.13}$$

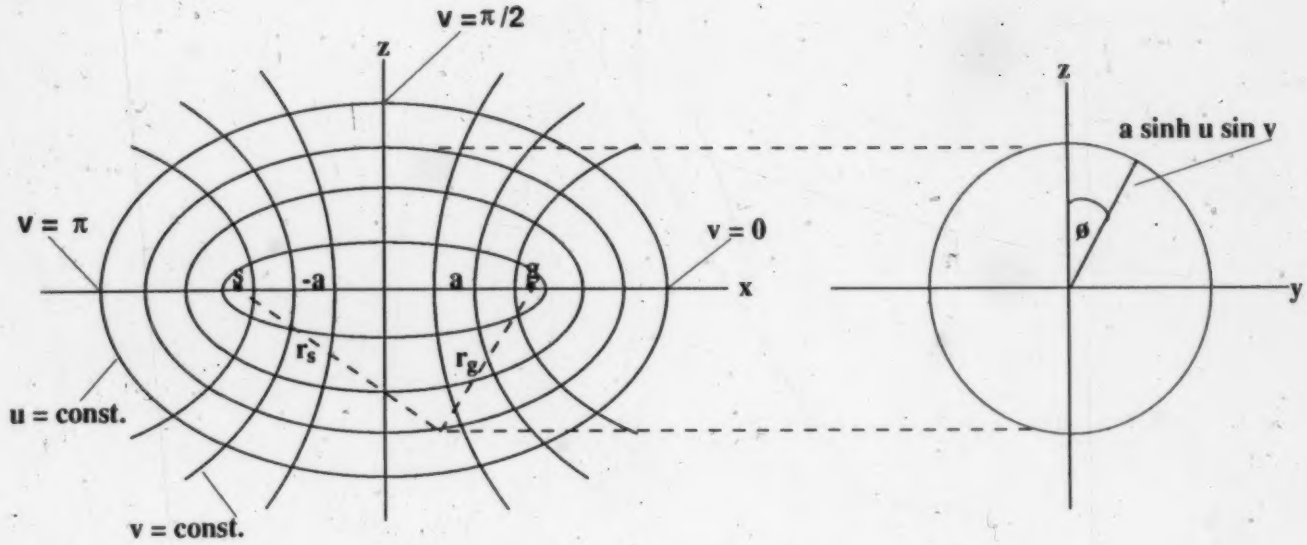

Figure II.2 The prolate spheroidal coordinate system. 's' and 'g' are the shot and receiver locations. 'r_s' and 'r_g' are the distances of the shot and receiver respectively from the subsurface point. 'r_s+r_g' is constant on the ellipsoid of revolution about the x-axis.

The truncated horizontal plane reflector is located at a depth of Z_0. Using (II.11), (II.12) and (II.13), we can express dS in terms of d(cosh u) and d(cos v) as (Berryhill 1977)

$$dS = a^2 G(\cosh u, \cos v)\, d(\cosh u)\, d(\cos v) \tag{II.14}$$

where

$$G(\cosh u, \cos v) = \frac{(\sinh^2 u + \sin^2 v)}{[\sinh^2 u \sin^2 v - z_0^2 / a^2]^{1/2}}$$

Now using (II.12), (II.13) and (II.14), we can write (II.9) in terms of $d\sigma$ and $d\tau$ as

$$p_g(t) = \frac{z_0}{2\pi} \iint_S f(t-\tau) \frac{2}{c(\tau+\sigma)} \frac{8}{c^3(\tau-\sigma)^3} a^2 G\left(\frac{c\tau}{2a}, \frac{c\sigma}{2a}\right) \frac{c^2}{4a^2} d\sigma\, d\tau$$

$$+ \frac{z_0}{2\pi} \iint_S \frac{1}{c} \frac{df(t-\tau)}{dt} \frac{2}{c(\tau+\sigma)} \frac{4}{c^2(\tau-\sigma)^2} a^2 G\left(\frac{c\tau}{2a}, \frac{c\sigma}{2a}\right) \frac{c^2}{4a^2} d\sigma\, d\tau \tag{II.15}$$

The integrations with respect to σ are carried out first and the results are written as

$$F_N(\tau) = \left(\frac{2}{c}\right)^N U(\tau - t_a) \int_{\sigma_{min}(\tau)}^{\sigma_{max}(\tau)} \frac{1}{(\tau-\sigma)^N} \frac{1}{(\tau^2-\sigma^2)} G\left(\frac{c\tau}{2a}, \frac{c\sigma}{2a}\right) d\sigma \qquad N = 1, 2 \tag{II.16}$$

where t_a is the first arrival time of the diffracted siignal. The limits of integration depend upon the geometry of the boundary surface. Substituting (II.16) into (II.15) yields

$$p_g(t) = \frac{z_0}{2\pi} \int_{-\infty}^{\infty} \left[f(t-\tau)\, F_2(\tau) + \frac{1}{c} \frac{df(t-\tau)}{dt} F_1(\tau) \right] d\tau \tag{II.17}$$

The lower integration limit for τ is extended to $-\infty$ by including a unit step function in the definition of $F_N(\tau)$. Then

$$p_g(t) = \frac{z_0}{2\pi} f(t) * \left[F_2(t) + \frac{1}{c} \frac{dF_1(t)}{dt} \right] \tag{II.18}$$

This expresses the response at the receiver as a convolution operation. Now the only problem is to evaluate the integrals in (II.16) by specifying the appropriate limits of integration for σ, and then substitute the results in (II.18). Rewriting (II.16) as

$$F_N(\tau) = \left(\frac{2}{c}\right)^N U(\tau - t_a) \left(\frac{c}{2a}\right)^{N+1} I_N(\tau)$$

$$= \frac{c}{2a\, a^N} U(\tau - t_a)\, I_N(\tau) \tag{II.19}$$

where

$$I_N(\tau) = \frac{1}{\sinh u} \int_{v_{max}(\tau)}^{v_{min}(\tau)} \frac{1}{(\cosh u - \cos v)^N} \frac{1}{\sqrt{K^2 - \cos^2 v}}\, d(\cos v)$$

$$N = 1, 2 \tag{II.20}$$

provided that

$$K^2 = 1 - \frac{z_0^2}{a^2 \sinh^2 u}$$

The integrals in (II.20) are given by (Gradshteyn and Ryzhik 1980)

$$\int \frac{1}{(\cosh u - \cos v)} \frac{1}{\sqrt{K^2 - \cos^2 v}}\, d(\cos v) =$$

$$- \frac{1}{\sqrt{\cosh^2 u - \cos^2 v}} \arcsin\left(\frac{K^2 - \cosh u \cos v}{K [\cosh u - \cos v]} \right) + \text{const} \tag{II.21}$$

$$\int \frac{1}{(\cosh u - \cos v)^2} \frac{1}{\sqrt{K^2 - \cos^2 v}} d(\cos v) =$$

$$\frac{\cosh u}{K^2 - \cosh^2 u} \frac{1}{\sqrt{\cosh^2 u - \cos^2 v}} \arcsin\left(\frac{K^2 - \cosh u \cos v}{K [\cosh u - \cos v]} \right)$$

$$- \frac{1}{(K^2 - \cosh^2 u)} \frac{\sqrt{K^2 - \cos^2 v}}{(\cos v - \cosh u)} + \text{const} \qquad \text{(II.22)}$$

The diffraction response, when the source receiver axis is perpendicular to the diffracting edge, is obtained now after finding out the limits of integration for v. Consider Figure II.3, the edge is located at $x=x_0$ and at a depth of $z=z_0$. At the first arrival time $\tau=t_a$, an ellipsoidal surface $u=u_{min}$ contacts the edge and is shown as a solid ellipse. The contact takes place in the x-z plane with y=0 and $\phi=\pi$. At later times, boundary surface S intersects the ellipsoid u=const along a curve which is a segment of an ellipse. Then from (II.11)

$$\cos v_{min} = \left[1 - \frac{z_0^2}{a^2 \sinh^2 u} \right]^{1/2} = K$$

v_{max} is obtained by substituting $x=x_0$ in (11), i.e.

$$\cos v_{max} = \frac{x_0}{a \cosh u}$$

Substituting these values of v_{min} and v_{max} in (II.15) and evaluating the integrals using (II.21) and (II.22), one obtains

$$I_1 = \frac{1}{\sinh u} \frac{1}{[\cosh^2 u - x_0^2 / (a^2 \cosh^2 u)]^{1/2}} \arcsin\left(\frac{\cosh u}{K} \frac{(a K^2 - x_0)}{(a \cosh^2 u - x_0)} \right)$$

$$+ \frac{1}{2} \frac{\pi}{\sinh u} \frac{1}{(\cosh^2 u - K^2)^{1/2}} \qquad \text{(II.23)}$$

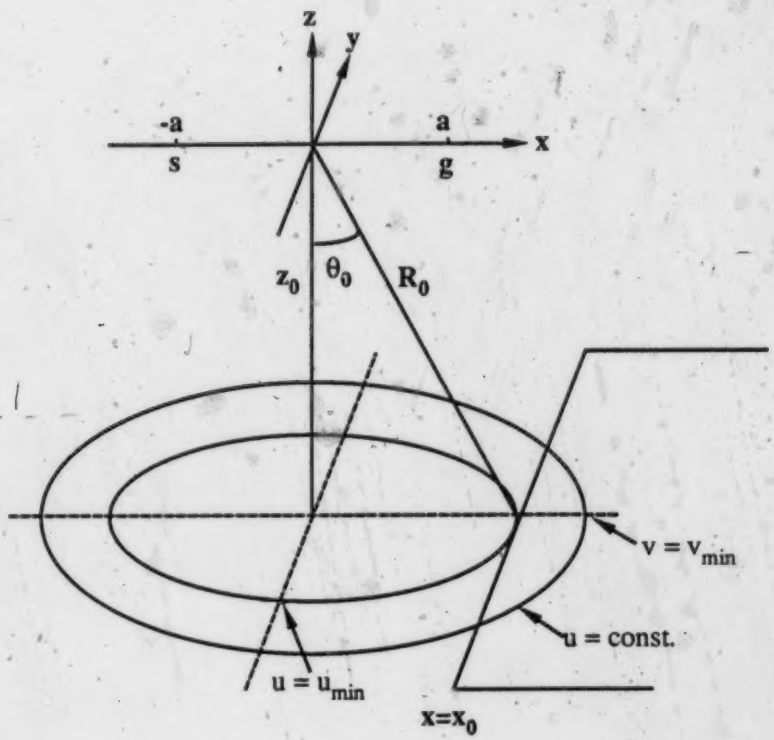

Figure II.3 Geometry for the calculation of the diffraction response due to a diffracting edge perpendicular to the shot-receiver axis.

$$I_2 = \frac{1}{\sinh u\,(\cosh^2 u - K^2)} \left\{ \frac{[K^2\cosh^2 u - x_0^2/a^2]^{1/2}}{\cosh^2 u - x_0/a} + \frac{\cosh u}{[\cosh^2 u - x_0^2/(a^2\cosh^2 u)]^{1/2}} \arcsin\left(\frac{\cosh u}{K} \frac{a K^2 - x_0}{(a\cosh^2 u - x_0)} \right) \right\} + \frac{\pi}{2} \frac{\cosh u}{\sinh u} \frac{1}{(\cosh^2 u - K^2)^{3/2}} \qquad \text{(II.24)}$$

Substituting (II.23) and (II.24) in (II.18) and making some algebraic simplifications, it becomes possible to write

$$F_2(t) + \frac{1}{c}\frac{dF_1(t)}{dt} = \frac{c}{2a^2} U(t-t_a) \left[C(t) + B(t)\,A(t)\,\Theta(t) + \frac{a}{c}\frac{d}{dt}(A(t)\,\Theta(t)) \right] \qquad \text{(II.25)}$$

where

$$A(t) = \frac{1}{\sinh u} \left[\cosh^2 u - \frac{x_0^2}{a^2\cosh^2 u} \right]^{-1/2}$$

$$B(t) = \frac{\cosh u}{\cosh^2 u - K^2}$$

$$C(t) = \frac{[K^2\cosh^2 u - x_0^2/a^2]^{1/2}}{\sinh u\,(\cosh^2 u - K^2)(\cosh^2 u - x_0/a)}$$

$$\Theta(t) = \arcsin\left[\frac{\cosh u}{K} \frac{(a K^2 - x_0)}{(a\cosh^2 u - x_0)} \right]$$

$$\cosh u = \frac{v\,t}{2\,a}$$

$$K = \left[1 - \frac{Z_0^2}{a^2 \sinh^2 u} \right]^{1/2}$$

and $\qquad \Theta(t_a) = -\pi/2$

Before writing the response at the receiver ($p_g(t)$) using (II.18), the above expression is appropriately normalized. This is done by using the expression for the zero source-receiver separation, since as 'a' approaches zero both expressions should produce same results. Therefore multiplying (II.25) by $2R_0$ and also introducing a factor of 2 to account for the fact that the derivation to this point has considered only the region $y > 0$, we obtain

$$p_g(t) = f(t) * D_a(t)\ U(t - t_a) \tag{II.26}$$

where

$$D_a(t) = \frac{1}{\pi} \cos\theta_0 \left[\frac{R_0^2 v}{a^3} [\, C(t) + B(t)\, A(t)\, \Theta(t) \,] + \frac{R_0^2}{a^2} \frac{d}{dt} [\, A(t)\, \Theta(t) \,] \right] \tag{II.27}$$

and

$$z_0 = R_0 \cos\theta_0$$